Field-Free Alignment and Strong Field Control of Molecular Rotors

by

Michael Spanner

A thesis
presented to the University of Waterloo
in fulfilment of the
thesis requirement for the degree of
Doctor of Philosophy
in
Physics

Waterloo, Ontario, Canada, 2004

Author's declaration for electronic submission of a thesis

I hereby declare that I am the sole author of this thesis. This is a true copy of the thesis, including any required final revisions, as accepted by my examiners.

I understand that my thesis may be made electronically available to the public.

Abstract

Methods of controlling molecular rotations using linearly polarized femtosecond and picosecond pulses are considered and analyzed theoretically. These laser pulses, typically in the infrared, are highly non-resonant with respect to the electronic degrees of freedom of the molecules and have intensities of $\sim 10^{13}$ to 10^{14} W/cm^2. It is shown how these laser pulses can force small linear molecules to align with the direction of the electric field vector of the laser both in the presence of the laser field as well as after the application of a short laser pulse. Recent experiments on laser-induced molecular alignment are modeled and excellent agreement between experiment and theory is found.

Additional methods of controlling molecular rotational dynamics are outlined. The first method considers the forced rotational acceleration of diatomic molecules, called the *optical centrifuge*. Here, the direction of polarization of a linearly polarized laser field is made to smoothly rotate faster and faster. The molecules, which tend to align with the polarization vector of the laser field, follow the rotation of the laser polarization and are accelerated to high angular momentum. The second method considers the control of field-free rotational dynamics by applying phase shifts to the molecular wave function at select times called *fractional revivals*. At these select moments, an initially localized wave function splits into several copies of the initial state. Adding phase shifts to the copies then induces interference effects which can be used to control the subsequent evolution of the rotational wave function. This same control scheme has a close link to quantum information and this connection is outlined. Finally, a recently proposed method of controlling the quantum dynamics of the classically chaotic kicked rotor system [J. Gong and P. Brumer, Phys. Rev. Lett. **86**, 1741 (2001)] is analyzed from a phase space perspective. It is shown that the proposed quantum control can be linked to small islands of stability in the classical phase space. An experimentally feasible variant of this control scenario using wave packets of molecular alignment is proposed.

Two applications of molecular alignment are discussed. The first application uses field-free aligned molecules as a non-linear medium for compression of a laser

pulse to the 1 fs regime at optical wavelengths. At such durations, these laser pulses contain nearly a single oscillation of the electric field and represent the shortest laser pulses physically achievable for such frequencies. The second application uses molecular alignment to create a sort of gas phase "molecular crystal" which forms a basis for laser-induced electron diffraction and imaging of the aligned molecules. Here, a first laser pulse aligns the molecules in space. A second laser pulse is then used to ionize outer-shell electrons, accelerate them in the laser field, and steer them back to collide with the parent ion creating a diffraction image with sub-femtosecond and sub-Angstrom resolution.

Acknowledgments

Firstly, I must thank my Mom for her brains and my Dad for his good looks (or was it the other way around...) Secondly, I must thank my sister, Irene-Ann, for teaching me how to be a student when we were kids.

At the beginning of my Ph.D. work, I saw my knowledge of computational and numerical methods as the dominant strength of my physics abilities. In this regard, I owe a huge dept of gratitude to the Commodore 64. It was on this ground breaking (and yet to truly be surpassed) machine that I first learned to love and respect the art of programming. Although I don't quite remember exactly my first program, I'm quite positive the following bit of code comes close and it will certainly serve as a proper tribute:

```
10 PRINT "MICHAEL IS THE BEST!"
20 GOTO 10
```

It was on the commodore 64 that I programmed my first graphics programs and computer games. The computational programs I now build in the name of physics are, to me, really little more than scientifically-biased computer games.

Second on the list of those whom deserve thanks for instilling in me the love of code is no doubt Adrian Secord. It was with him in 1^{st} and 2^{nd} year of university that my initial inclination to programming really took off. Together we tackled many recreational problems related to fractals, 3D rendering, and computer animation through which I learned how to be confident, comfortable, and patient with computers while getting at the desired results. He is also the reason I started using Linux, a development which truly reshaped how I thought about and interacted with computers.

Although my computer skills have certainly served me well, I now see them essentially as just another tool to study and learn about physics. As for my love of physics, the first person to blame for this passion is without a doubt Ben Sussman. Together with Ben, I managed to actually learn something from undergrad as opposed to simply "doing the work". We never once believed blindly things that our professors told us nor what was contained in most textbooks but rather remained continuously skeptical about pretty much every bit of physics that we could not prove for ourselves from first principles. Some of this skepticism is still with me today and has been a great help in digging my way to the bottom of many problems and being able to appreciate what is actually important in physical theories.

I am extremely indebted to my supervisor Misha Ivanov (see Figure 1). He has been my Delone, Krainov, Fedorov, Corkum, and Rzazewski all rolled into

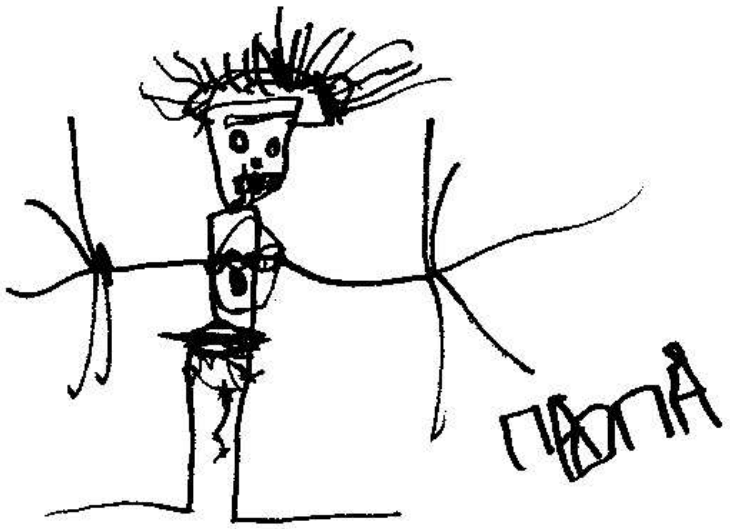

Figure 1: "Daddy" (© Mitia Ivanov, 2004)

one brilliant man. He taught me how to *think* about physics. Since day one, doing physics with Misha has been nothing but pure joy. He has given me endless encouragement and support always allowing me the freedom to explore whatever interested me.

Credit for my current perspective on physics must also go to Albert Stolow. Together, Albert and Misha taught me to be interested in ideas and to see the difference between physics and the tools we use to study physics. Another individual whom I consider as one my better teachers has been Paul Brumer. I find Paul's contribution to my style of physics a bit hard to describe. The best way to put it is that he has in some important way contributed to my idea of what proper scientist should be.

I also owe many thanks to all the great people I have work with from the Femtosecond group of the National Research Council of Canada over the past few years and in particular Zhenia Shapiro, Paul Corkum, David Villeneuve, François Légaré, Jérôme Levesque, Pat Dooley, Igor Litvinyuk, Kevin Lee, Jonathan Underwood, Anthony Lee, Ben Sussman, and Gennady Yudin. You have given me many good memories ranging from understanding the "experimental θ" to pondering how much friction one would need to climb a 90° corner. And a special thanks to Oliver Gessner for bringing better coffee to the coffee room!

As for the present thesis, I must acknowledge some direct contributions from my colleagues. Sections 2.3.2 and 2.4.2 present experimental results collected by

Pat Dooley, Igor Litvinyuk, and Kevin Lee. These experimental results have been previously published in [Phys. Rev. A **68**, 023406 (2003)] and [J. Phys. B: At. Mol. Opt. Phys. **37**, L43 (2004)]. Section 2.5.2 presents experimental results provided by Jonathan Underwood and Albert Stolow which have been previously published in [Phys. Rev. Lett. **90**, 223001 (2003)]. Section 3.2 was co-authored by Zhenia Shapiro, Misha Ivanov and myself and has been published in [Phys. Rev. Lett. **91**, 237901 (2003)] and [Phys. Rev. Lett. **92**, 093001 (2004)]. Section 4.2 was co-authored by Olga Smirnova, Misha Ivanov, and myself and has been published in [J. Phys. B: At. Mol. Opt. Phys. **37**, L243 (2004)].

Results of Section 3.1 have been published in [J. Chem. Phys. **114**, 3456 (2001)]. Section 4.1 has been published in [Opt. Lett. **28**, 576 (2003)].

This research was financially supported by the Natural Sciences and Engineering Research Council of Canada and the NRC Graduate Student Scholarship Supplement Program.

Publications

Much of the author's research related to this thesis has previously appeared in publications:

Strong Field Molecular Alignment

Section 2.3: Short-Pulse Alignment

P.W. Dooley, I.V. Litvinyuk, K.F. Lee, D.M. Rayner, M. Spanner, D.M. Villeneuve, and P.B. Corkum, *Direct imaging of rotational wave packet dynamics of diatomic molecules*, Phys. Rev. A **68**, 023406 (2003).

Section 2.4: Two-Pulse Alignment

K.F. Lee, I.V. Litvinyuk, P.W. Dooley, M. Spanner, D.M. Villeneuve, and P.B. Corkum, *Two-pulse alignment of molecules*, J. Phys. B: At. Mol. Opt. Phys. **37**, L43 (2004).

Section 2.5: Switched Wave Packets

J. Underwood, M. Spanner, M.Yu. Ivanov, J. Mottershead, B.J. Sussman, and A. Stolow, *Switched Wave Packets: A Route to Nonperturbative Quantum Control*, Phys. Rev. Lett. **90**, 223001 (2003).

Control of Rotational Wave-Packet Dynamics

Section 3.1: Optical Centrifuge

D.M. Villeneuve, S.A. Aseyev, P. Dietrich, M. Spanner, M.Yu. Ivanov, and P.B. Corkum, *Forced Molecular Rotation in an Optical Centrifuge*, Phys. Rev. Lett. **85**, 542-545 (2000).

M. Spanner and M.Yu. Ivanov, *Angular trapping and rotational dissociation of a diatomic molecule in an optical centrifuge*, J. Chem. Phys. **114**, 3456-3464 (2001).

M. Spanner, K.M. Davitt and M.Yu. Ivanov, *Stability of angular confinement and rotational acceleration of a diatomic molecule in an optical centrifuge*, J. Chem. Phys. **115**, 8403-8410 (2001).

Section 3.2: Control of Revival Dynamics

E.A. Shapiro, M. Spanner, and M.Yu. Ivanov, *Quantum Logic Approach to Wave Packet Control*, Phys. Rev. Lett. **91**, 237901 (2003).

M. Spanner, E.A. Shapiro, and M.Yu. Ivanov, *Coherent Control of Rotational Wave Packet Dynamics via Fractional Revivals*, Phys. Rev. Lett. **92**, 093001 (2004).

Applications of Molecular Alignment

Section 4.1: Pulse Compression

V. Kalosha, M. Spanner, J. Herrmann, and M. Ivanov, *Generation of Single Dispersion Precompensated 1 fs Pulses by Shaped-Pulse Optimized High-Order Stimulated Raman Scattering*, Phys. Rev. Lett. **88**, 103901 (2002).

M. Spanner and M.Yu. Ivanov, *Optimal Generation of Single Dispersion Precompensated 1 fs Pulses by Molecular Phase Modulation*, Opt. Lett. **28**, 576 (2003).

Section 4.2: Laser-Induced Electron Diffraction

M. Spanner, O. Smirnova, P.B. Corkum, and M.Yu. Ivanov, *Reading diffraction images in strong field ionization of diatomic molecules*, J. Phys. B: At. Mol. Opt. Phys. **37**, L243 (2004).

Additional Works

Works published during the author's Ph.D. not directly related to the topic of the present thesis:

E.A. Shapiro, I. Khavkine, M. Spanner, and M.Yu. Ivanov, *Strong-field molecular alignment for quantum logic and quantum control*, Phys. Rev. A **67**, 013406 (2003).

M. Spanner, M.Yu. Ivanov, V. Kalosha, J. Herrmann, D.A. Wiersma, and M. Pshenichnikov, *Tunable Optimal Compression of Ultrabroadband Pulses by Cross-Phase Modulation*, Opt. Lett. **28**, 749 (2003).

M. Spanner, M. Pshenichnikov, V. Olvo, and M.Yu. Ivanov, *Controlled Supercontinuum Generation for Optimal Pulse Compression: A Time-Warp Analysis of Nonlinear Propagation of Ultrabroadband Pulses*, App. Phys. B **77**, 329-336 (2003).

M. Spanner, *Strong Field Tunnel Ionization by Real-Valued Classical Trajectories*, Phys. Rev. Lett. **90**, 233005 (2003).

O. Smirnova, M. Spanner, and M. Ivanov, *A molecule without electrons – binding bare nuclei with strong laser fields*, Phys. Rev. Lett. **90**, 243001 (2003).

Contents

List of Tables

List of Figures

Chapter 1

Introduction

The idea that light can exert forces on matter dates back to the time of Kepler. In his 1619 treatise *De Cometis*, the hypothesis was put forth that solar ray pressure acting on the tails of comets is responsible for the observation that these tails point away from the sun. However, a quantitative understanding of the forces that light could exert on matter came only in the 1870s with Maxwell's theory of electromagnetism and the calculation of the momentum flux density of light. Shortly after came experimental demonstrations by Lebedev in 1901 [1] and Nichols and Hull in 1901 and 1903 [2,3]. Using torsion balances in vacua, these experiments demonstrated that light can exert a minute pressure on small reflective surfaces. The quantum nature of the light pressure was found by Einstein in 1917 when he postulated that quanta of light carry momentum $p = h/\lambda$ where λ is the wavelength of the light and h is Planck's constant [4]. Any emission or absorption of light quanta by matter must then be accompanied by a corresponding transfer of momentum.

The observation of the forces exerted by light on individual atoms came in 1933 when Frisch measured the deflection of an atomic beam of sodium with radiation from a sodium resonance lamp [5]. This experiment demonstrates the manipulation of the external degrees of freedom of atoms, namely their linear momentum. The effects of light on the internal degrees of freedom of atoms, namely their angular momentum, were seen in the early 1950s in the work of Kastler [6, 7] on optical

pumping techniques. With the invention of the laser, these methods of controlling atoms with light were much studied and greatly refined. Eventually these studies lead to the successes of laser cooling and trapping of atoms [8–11] and the realization of Bose-Einstein condensates [12, 13].

The methods of controlling atomic motion with lasers take advantage of isolated transitions present in the atomic level structure and the large dynamic polarizabilities associated with near-resonant excitation. Such methods, however, can not be readily carried over to the control of molecules. A much more complex and dense level structure exists in molecules due to the many nuclear and electronic degrees of freedom making isolated transitions the exception rather than the rule. One possible alternative is to use highly non-resonant low frequency fields when trying to control molecules with lasers. Unfortunately, the molecular polarizabilities in the regime of highly non-resonant (with respect to electronic degrees of freedom) excitation are essentially static polarizabilities that are much smaller than the dynamic polarizabilities arising from near-resonant excitation. For many years laser technology was not capable of providing enough intensity to make use of these non-resonant interactions. For example, using near-resonant interactions with large dynamic polarizabilities, researchers were able to focus an atomic beam using a focused laser beam as early as 1978 [14]. The intensity needed to accomplish a similar feat with molecular beams in the regime of non-resonant excitation, however, is much larger than that needed in the atomic case due to the low polarizabilities in the non-resonant regime. The focusing of a molecular beam using lasers was not realized until 1998 [15, 16], a full two decades after the focusing of atomic beams. The development in laser technology largely responsible for achieving the necessary intensities for non-resonant control of molecules was the chirped-pulse amplification (CPA) of ultrashort pulses in 1985 [17]. In the years following the invention of CPA, modern laser systems have evolved to the point where interaction energies of $\sim$50 meV lasting hundreds of picoseconds are now routinely available for molecules in strong non-resonant laser fields [16]. These energies surpass the thermal energy at room temperature of 25 meV showing that the control of even room temperature molecules is possible.

The present thesis considers the control of rotations of small linear molecules using strong non-resonant ultrashort laser pulses in the range of $\sim 10^{13}$ to 10^{14} W/cm^2 and ~ 50 fs to 100 ps. Due to very low laser frequency compared to the ionization potential, even these relatively high intensities lie just below the threshold of molecular ionization for these time scales. Ionization in this regime occurs in a manner similar to tunnel ionization in static electric fields and is termed "optical tunneling" [18]. These laser pulses are essentially the largest fields one can apply to molecules for tens to hundreds of picoseconds without destroying the molecules. The first control scenario considered is that of molecular alignment. In this process, all the molecules in the focus of the laser are forced by the laser field to align with the direction of the electric field vector.

Molecular alignment induced by a strong non-resonant laser field was first studied theoretically by Zon and Katsnelson [19] in 1975. However, the current burst of activity in this field was initiated by the work of Friedrich and Herschbach [20] and Seideman [21] the mid-90s. To date there have been both theoretical proposals and experimental realizations of (i) in-field alignment of small molecules [20–24], (ii) field-free alignment of small molecules wherein alignment occurs *after* the interaction with the laser pulse [25–35], (iii) multi-pulse enhancement of field-free molecular alignment [36–40], (iv) 3-dimensional alignment (that is, the confinement of all three Euler angles) of polyatomic molecules using elliptically polarized laser fields [41].

Chapter 2 begins with a description of the computational tools required to model strong field molecular alignment. The discussion then moves on to illustrate the methods of adiabatic alignment, short-pulse alignment, two-pulse alignment, and alignment by switched wave packets. This choice of topics reflects recent experiments on strong field alignment of N_2, O_2, and CO_2 undertaken by the groups of Paul Corkum [31, 38] and Albert Stolow [34] of the National Research Council of Canada in Ottawa. The experimental results are compared against the theoretical predictions and excellent agreement is found.

Chapter 3 considers other methods of controlling rotational dynamics of small linear molecules, again based on the non-resonant interactions. The first section

outlines a method of forced rotational acceleration of molecules called the optical centrifuge [42–45]. In this scenario, the molecules are trapped in the angular potential well created by a linearly polarized laser field. The polarization vector of the electric field is then made to rotate, forcing the molecules follow. Using such a method, the molecules can be accelerated to such a high angular momentum that rotational dissociation occurs due to centrifugal forces.

The second section outlines the idea of controlling field-free dynamics of rotational wave packets (i.e., superpositions of field-free eigenstates) by applying angular-dependent phase shifts to the rotational wave function [46]. These phase shifts are induced by short laser pulses and are applied at moments of *fractional revivals*, moments where the wave packet has split into multiple copies of the initial wave packet by field-free time evolution. The multiple copies effectively act as multiple slits in an interference experiment. Just as changing the relative phase of the wave function at the various slits in a multi-slit experiment would change the observed interference in the evolution beyond the slits, changing the relative phase of the wave packet copies at the fractional revivals changes the interferences, and hence the dynamics, in the subsequent evolution of the rotational wave function.

This same control scenario can also be viewed from a quantum logic perspective [47]. The wave-packet shape and symmetry at the moments of fractional revivals can be used to encode qubits. Field-free evolution together with phase shifts at the moments of fractional revivals can be used to construct a logarithmically small number of gates to exert complete control over the encoded qubits. Using this formalism, one could construct complex wave-packet control scenarios from a small set of basic operations in the same way that a quantum computer executes large algorithms using a small set of fundamental gates. The formalism is general and can be applied to any type of wave packets. Although this perspective could be illustrated using molecular rotations, the discussion deviates a bit from this theme and wave packets of molecular vibrations are used as an example.

The third section examines a recently proposed scenario for the quantum control of a classically chaotic system, namely the kicked rotor model [48, 49]. The quantum mechanics of classically chaotic systems is qualitative different than the

quantum mechanics of classically regular systems. The level spacings of a chaotic system exhibits Wigner statistic while the spacings of regular systems exhibit Poissonian statistics [50]. The wave functions can not be approximated by standard semiclassical methods (such as WKB or EBK quantization [51]) but are instead well described by random matrix theory and exhibit occasional 'scars' of unstable periodic orbits [52]. Little at present is known about the control of quantum motion in classically chaotic systems, or even if there is a difference between control in this regime and control in the classically regular regime. In this section, a strong connection between quantum control of the kicked rotor system in the mildly chaotic regime and small regular structures in the classical phase space is found. These regular structures in the classical phase space are too small to effect the classical dynamics but are seen to strongly influence the quantum system. Furthermore, it is shown that the kicked rotor system can be implemented in small linear molecules using strong non-resonant laser interactions and that a variant of the Gong-Brumer control scenario [48, 49] can be implemented using wave packets of molecular alignment.

In Chapter 4, the discussion shifts to consider applications of molecular alignment. The first application presented uses molecular alignment for compression of laser pulses.

To create a short laser pulse one must first create a large coherent bandwidth of frequencies. After the creation of a large bandwidth, the phases across the spectrum must be adjusted to compress this bandwidth into a short pulse. Ideally, all the frequencies in the pulse should be in phase. This leads to a *transform limited* pulse and is the shortest pulse that can be obtained for a given bandwidth. Currently, the most advanced techniques of pulse compression create a large bandwidth in a short pulse using self-phase modulation in a gas-filled hollow-core fiber. The phases of the resulting broad spectrum are then adjusted after the fiber using gratings, chirped mirror, and/or pulse-shaping devices [53, 54]. Using such compression methods, pulses of $\sim$5 fs in the optical regime can be obtained [55–58].

The method of pulse compression by self-phase modulation, however, has limitations. The phase-adjusting optical components after the fiber can not easily

accommodate the particular phase profiles that result from self-phase modulation for an arbitrarily large spectrum. This limits the size of the controllable spectrum and hence the limits the smallest pulse durations attainable. One might then consider using some form of pre-shaping of the pulse before spectral broadening in the fiber to help control the phases of the generated spectrum at the output of the fiber. In the case of self-phase modulation, however, this leads to a non-linear optimization problem since the pulse itself creates the non-linear interaction used to broaden the spectrum. Such non-linear optimization problems often lead to complex and unstable optimal solutions.

An alternate route of pulse compression is proposed to circumvent these problems [32, 33]. Instead of generating a broad spectrum by self-phase modulation, a strong 'pump' pulse is used to first create field-free rotational wave packets in a molecular gas contained in a hollow-core fiber. A second 'probe' pulse (the pulse one is interested in compressing) is then sent through the fiber timed to propagated on one of the rotational revivals. The time-dependent alignment of the molecules during the revival creates a time-dependent refractive index which broadens the spectrum of the probe pulse. Since the creation of the non-linear response of the medium (i.e. the creation of the rotational wave packets) is now decoupled from the pulse one is interested in compressing, pre-shaping of the probe pulse at the input of the fiber to optimize the particular phase profile of the probe spectrum at the output of the fiber no longer leads to a non-linear optimization problem. Using this method, it should be possible to compress optical pulses to $\sim$1 fs. At these durations, optical pulses contain essentially one oscillation of the electric field and are the shortest pulses physically obtainable for such wavelengths.

The second application of molecular alignment presented is time-resolved laser-induced electron diffraction and imaging of molecules [59]. By controlling the alignment of molecules in a gas, a sort of 'gas phase crystal' structure can be made in which all the molecules of the gas are aligned to the same direction in space. Diffraction images of such optically-induced 'molecular crystals' can taken using the molecules' own electrons. A low frequency non-resonant near-single-cycle laser pulse is used to liberate outer-shell electrons by tunnel ionization. These elec-

trons are then accelerated to ∼100 eV energies in the laser field and sent back to collide with the parent molecules once the oscillating electric field vector of the near-single-cycle pulse has changed direction. The collision of the electrons with the parent molecule lasts only a few hundred attoseconds. Diffraction images of small molecules with sub-Angstrom and sub-femtosecond accuracy is then possible, improving existing electron diffraction imaging resolution of gas phase molecular dynamics [60] by several orders of magnitude.

Chapter 2

Strong Field Molecular Alignment

2.1 Calculation of Rotational Wave-Packet Dynamics

2.1.1 Angle-dependent AC Stark Shift

Any non-spherical polarizable particle placed in an electric field will experience a torque due to the angular-dependent interaction (potential) energy U between the induced dipole moment $\vec{p} = \vec{\alpha} \cdot \vec{\mathcal{E}}$ and the field $\vec{\mathcal{E}}$. This potential energy term arises as follows [61]. Consider, for simplicity, a linear particle having one dominant axis of polarizability $\alpha_{\parallel} > \alpha_{\perp}$ as shown in Figure 2.1. When placed in the field $\vec{\mathcal{E}}$ the potential energy is given by $U = -\vec{p} \cdot \vec{\mathcal{E}}$. The change in the potential energy for a small change of the field strength $d\vec{\mathcal{E}}$ would be

$$dU = -\vec{p} \cdot d\vec{\mathcal{E}} = -p_{\parallel} d\mathcal{E}_{\parallel} - p_{\perp} d\mathcal{E}_{\perp}, \tag{2.1}$$

where the directions $\parallel$ and $\perp$ are parallel and perpendicular to the dominant axis of the particle. After substitution of the components of the induced dipole moment $p_i = \alpha_i \mathcal{E}_i$, d$U$ becomes

$$dU = -\alpha_{\parallel} \mathcal{E}_{\parallel} d\mathcal{E}_{\parallel} - \alpha_{\perp} \mathcal{E}_{\perp} d\mathcal{E}_{\perp} \tag{2.2}$$

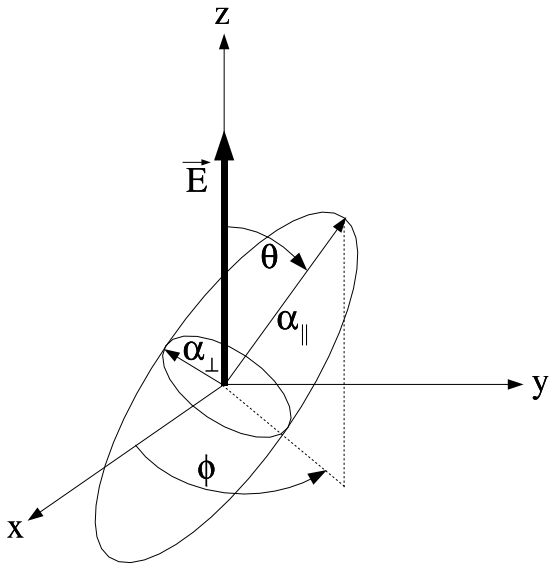

Figure 2.1: Geometry of an anisotropic particle in an electric field $\vec{\mathcal{E}}$.

which can be integrated to give

$$U = -\frac{1}{2}\left[\alpha_{\parallel}\mathcal{E}_{\parallel}^2 + \alpha_{\perp}\mathcal{E}_{\perp}^2\right]. \tag{2.3}$$

By using the angle θ between the dominant axis of the particle and the electric field $\vec{\mathcal{E}}$ this can be written as

$$\begin{aligned} U(\theta) &= -\frac{1}{2}\left[\alpha_{\parallel}\mathcal{E}^2\cos^2\theta + \alpha_{\perp}\mathcal{E}^2\sin^2\theta\right] \\ &= -\frac{1}{2}\alpha_{\perp}\mathcal{E}^2 - \frac{1}{2}\Delta\alpha\mathcal{E}^2\cos^2\theta. \end{aligned} \tag{2.4}$$

with $\Delta\alpha = (\alpha_{\parallel} - \alpha_{\perp})$.

This potential contains a constant term and an angular-dependent term. The constant term, however, is just a coordinate-independent shift which does not introduce any torques and can hence be dropped for convenience. Furthermore, when dealing with the particular case of diatomic molecules placed in infrared or near-infrared laser fields $\mathcal{E}(t) \sim \mathcal{E}_0 \sin\omega t$ which are far off-resonant with rotational frequencies, as is typical in experiments of strong field control of molecular rota-

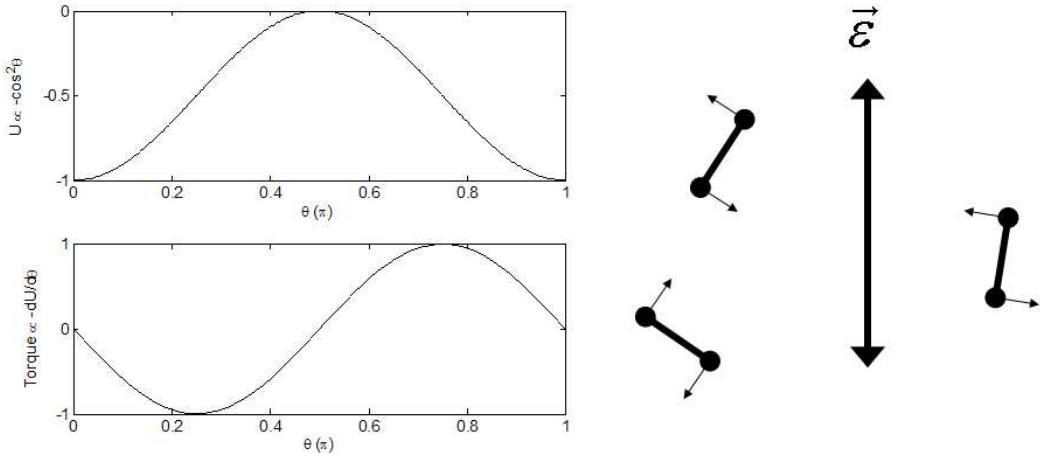

Figure 2.2: Schematic plot of the angular-dependence of potential energy U and the torque $\sim dU/d\theta$ felt by the molecules in a strong non-resonant laser field (right). The molecules will tend to rotate toward the electric field of the laser (left).

tions, the oscillating electric field switches direction too fast for the nuclei to follow directly. These oscillations can be removed from the potential energy by considering instead the time-average of the energy $U(\theta)$ over one cycle

$$\begin{aligned} U(\theta,t) &= \int_0^{2\pi} \frac{1}{2}\Delta\alpha\mathcal{E}_0^2 f^2(t)\sin^2(t')\cos^2\theta dt' \\ &= -\frac{1}{4}\Delta\alpha\mathcal{E}_0^2 f^2(t)\cos^2\theta \end{aligned} \tag{2.5}$$

where $\mathcal{E}_0$ is the maximum field strength of the laser and $f(t)$ represents the envelope of the laser pulse which varies much slower than the field oscillations. This laser-induced potential energy is known as the angular AC Stark shift [20]. Note that any permanent dipole of the molecule would give a zero contribution to the potential energy upon time-averaging over one cycle of the laser field.

The potential energy $U(\theta)$ as well as the corresponding torque $\propto -dU/d\theta$ is plotted schematically in Figure 2.2. The interaction with the laser field creates two potential wells located at $\theta = 0$ and $\theta = \pi$. The molecules feel a torque which pushes them toward the direction of the laser polarization. Molecules with angles

$0 < \theta < \pi/2$ feel a negative torque and are pushed toward $\theta = 0$ while molecules with angles $\pi/2 < \theta < \pi$ feel a positive torque and are pushed toward $\theta = \pi$.

The maximum Stark shift U that can be achieved in a molecule is limited by ionization: if the field strength is increased too much, the outer most electrons of the molecule will be removed by tunnel ionization. Judging by the structure of the Stark shift 2.5, one might immediately assume that larger Stark shifts can be achieved in molecules with larger polarizabilities before ionization becomes important. However, this is not the case. As the molecular polarizability decreases, the ionization potential typically increases. Molecules with lower polarizabilities can then withstand larger intensities which compensates for their low polarizabilities [16]. Stark shifts of 50 meV can be obtained on hundred picosecond time scales for most diatomics. The angular well created by the stark shift is then deep enough to trap most small molecules even at room temperature where $kT = 25$ meV.

2.1.2 Initial Ensemble

The specific systems being considered are molecular gases interacting with linearly polarized infrared laser pulses. Before the laser pulse interacts with the molecular gas, the system is assumed to be in a thermal ensemble characterized by a temperature T. In the quantum picture, this system is described by a statistical mixture of angular momentum states. Each molecule finds itself in a definite state of angular momentum $|J, M\rangle$ where J is the orbital momentum $J = 0, 1, 2,...$ The M is the projection of the angular momentum onto the z-axis of the coordinate system and can take on the values $M = -J, -(J-1), ..., J-1, J$. The coordinate wave functions of this basis are the spherical harmonics $Y_M^J(\theta, \phi)$. The distribution of angular momentum amongst the various molecules in the gas is given by the Boltzmann distribution

$$P_J \sim (2J + 1) \exp(-E_J/kT) \tag{2.6}$$

where E_J is the rotational energy of the state $|J, M\rangle$. The $(2J + 1)$ term accounts for the degeneracies within a given J level because of the different M sub-levels.

In the case of homonuclear diatomics, there is an additional factor g_J in the

Boltzmann distribution arising from the nuclear spin statistics [62]

$$P_J \sim g_J(2J+1)\exp(-E_J/kT). \tag{2.7}$$

This factor controls the relative weight between even and odd J states. The nuclear spin statistics are best understood using a short example. Consider the case of N_2. Each N atom has spin 1 and is therefore a boson. When the two N atoms are brought together to form an N_2 molecule, their spins can add in different ways to give one of the following possible spin states $|S, M_s\rangle$

$$\begin{array}{lcccl} S=0 & : & |0,0\rangle & : & 1\,\text{state} \\ S=1 & : & |1,-1\rangle, |1,0\rangle, |1,1\rangle & : & 3\,\text{states} \\ S=2 & : & |2,-2\rangle, |2,-1\rangle, |2,0\rangle, |2,1\rangle, |2,2\rangle & : & 5\,\text{states.} \end{array} \tag{2.8}$$

For N_2, these spin states are equally populated in a thermal ensemble. Since the two N atoms are bosons, the total nuclear wave function $\Psi_{spin} \times \Psi(\theta, \phi)$ must be symmetric under the exchange of these two particles. There are in total 6 possibilities of symmetric spin wave functions, which must be accompanied by symmetric coordinate wave functions, and 3 antisymmetric spin wave functions, which must be accompanied by antisymmetric coordinate wave functions. Therefore, due to the spin statistics, the relative weights of the even and odd J in the case of N_2 will be

$$g_J = \begin{cases} 2, & \text{for even } J \\ 1, & \text{for odd } J. \end{cases} \tag{2.9}$$

In some species of diatomics, only one of the possible spin states will be present in the thermal distribution. This is the case for O_2. In such a situation, only one of the two symmetries of J states (even or odd) will be present. The g_J weights for the molecules considered in this work as well as relevant rotational constants and polarizabilities are tabulated in Table 2.1.2. Note that although CO_2 is not actually a homonuclear diatomic, the two O atoms are indistinguishable and hence symmetrization of the wave function with respect to these two particles must still be enforced which leads to the presence of a g_J for CO_2.

Molecule	B_0 (cm^{-1})	D_0 (cm^{-1})	$\Delta\alpha$ ($\mathring{A}^3$)	g_{even}	g_{odd}
N_2	1.989581	5.76×10^{-6}	1.0	2	1
O_2	1.4297	4.839×10^{-6}	1.15	0	1
CO_2	0.3902	0.135×10^{-6}	2.0	1	0

Table 2.1: Molecular properties for the different species considered in this work [62–65].

2.1.3 Quantum Evolution

When the laser pulse interacts with the molecular gas, rotational wave packets (i.e. superpositions of the field-free eigenstates $|J, M\rangle$) are created in each molecule. The particular wave packet created in a given molecule will depend on its initial angular momentum state. Hence, to calculate the response of the molecular medium, the induced wave packet starting from each initial state in the thermal distribution must be calculated.

Consider a laser pulse with the electric field linearly polarized along the z-axis as in Figure 2.1. The interaction of laser pulse with the molecule is described by the Schrödinger equation [20]

$$i\dot{\Psi}(\theta, \phi, t) = \left[B\mathbf{J}^2 - U_0(t)\cos^2\theta\right]\Psi(\theta, \phi, t) \tag{2.10}$$

where θ is the angle between the laser polarization and the molecular axis, $\mathrm{B}\mathbf{J}^2$ is the rotational energy operator, and $U_0(t) = \frac{1}{4}\Delta\alpha\mathcal{E}_0^2 f^2(t)$. Here, and throughout this work, equations are written in atomic units ($e = m_{electron} = \hbar = 1$). The pulse shapes considered typically have the form

$$f^2(t) = \begin{cases} \sin^2\left(\frac{\pi t}{2\tau_{on}}\right) & , \ 0 \leq t < 2\tau_{on} \\ 0 & , \text{ for all other } t \end{cases} \tag{2.11}$$

where τ_{on} gives the time for the pulse to rise from zero to peak amplitude and is also the full width at half maximum (FWHM) of the $\sin^2$ pulse.

Rovibrational coupling is included by writing the $B\mathbf{J}^2$ operator as $B_0 J(J+1) - D_0[J(J+1)]^2$ in the angular momentum basis [62]. The D_0 term accounts

for bond stretching at high angular momentum. Further corrections to the kinetic energy arising from vibrational excitation can be neglected since (i) essentially no thermal vibrational excitation exists for the molecular species considered herein (for example, less than 10^{-5} N_2 molecules are vibrationally excited for temperatures smaller than 300 K [62]), (ii) homonuclears are IR inactive, and hence no Raman resonances with vibrations will occur during the interaction with the pulse.

The evolution of the wave function for the duration of the aligning pulse was calculated numerically in the angular momentum basis $|J, M\rangle$. The time-dependent wave function is first expanded in the $|J, M\rangle$ basis

$$|\Psi(t)\rangle = \sum_{J,M} A_{J,M}(t)|J, M\rangle. \tag{2.12}$$

In this basis, the Hamiltonian $\mathbf{H}(t) = [B\mathbf{J}^2 - U_0(t)\cos^2\theta]$ becomes

$$\begin{aligned}\langle J, M|\mathbf{H}(t)|\Psi(t)\rangle &= \left\{B_0 J(J+1) - D_0[J(J+1)]^2\right\} A_{J,M} - \\ &\quad U_0(t)C_{J,J+2,M}A_{J+2,M} - U_0(t)C_{J,J,M}A_{J,M} - \\ &\quad U_0(t)C_{J,J-2,M}A_{J-2,M}\end{aligned} \tag{2.13}$$

where

$$\begin{aligned}C_{J,J,M} &= \langle J, M|\cos^2\theta|J, M\rangle \\ C_{J,J+2,M} &= \langle J, M|\cos^2\theta|J+2, M\rangle \\ C_{J,J-2,M} &= \langle J, M|\cos^2\theta|J-2, M\rangle.\end{aligned} \tag{2.14}$$

The Hamiltonian (2.13) does not couple even and odd J. All transitions occur between $J \leftrightarrow J+2$ and $J \leftrightarrow J-2$. This is a consequence of the symmetry of the angular potential $\cos^2\theta$ with respect to the point $\theta = \pi/2$. Furthermore, different M states do not couple. This is a consequence of the cylindrical symmetry of the angular potential (i.e. no ϕ dependence).

Due to the lack of M coupling, the original Schrödinger equation (2.10) for θ and ϕ reduces to a single 1-dimensional equation when the initial state is assumed

to be a single eigenstate of angular momentum. The solution of this equation is calculated numerically using the following method. The formal solution to the time-dependent Schrödinger equation

$$i\frac{\partial}{\partial t}\Psi(t) = \mathbf{H}\Psi \tag{2.15}$$

for an infinitesimal time step dt is

$$\Psi(t+dt) = e^{-i\mathbf{H}dt}\Psi(t). \tag{2.16}$$

The exponential operator is now split into two parts

$$e^{-i\mathbf{H}dt} = \frac{e^{-i\mathbf{H}dt/2}}{e^{+i\mathbf{H}dt/2}} \tag{2.17}$$

and the formal solution is re-written as

$$e^{+i\mathbf{H}dt/2}\Psi(t+dt) = e^{-i\mathbf{H}dt/2}\Psi(t). \tag{2.18}$$

Expanding the exponentials in a Taylor series and writing the infinitesimal dt as a small but finite time step Δt then gives

$$\left[1 + i\frac{\Delta t}{2}\mathbf{H}(t+\Delta t)\right]\Psi(t+\Delta t) = \left[1 - i\frac{\Delta t}{2}\mathbf{H}(t)\right]\Psi(t). \tag{2.19}$$

This is the Cranck-Nicholson method [66]. In the angular momentum representation this Cranck-Nicholson equation becomes a tridiagonal set of linear equations for the amplitudes $A_{J,M}(t) \equiv A^t_{J,M}$

$$\begin{aligned} F_1^{t+\Delta t}A^{t+\Delta t}_{J+2,M} + (1+F_2^{t+\Delta t})A^{t+\Delta t}_{J,M} + F_3^{t+\Delta t}A^{t+\Delta t}_{J-2,M} = \\ -F_1^t A^t_{J+2,M} + (1-F_2^t)A^t_{J,M} - F_3^t A^t_{J-2,M} \end{aligned} \tag{2.20}$$

where,

$$\begin{aligned} F_1^t &= -i\frac{\Delta t}{2}U_0(t)C_{J,J+2,M} \\ F_2^t &= i\frac{\Delta t}{2}\left[B_0 J(J+1) - D_0[J(J+1)]^2 - U_0(t)C_{J,J,M}\right] \\ F_3^t &= -i\frac{\Delta t}{2}U_0(t)C_{J,J-2,M}. \end{aligned}$$

Efficient methods of solution exist to solve tridiagonal systems of equations [66]. These methods are used to calculate the unknown amplitudes at the next time step $A_{J,M}^{t+\Delta t}$ from the amplitudes at the present time $A_{J,M}^t$.

With the rotational superposition at the end of the pulse expanded in angular momentum states (recall that different M don't couple so the sum is now over J only)

$$\Psi = \sum_J A_{J,M}|J,M\rangle, \tag{2.21}$$

the field-free evolution of the wave packet becomes

$$\Psi(t) = \sum_J A_{J,M}e^{-iE_J t}|J,M\rangle. \tag{2.22}$$

where E_J is the eigenenergy $E_J = B_0 J(J+1) - D_0[J(J+1)]^2$.

2.1.4 The $\langle\cos^2\theta\rangle$ Measure of Alignment

There is really no unique way to define the degree of alignment of a rotational wave packet or angular distribution. Some intuitively clear ways would be to track, for example, the full width at half maximum or perhaps the standard deviation of the angular distribution. Both of these measures would certainly be good indicators of alignment. However, the standard measure of alignment is defined in a slightly different way and is given by the average value of $\cos^2\theta$

$$\langle\cos^2\theta\rangle = \langle\Psi|\cos^2\theta|\Psi\rangle. \tag{2.23}$$

This measure would give a value of $\langle\cos^2\theta\rangle = 1$ for an angular distribution perfectly peaked along the 'poles' $\theta = 0$ and π, $\langle\cos^2\theta\rangle = 0$ for a distribution peak along the 'equator' $\theta = \pi/2$, and $\langle\cos^2\theta\rangle = 1/3$ for an isotropic distribution evenly distributed across all θ.

During the interaction with the laser pulse, this measure is simply obtained by numerical integration over the computed wave function. For field-free propagation, the time-dependent measure of alignment is given by

$$\begin{aligned}\langle\cos^2\theta\rangle(t) &= \langle\Psi(t)|\cos^2\theta|\Psi(t)\rangle \\ &= \sum_J \Big[|A_{J,M}|^2 C_{J,J,M} \\ &\quad + |A_{J,M}||A_{J+2,M}|\cos\big(\omega_J t + \varphi_{J,J+2}\big)C_{J,J+2,M}\Big]\end{aligned} \tag{2.24}$$

where

$$\omega_J = E_{J+2} - E_J \tag{2.25}$$

and $\varphi_{J,J+2}$ denotes the relative phase between the states $|J, M\rangle$ and $|J+2, M\rangle$ at the start of the field-free evolution. Note that during the field-free evolution the $\langle\cos^2\theta\rangle(t)$ signal is composed of the discrete frequencies ω_J.

The alignment signal is further averaged over an initial Boltzmann distribution of angular momentum states for a given initial temperature T. This is accomplished by calculating the rotational wave-packet dynamics for each initial rotational state in the Boltzmann distribution, and then incoherently averaging the $\langle\cos^2\theta\rangle(t)_{J,M}$ signal from each initial state $|J, M\rangle$ weighted by the Boltzmann probability

$$P_J \sim g_J(2J+1)\exp(-E_J/kT) \tag{2.26}$$

to give

$$\langle\cos^2\theta\rangle(t) = \frac{\sum_{J,M} g_J e^{-E_J/kT}\langle\cos^2\theta\rangle(t)_{J,M}}{\sum_J P_J} \tag{2.27}$$

where the rotational energies are $E_J = B_0 J(J+1) - D_0[J(J+1)]^2$.

2.2 Adiabatic Alignment

2.2.1 Adiabatic Quantum Evolution

The first ideas and experiments using the AC Stark shift for molecular alignment considered the case of adiabatic alignment [20–24]. In this regime, a laser field is slowly turned on such that the molecules can adiabatically adjust to the changing potential energy and "smoothly fall" into the potential wells at $\theta = 0$ and π.

For such adiabatic evolution it is useful to think in terms of eigenstates $\psi_j(t)$ of the instantaneous Hamiltonian $\mathbf{H}(t)$ such that

$$\mathbf{H}(t)\psi_j(t) = E_j(t)\psi_j(t) \tag{2.28}$$

at any particular time t. By turning on the field slowly, one expects that an initially populated eigenstate of the field-free system $\psi_j(0)$ will simply follow the eigenstate $\psi_j(t)$ without making transitions to other states. The criterion for what 'slowly' means in this case is given by the *adiabatic theorem* [67]

$$\left| \frac{\langle \psi_i | \partial \mathbf{H}/\partial t | \psi_j \rangle}{(E_i - E_j)^2} \right|^2 \ll 1 \tag{2.29}$$

which says that the time rate of change of the matrix element of the Hamiltonian divided by the energy separation squared must be small. In (2.29), the level j is the initially populated eigenstate and the level i would be the level with smallest energy difference from the populated eigenstate.

This condition implies that adiabatic evolution is possible as long as there are no level crossings or degeneracies in the level structure during the evolution. Otherwise $E_i - E_j$ would be zero and the adiabatic condition could not be satisfied. This might initially seem to cause a problem for adiabatic alignment since at the beginning of the evolution every J level has $(2J + 1)$ degenerate M sub-levels. Fortunately, the matrix element in the numerator of the adiabatic criterion removes the difficulty: only states to which the populated eigenstate can couple need to be considered.

Since the Hamiltonian in the case of laser alignment does not couple different M states, these degeneracies are not a problem.

For the case of adiabatic alignment, the set of instantaneous eigenstates can be written as $\psi_j = \{|\tilde{J}, M\rangle\}$. This labeling makes clear that each instantaneous eigenstate in the field correlates to a specific $|J, M\rangle$ in the field-free case. Figures 2.3 and 2.4 illustrate this point for the first 6 eigenstates of the $M = 0$ case in N_2. Figure 2.3(a) shows the field-free eigenstates. Figures 2.3(b) and (c) show the corresponding even and odd in-field eigenstates for a laser intensity[1] of $I_0 = 0.5 \times 10^{14}$ W/cm^2 along with the $-U_0 \cos^2\theta$ potential. Such intensity creates a well depth of $U_0 = 54.4$ meV in N_2. Note that the $|\tilde{J}, M\rangle$ states are localized in the potential wells at $\theta = 0$ and π, i.e. they are *aligned* with the direction of the laser field. Furthermore, unlike the field-free states $|J, M\rangle$, the $|\tilde{J}, M\rangle$ states are now organized into even and odd "tunneling pairs" split by the potential barrier at $\theta = \pi/2$.

Figure 2.4 shows the evolution of the eigenenergies for these states as the field strength is changed. It can also be seen on this plot that the neighbouring even and odd states are grouping to form "tunneling pairs" of degenerate energies. These degeneracies, however, do not cause any problems for adiabatic evolution because the even and odd states do not mix. The spectrum for large intensities is seen to approach the spectrum of a harmonic oscillator. In this regime the eigenstates lie deep in the well and a harmonic expansion about the minimum of the well can be used

$$-U_0 \cos^2\theta \approx -U_0 + U_0\theta^2. \tag{2.30}$$

The energy spacings in this limit can then be found by solving the harmonic oscillator problem with the potential (2.30). Note also that the energy spacing become larger as the field strength is increased. This implies that an estimate for adiabatic turn on only needs to consider the field-free levels since, as the field becomes large, the level spacings increase and the adiabatic condition will actually be better fulfilled.

[1]Intensity I_0 in W/cm^2 can be related to $\mathcal{E}^2$ atomic units by: I_0 (in W/cm^2) / 3.5×10^{16} = $\mathcal{E}^2$ (in a.u.).

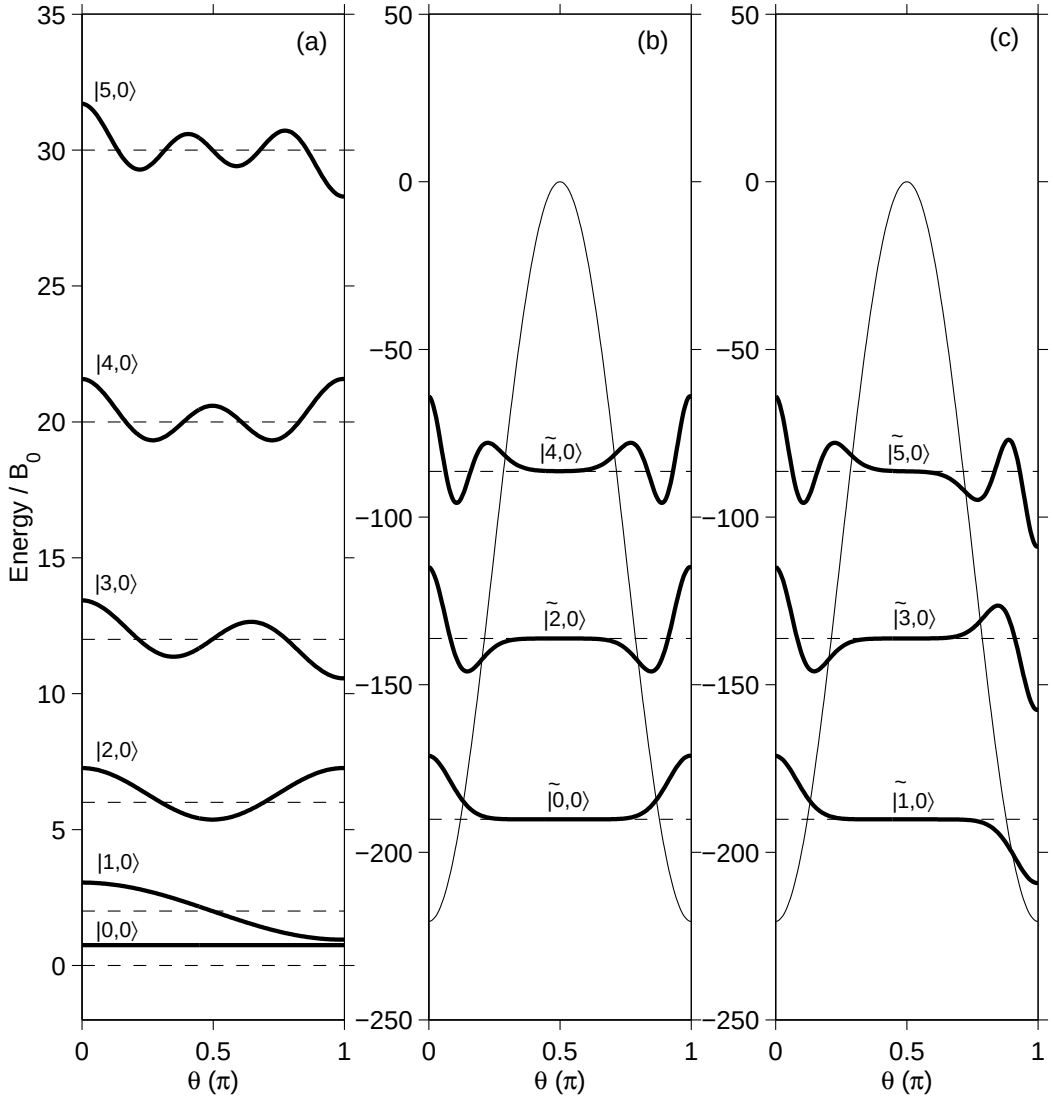

Figure 2.3: Field-free and in-field eigenstates for adiabatic alignment in the case of $M = 0$ for N_2. (a) First six field-free eigenstates $|J, 0\rangle$ centred vertically around the corresponding eigenenergy. Even (b) and odd (c) eigenstates $|\tilde{J}, 0\rangle$ in the laser field with $I_0 = 0.5 \times 10^{14}$ W/cm^2 (well depth $U_0 = 54.4$ meV). The angular potential $-U_0 \cos^2 \theta$ is shown in (b) and (c) for reference.

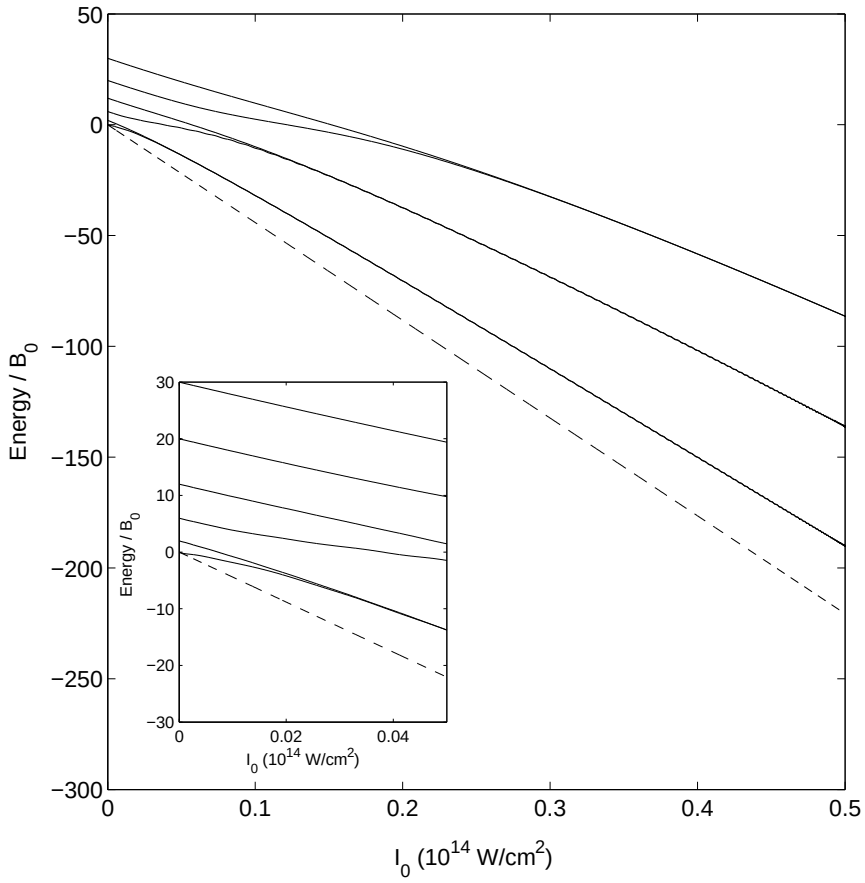

Figure 2.4: Instantaneous eigenenergies of the in-field eigenstates of the first six states of the $M = 0$ case for N_2. The inset shows a larger version of the lower intensity portion of the main plot. The dashed line plots the minimum of the angular potential well for reference.

Having now a general understanding of the level structures and how they apply to the adiabatic evolution, a simple estimate for the turn on time can be made. The smallest level spacing between the field-free states is the energy difference between $J = 0$ and $J = 2$, $\Delta E = E_2 - E_0 \approx 6B_0$. The time scale associated with a transition between these to level will be $\Delta t \sim 2\pi/\Delta E = 2\pi/(6B_0)$. The turn on necessary for adiabatic evolution should then be much larger than this time scale

$$\tau_{on} \gg \frac{1}{B_0}. \tag{2.31}$$

2.2.2 An Example of Adiabatic Alignment: N_2

The condition for adiabatic turn on for N_2 is $\tau_{on} \gg 3$ ps. A pulse duration of $\tau_{on} = 48.4$ ps is chosen to illustrate alignment of N_2 in the adiabatic regime. The results are shown in Figure 2.5. The maximum intensity of the laser pulse was $I_0 = 0.5 \times 10^{14}$ W/cm^2 ($U_0 = 54.4$ meV). Panel (a) shows adiabatic alignment of N_2 at three different temperatures: 20 K (—), 90 K (- -), and 295 K ($\cdots$). The measure of alignment shows a value of $\langle \cos^2 \theta \rangle = 1/3$ before the application of the pulse indicating an initial homogeneous distribution of angles. As the laser pulse interacts with the molecular distribution, the average alignment toward the direction of the laser polarization increases. The colder ensemble reaches a much larger degree of alignment. This is because lower initial J states, having less rotational energy, fall deeper into the angular well and are more localized. The colder initial ensemble consists of more low-J states and hence shows a higher degree of average alignment.

The inset of panel (a) plots the degree of adiabatic alignment of N_2 as a function of laser intensity. The initial alignment at low laser intensities is seen to follow a linear increase. This is the region of perturbative alignment where the wave functions of the initial field-free rotational states are not too strongly distorted. For stronger laser intensities, the alignment deviates from this linear behaviour and is seen to start to saturate. For the present example, strong saturation of the alignment is only seen in the coldest (20 K) distribution.

Figures 2.6(b) and (c) show a couple of representative plots of wave function

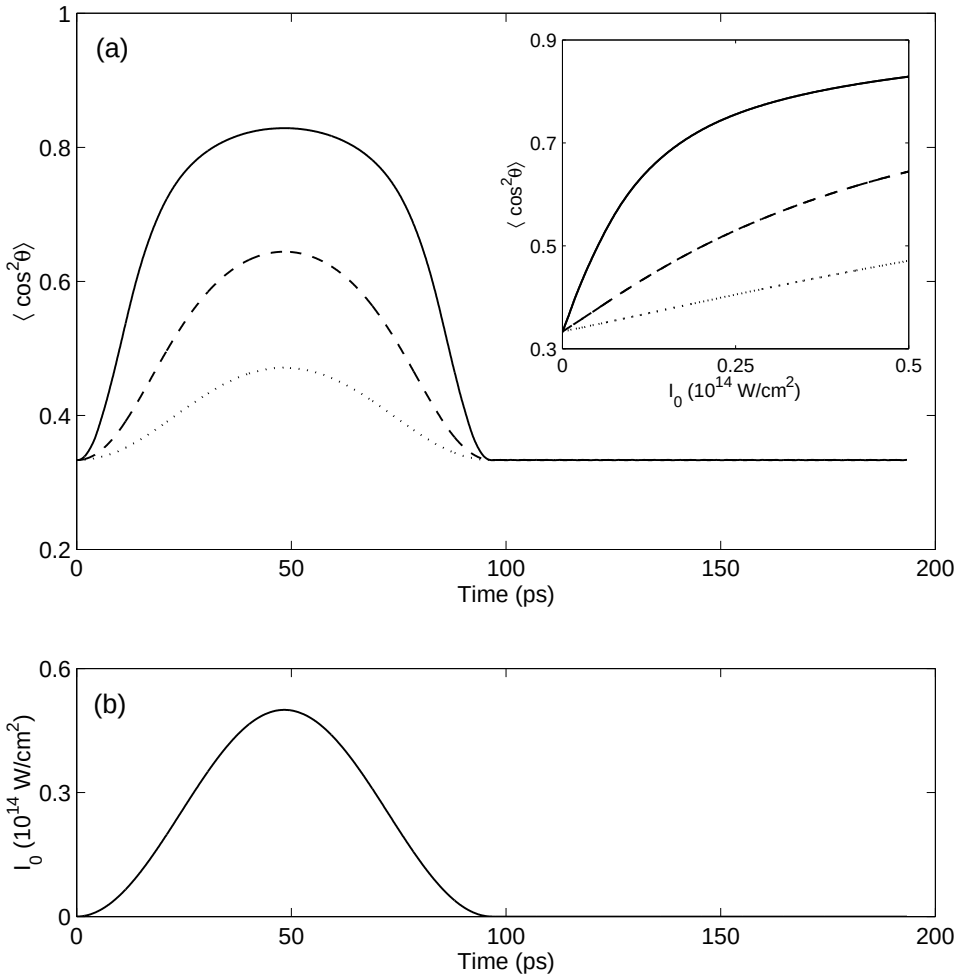

Figure 2.5: Adiabatic alignment of N_2. (a) The average alignment of N_2 for three different temperatures: 20 K (—), 90 K (- -), and 295 K ($\cdots$). The inset shows the average alignment as a function of laser intensity for the same three temperatures. (b) Laser pulse used to calculated the alignment in panel (a).

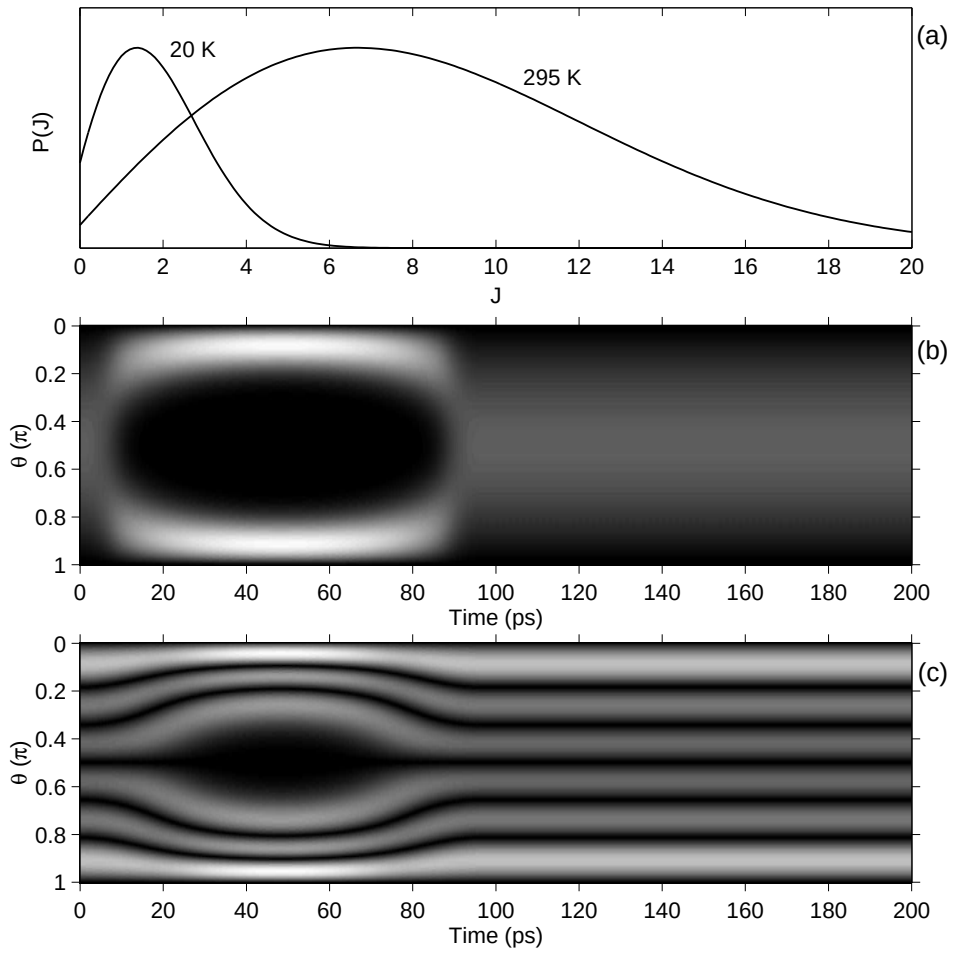

Figure 2.6: Wave function evolution during adiabatic alignment. (a) Distribution of initial $|J\rangle$ states for 20 K and 295 K. (b) and (c) Quantum carpets $|\Psi(\theta, t)|$ for two representative states $|1, 0\rangle$ and $|6, 1\rangle$ corresponding to the maximum of the distributions in (a). Black represents zero amplitude.

evolution, called *quantum carpets* [68–70], for the two initial state $|1,0\rangle$ and $|6,1\rangle$ during the adiabatic alignment process. These quantum carpets are plots of the time-dependent wave function $|\Psi(\theta,t)|$ with amplitude represented by the shading. The distribution of initial $|J\rangle$ states for 20 K and 295 K is shown in panel (a). The g_J factor reflecting the nuclear spin statistics was neglected in these plots for simplicity. The two initial states chosen for the carpets are seen to lie near the maximum of the 20 K and 295 K distributions. In both carpets, the wave function localizes near the $\theta = 0$ and π regions during the application of the laser pulse. The maximum localization occurs at the maximum of the laser pulse. After the pulse is over ($t > 100$ ps), the wave functions return completely to the field-free eigenstates in which they started and no residual excitation remains. This affirms the adiabatic character of this alignment scenario.

2.3 Short-Pulse Alignment

2.3.1 Alignment and Revival Structure

Contrary to adiabatic alignment considered above, the idea of short-pulse alignment is to use the AC Stark shift to give the molecules a rapid 'kick' toward the axis of the laser field. Following the short pulse, the molecules move through a moment of collective alignment. However, since they are field-free, they continue to rotate and the moment of alignment is only short-lived.

The reason for a moment of collective alignment following the short kick can be understood as follows. In the impulsive limit of short pulse excitation, the molecules have no time to move during the interaction time with the laser. Classically, in such a situation, a short pulse imparts angular momentum to a molecule in proportion to the angle θ that the molecule makes with the electric field. The angular momentum transfered is proportional to the torque

$$\Delta J \propto -\frac{dU(\theta)}{d\theta} \propto -\sin(2\theta). \tag{2.32}$$

At small angles, the torque is roughly proportional to -2θ. The molecules will then receive a push proportional to the angle θ. Hence, molecules with larger θ will be able to catch up with the molecules which started closer to $\theta = 0$ and they move through the alignment axis at roughly the same time.

The same process can be understood quantum mechanically. Consider the zero momentum wave function of a rotor in a plane $\Psi(\theta) = 1/\sqrt{2\pi}$. In the limit of a delta-kick $f^2(t) = \delta(t)$, the pulse will add a phase to this wave function of $-U_0 \cos^2\theta$

$$\Psi \longrightarrow e^{-iU_0 \cos^2\theta}\Psi. \tag{2.33}$$

The exponential term can be expanded into a Bessel series using $\exp[-iK\sin\theta] =$

$\sum_n \exp[-in\theta]J_n(K)$ to give

$$e^{-iU_0\cos^2\theta}\Psi = \frac{e^{-iU_0/2}}{\sqrt{2\pi}}\sum_n J_n(U_0/2)e^{-in\pi/2}e^{-i2n\theta}. \tag{2.34}$$

The delta-kick pulse has populated the angular momentum states of the rotor in the plane up to $n \sim U_0/2$. The maximum localization of the wave function following the kick will occur when all the phases of the populated states $e^{-i2n\theta}$ are roughly equal. The phases of these states immediately after the kick are given by $\varphi_n = -n\pi/2$. For the rotor in a plane, the field-free evolution will add the phase of $\varphi_n = B_0 n^2 t$ to the state n. A short period of field-free evolution can then adjust the phases such that approximate localization is reached.

This process of alignment by a short pump pulse is shown in Figure 2.7. In this plot, a pulse with intensity $I_0 = 0.5 \times 10^{14}$ W/cm^2 ($U_0 = 54.4$ meV) and duration $\tau_{on} = 48.4$ fs was used to align N_2. Results are shown for the three temperatures 20 K, 90 K, and 295 K. Note that now the duration of the laser pulse is much less then the characteristic time scale of rotations in N_2 estimated to be $\sim$3 ps indicating that the excitation process is no longer in the adiabatic regime. Consequently, after the laser pulse is over, the wave function will no longer return to the initial field-free eigenstate. Instead, it will be in a superposition of states and will exhibit field-free dynamics. Following the interaction with the laser, the molecules exhibit a short moment of large collective alignment and then quickly dephase away from this aligned configuration due to field-free propagation. Again it is seen that the colder molecular distribution shows better alignment. This is a generic feature of laser induced molecular alignment using either the adiabatic or short-pulse method.

Upon comparing the degree of alignment obtained using the short pulse method (Figure 2.7) with the alignment obtained using the adiabatic method (Figure 2.5) one might conclude that the short-pulse method gives smaller maximum alignment for equal maximum intensities I_0. This, however, is not the case. The degree of alignment obtained in the short-pulse method is sensitive the duration of the pump pulse [see Figure 4.1(a) and related discussion]. Therefore, the alignment can be increased by optimizing the pulse duration. As a result, the degree of alignment

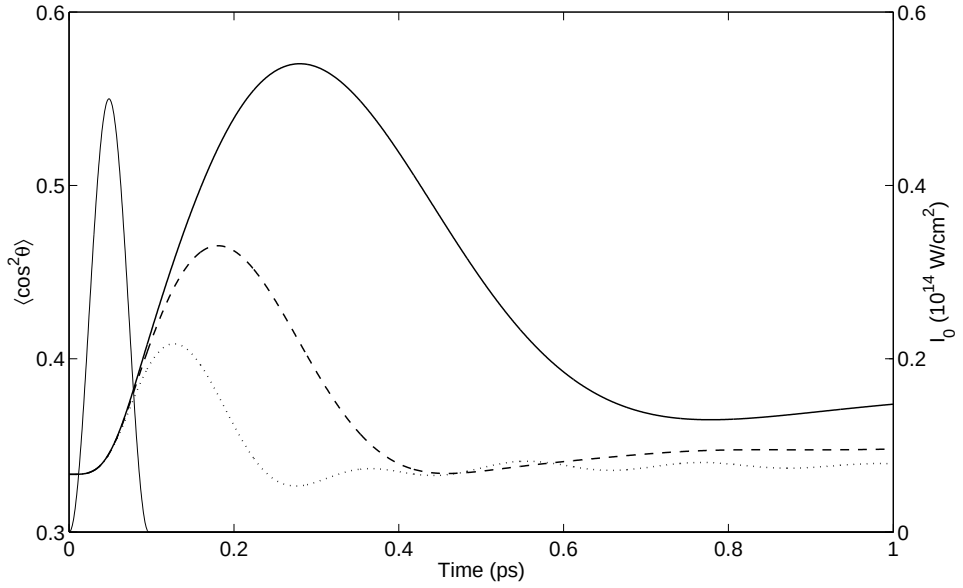

Figure 2.7: The average alignment of N_2 for three different temperatures 20 K (—), 90 K (- -), and 295 K ($\cdots$) following excitation by a short pump pulse (thin line) of intensity $I_0 = 0.5 \times 10^{14}$ W/cm^2 and duration $\tau_{on} = 48.4$ fs.

obtained using the short-pulse method can be comparable to the one obtained with the adiabatic approach. Physically, this optimal pulse duration corresponds to the natural time scale of rotations of the molecules as they fall into the potential well. A simple analogy would be pushing a person on a swing. To be able to transfer the maximum amount of energy to the swing, one must push the swing with the same time scale at which the swing would naturally like to oscillate. Pushing the swing too rapidly or too slowly leads to smaller oscillations then those achieved when pushing in resonance with the swing's natural frequency.

Although the alignment after the short pulse does not persist indefinitely, due to a quantum mechanical effect arising from the discrete spectrum of angular momentum states, the molecules will eventually re-align. When neglecting the rovibrational coupling (i.e $D_0 = 0$), the field-free energies become

$$E_J = B_0 J(J+1). \tag{2.35}$$

Using these energies, the field-free evolution given by Equation (2.22) is

$$\Psi(t) = \sum_J A_J e^{-iB_0 J(J+1)t} |J, M\rangle. \tag{2.36}$$

Setting $t = \pi/B_0$ gives

$$\begin{aligned} \Psi(t = \pi/B_0) &= \sum_J A_J e^{-iB_0 J(J+1)(\pi/B_0)} |J, M\rangle \\ &= \sum_J A_J e^{-iJ(J+1)\pi} |J, M\rangle \\ &= \sum_J A_J |J, M\rangle = \Psi(t = 0) \end{aligned} \tag{2.37}$$

where the fact that $J(J+1)$ is always an even integer and hence $\exp[-iJ(J+1)\pi] = 1$ was used. This shows that after a field-free evolution of $t = \pi/B_0 \equiv T_{rev}$ the wave function will exactly reproduce the wave function at $t = 0$. Such behaviour is called a *wave-packet revival* [71, 72]. Hence, a time of π/B_0 after the point of maximum alignment seen in Figure 2.7 the molecular distribution will again revive to a point of strong alignment.

Figure 2.8(a) shows the further evolution of the short-pulse alignment of N_2 at 90 K seen in Figure 2.7. The revivals of alignment can clearly be seen. The full revival period is $T_{rev} = 8.38$ ps for N_2 and hence the alignment signal begins to repeat every 8.38 ps. There are also moments of strong alignment that are seen to occur at smaller intervals. These correspond to points of *fractional* revivals at times of $t = T_{rev}/4$, $T_{rev}/2$, and $3T_{rev}/4$. These fractional revivals will be further explored in Section 3.2.1.

The difference in amplitudes of the various fractional and full revivals arises from the different weights of the even and odd states in the initial distribution. Figure 2.8(b) and (c) plot the same revival signal including (a) only even states and (c) only odd states. It can be seen on the figure that at the 1/4, 3/4, 5/4,... revivals the odd distribution has maxima (minima) whereas the even distribution has minima (maxima). During the 1/2, 1, 3/2,... revivals, however, the minima and

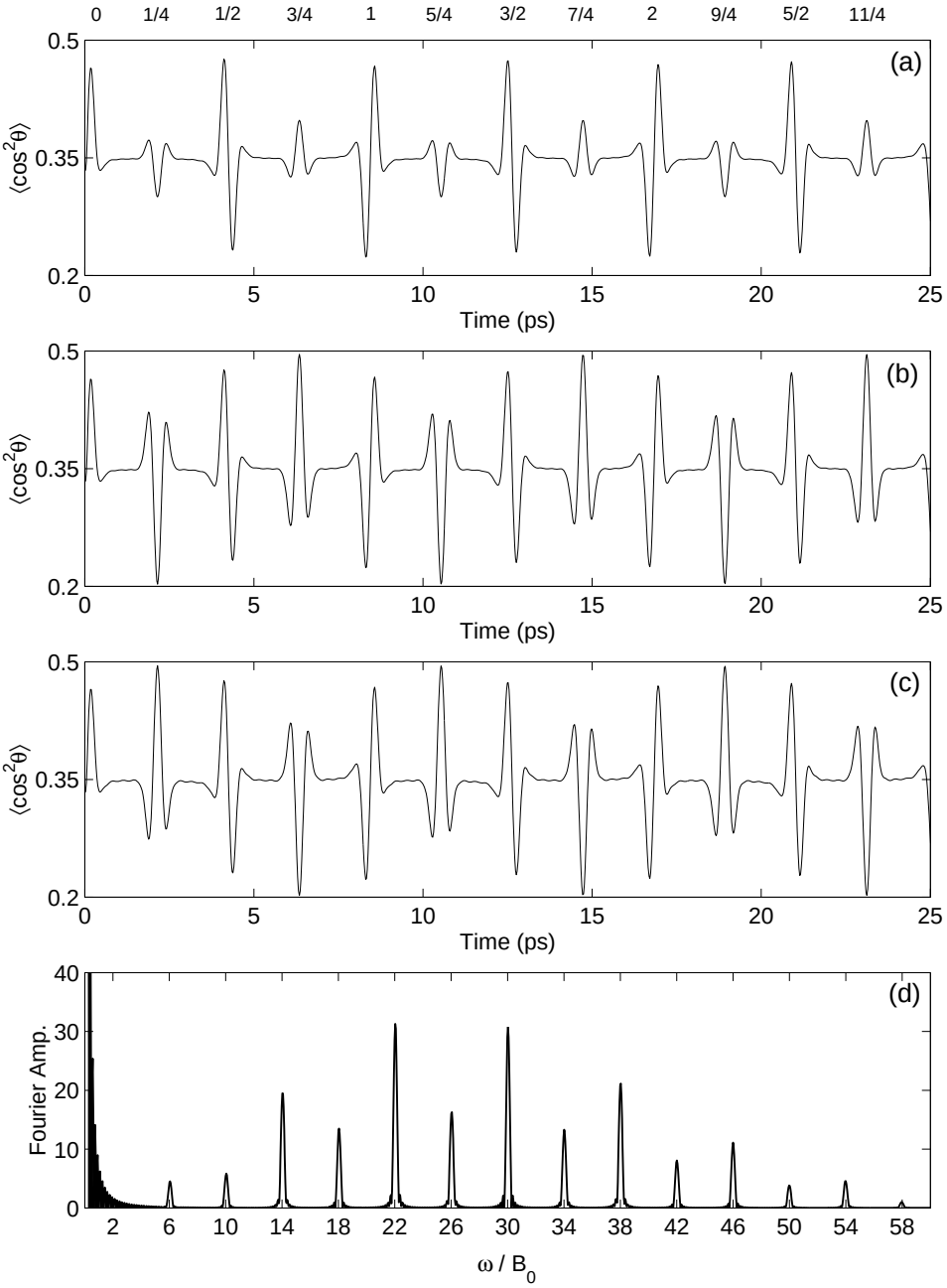

Figure 2.8: Alignment revivals in short-pulse excitation of N_2 at 90 K from a laser pulse with duration 48.4 fs and intensity 0.5×10^{14} W/cm^2 (well depth $U_0 = 54.4$ meV. The fractions appearing above the plot label the revivals for discussion in the text. (a) Alignment signal averaged over all states. (b) Alignment signal including only even states. (c) Alignment signal including only odd states. (d) Fourier transform of complete alignment signal shown in panel (a).

maxima of the even and odd distributions coincide. Hence, when these two signals are averaged together taking into account the weight factor g_J, half the alignment peaks partially cancel while the other half add constructively.

In between the revivals, the alignment does not return to the value of $\langle\cos^2\theta\rangle = 1/3$ characteristic of an isotropic distribution but instead is a bit larger $\langle\cos^2\theta\rangle \approx 0.35$. This deviation from an isotropic distribution is due to the fact that the AC stark interaction spreads each initial angular momentum state to higher J but does not change M. Hence, on average, the populations of $|J, M\rangle$ states will be missing contributions from the $J \approx M$ states for the highest J in the ensemble. Classically, this means that the molecules are rotating preferentially in planes which included the direction of the laser polarization while molecules rotating in the equatorial plane are less probable.

Using the energies (2.35), the beat frequencies $\omega_J = E_{J+2} - E_J$ contained in the alignment signal become

$$\omega_J = B_0(4J + 6). \tag{2.38}$$

Looking at the Fourier transform of the alignment signal $\langle\cos^2\theta\rangle$, as shown in Figure 2.8(d), indeed reveals this set of discrete frequencies. Furthermore, the nuclear spin statistics term g_J weighting the even and odd states, g_J, can also be seen in this spectrum giving rise to the factor of 2 difference in peak heights between the beat frequencies arising from even states ($\omega_{even}/B_0 = 6,\ 14,\ 22,\ 30,...$) and odd states ($\omega_{odd}/B_0 = 10,\ 18,\ 26,\ 34,...$). There is a strong peak building near $\omega = 0$ which represents the DC part of the alignment signal [Equation (2.24)].

Figure 2.9 shows quantum carpets $|\Psi(\theta, t)|$ for the two states $|1, 0\rangle$ [panel (b)] and $|6, 1\rangle$ [panel (c)] during the process of short-pulse alignment. The top panel of the figure plots the average alignment for reference. Unlike the case for adiabatic alignment, here the wave functions exhibit rich dynamics after the pulse is over which accounts for the revivals in the average alignment. Panel (c) plots the angular probability function $|\Psi(\theta, t)|^2 \sin\theta$ averaged over all states in the distribution. Much of the fine scale features seen in the evolution of the individual wave functions is seen to disappear after thermal averaging. Little except the dynamics at the full

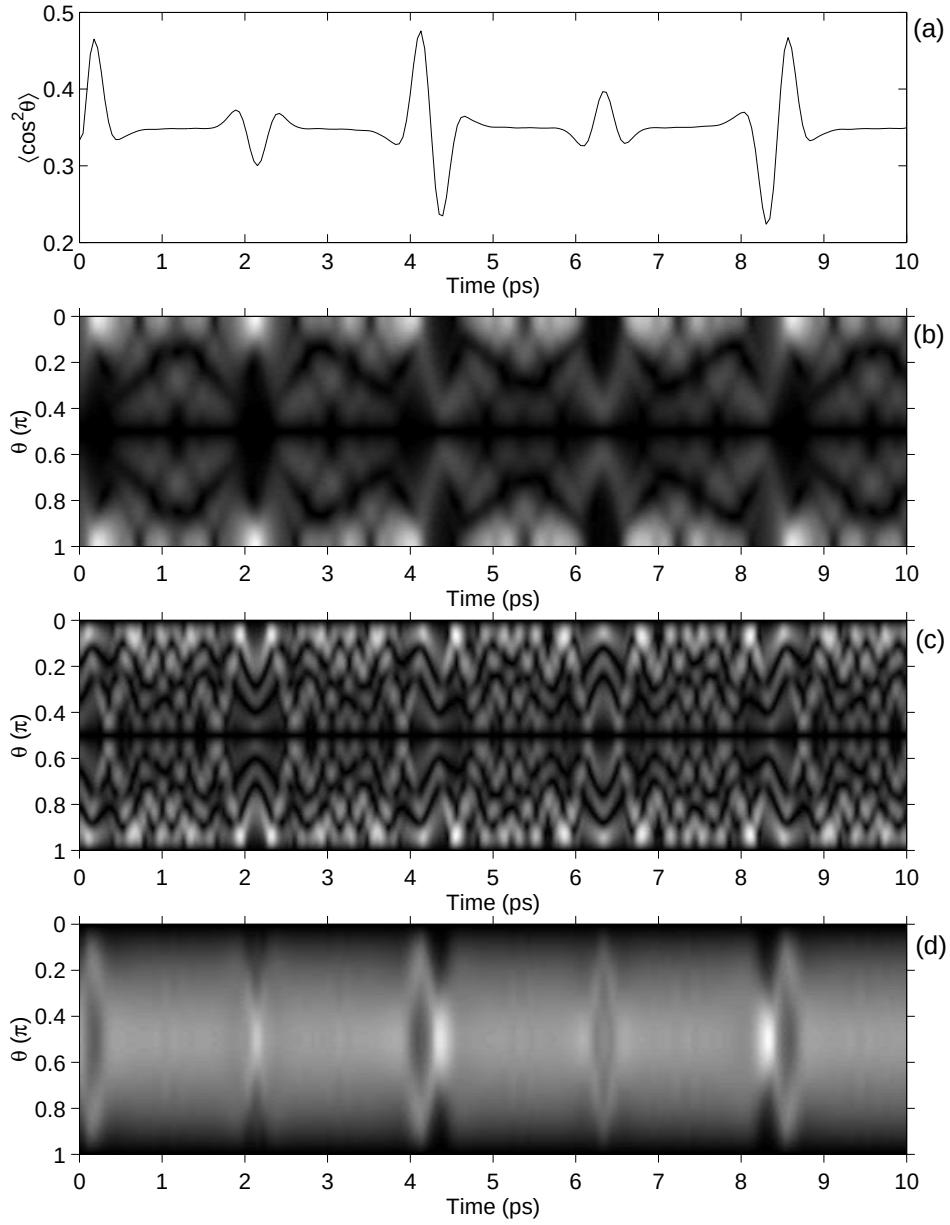

Figure 2.9: Quantum carpets of rotational revivals in short-pulse alignment of N_2 at 90 K. (a) The $\langle \cos^2 \theta \rangle$ measure showing the time-dependent alignment of the distribution. (b) and (c) Quantum carpets $|\Psi(\theta, t)|$ for the two initial states $|1, 0\rangle$ and $|6, 1\rangle$. (d) The angular probability function $|\Psi(\theta, t)|^2 \sin \theta$ averaged over all states in the distribution. In (b), (c), and (d) black represents zero amplitude.

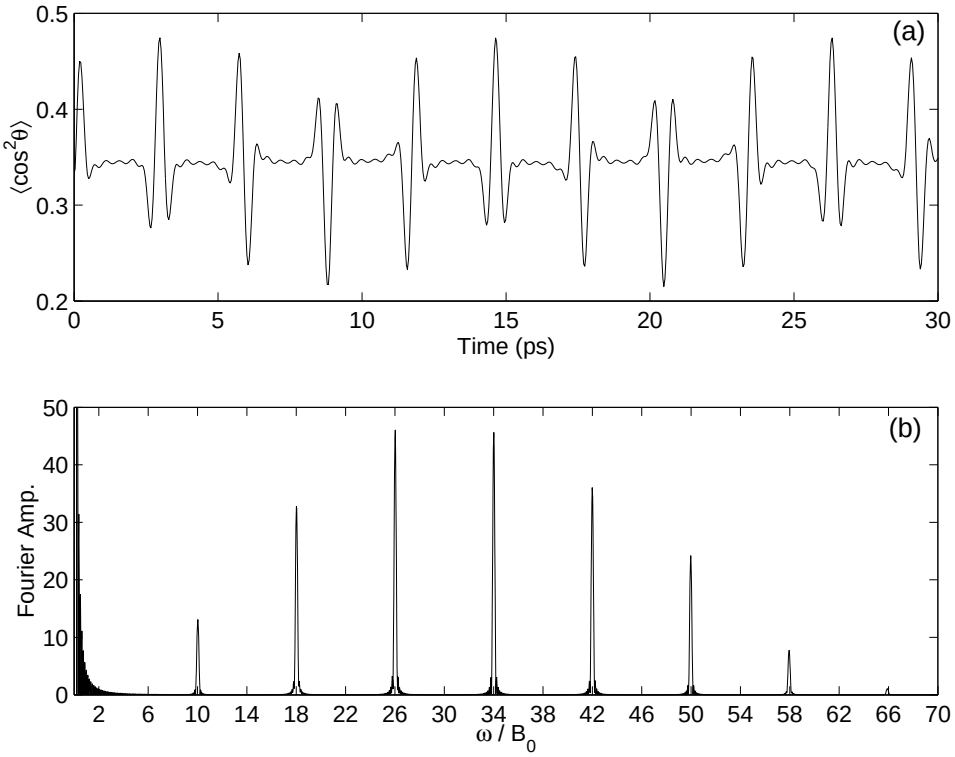

Figure 2.10: Alignment revivals in short-pulse excitation of O_2 at 90 K from a laser pulse with duration 48.4 fs and intensity 0.43×10^{14} W/cm^2 (well depth $U_0 = 54.4$ meV). (a) Alignment signal averaged over the initial distribution which, for O_2, included only odd states. (b) Fourier transform of alignment signal shown in panel (a).

and fractional revivals remains.

Turning now to O_2, a molecule where the spin statistics allows the population of only odd states, a slightly different behaviour can be seen. Figure 2.10(a) shows the calculation of short-pulse excitation of O_2 with a 48.4 fs pulse of intensity $I_0 = 0.43 \times 10^{14}$ W/cm^2 ($U_0 = 54.4$ meV). The full revival time for O_2 is $T_{rev} = 11.7$ ps. Unlike the case for N_2, here the initial distribution includes only odd states and, consequentially, all the revivals appear with roughly equal amplitudes. Turning to the Fourier amplitudes of the revivals, Figure 2.10(b), one sees that only the beat frequencies corresponding to odd initial states ($\omega_{odd}/B_0 = 10, 18, 26, 34, ...$) are

present.

Finally, it should be noted that the inclusion of the rovibrational coupling D_0 in the energies E_J will simply perturb the beat frequencies ω_J a little, adding nonlinearity to the spectrum. This causes small dephasing (or chirping) of the full and fractional revivals for larger times. This effect, as will be seen the following section, is responsible for smearing the shape of the revivals at large revival times.

2.3.2 Experimental Demonstration: N_2 and O_2

Figure 2.11 shows experimentally[2] measured alignment revival dynamics in N_2. This data was collected using a pump-probe time and angle resolved Coulomb explosion technique [31]. The pump pulse creating the alignment in the experiment was estimated to be $\sim$45 fs in duration with a peak intensity of $\sim 1.4 \times 10^{14}$ W/cm^2 and is timed to arrive at $t = 0$ on the plot. Due to technical details of the experimental setup, the angle measured in the experiment is not exactly the polar angle θ which ranges from 0 to π but rather is closer to the azimuthal angle ϕ ranging from 0 to 2π. Due to aperture effects in the resolution of the experiment, however, the experimental angle is somewhat a mixture of the polar and azimuthal angles (for more details refer to [31]). For this reason, the isotropic distribution of angles measured before the arrival of the aligning pulse gives a measure of $\langle \cos^2 \theta \rangle = 1/2$. Note, however, the qualitative agreement between this experimental alignment signal and the simulated signal shown previously [Figure 2.8(a)]. The bottom three panels show experimentally measured angular distributions (thick line) for three moments of time corresponding to maximum and minimum alignment of the revival signal. Note that in these plots the aligning laser points along $\theta = 0$ and is oriented along the horizontal. Also shown for comparison are simulated angular distributions which were calculated for the specific parameters of the experiment. The above estimates for the experimental parameters (intensity, pulse duration, temperature) were fine tuned using a fitting procedure as will be elaborated below.

[2]The experimentally measured data shown in this section was collected by P.W. Dooley, I.V. Litvinyuk, and K.F. Lee [31].

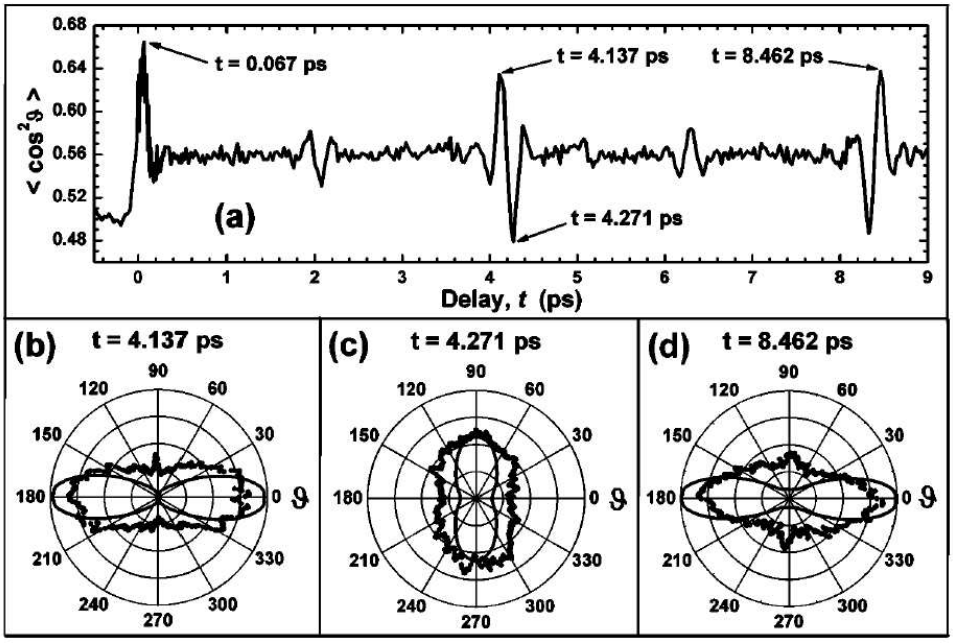

Figure 2.11: (a) Experimentally measured alignment revival structure for N_2. (b)-(d) Plots of measured (thick) and simulated (thin) angular distributions for select times along the revival structure.

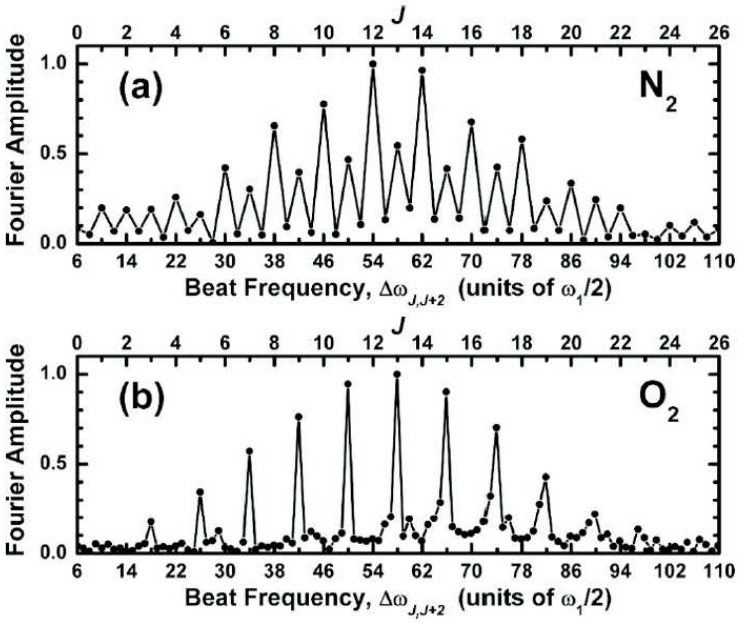

Figure 2.12: Fourier amplitudes of the experimental alignment signal. (a) Data for N_2. (b) Data for O_2.

Figure 2.12(a) shows the measured Fourier amplitudes of the revival signal for N_2 [Figure 2.11(a)]. As expected, the measured Fourier spectrum shows alternating peak heights due to the nuclear spin statistics factor g_J. Furthermore, all the beat frequencies[3] agree with the predicted sequence $\omega_J/B_0 = (4J + 6) = 6, 10, 14, 18, ...$ Figure 2.12(b) shows the Fourier amplitudes for an experimentally measured alignment revival signal in O_2. Here again all frequencies present match the expected sequence. Only frequencies arising from odd states ($\omega_J/B_0 = 10, 18, 26, ...$) are seen.

In order to best simulate the measured alignment revivals, it is necessary to fine tune the estimated experimental parameters. To this end, the initial temperature T, the laser intensity I_0, and the width of the pulse τ_{on} were varied until the calculated revival structure best matched the measured revivals. The comparison was done using the Fourier transform of the alignment signal [Equation (2.24)] which readily

[3]The units of frequency used on the experimental Fourier spectrum, $\omega_1/2$, are the same as those used in the theoretical plots, ω_J/B_0.

gives an estimate of the distribution of populated $|J\rangle$ states through the amplitude terms $|a_J||a_{J+2}|$ labeled by the corresponding frequencies $\omega_J \approx B_0(4J+6)$. In the case of N_2, the best agreement was seen for the laser parameters of $\tau_{on} = 48.4$ fs and $I_0 = 1.7 \times 10^{14}$ W/cm^2 with an initial temperature of 105 K. Figure 2.13 shows the theoretical and experimental alignment signal near the first, second, sixth, and tenth full revivals ($t \approx T_{rev}, 2T_{rev}, 6T_{rev}$, and $10T_{rev}$). Recall that the experimental angle θ and the theoretical θ are not exactly the same angle, and hence that the absolute magnitude of the revival signals is not expected to match. However, the simulations do successfully predict the times of maximum net alignment as well as the shape of each successive revival. The small time shift seen in the tenth revival between the experimental and simulated revival has been ascribed to timing resolution errors in the experiment [73]. As alluded to previously, the stretching or chirping of the revivals at long times is due to the rovibrational coupling term D_0 in the rotational energy spectrum. This term causes small nonlinearities and perturbs the perfect revivals predicted by Equation (2.37). More specifically, when D_0 is included in the energy spectrum of the rotor, the relation $e^{-iE_j t} = 1$ for $t = \pi/B_0$ is no longer exact but now only approximate. Deviations from this relation result in distortions of the wave packet's shape at revivals for large times.

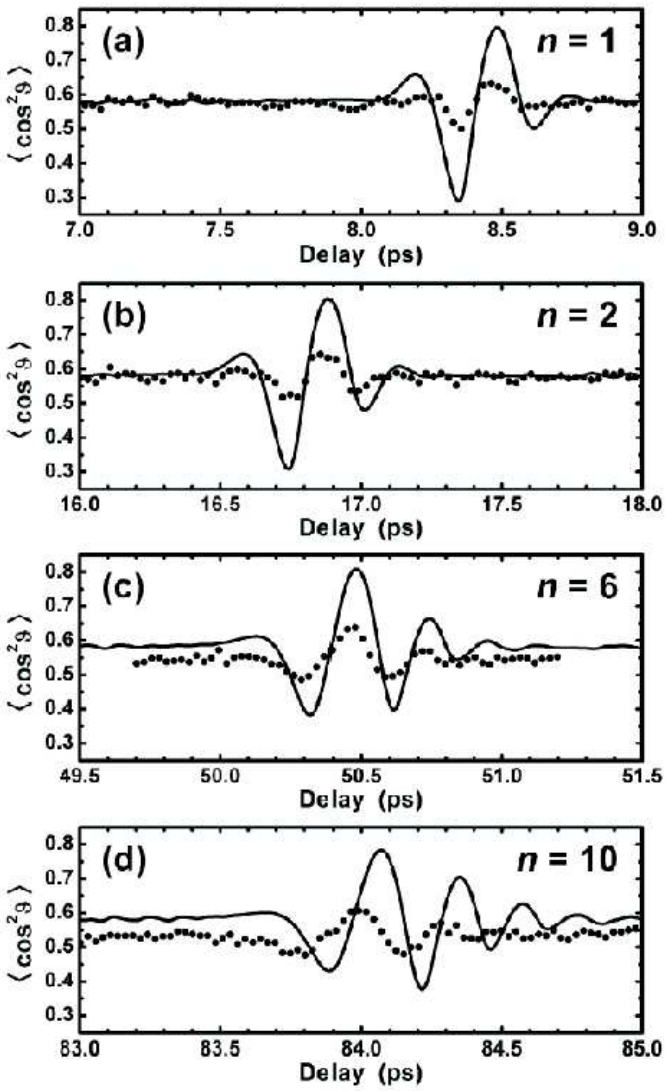

Figure 2.13: Selected full revivals for N_2. The measured time dependence of $\langle \cos^2 \theta \rangle$ (dots) and the simulated results for the (a) first, (b) second, (c) sixth, and (d) tenth wave-packet revivals.

2.4 Two-Pulse Alignment

2.4.1 Recipe for Enhanced Two-Pulse Alignment

The degree of alignment obtained using the above methods of adiabatic and short-pulse excitation are both limited by ionization of the molecule in the laser: there exists a maximum intensity, and hence a maximum aligning strength, beyond which the laser pulse will simply destroy the molecule. A simple way to get around this maximum intensity limit imposed by ionization is to use multiple pulses. Alignment is created with a first pulse, then the distribution is squeezed to a better degree of alignment with subsequent pulses.

This idea of using multiple pulses was first considered by Averbukh and colleagues [36,37]. In [36], the configuration of a pulse train was worked out to quickly and efficiently reach a high level of alignment. In [37], optimal control theory was applied to the specific cases of two-pulse and three-pulse scenarios to find the best pulse parameters for multi-pulse alignment. The solutions found in these studies were repeated in the present work with the inclusion of temperature, which had not been previously considered. The inclusion of temperature changed some minor details of the optimal solutions (for example, in [37] it was found that the best delay between the two pulses in the two-pulse scenario considered was $\sim (1/2)T_{rev}$, but with temperature included the optimal delay becomes $\sim (3/4)T_{rev}$). However, the new optimal multi-pulse solutions retained the same *qualitative* features as the previous 0 K solutions. These features allow one to define a simple recipe for setting up enhanced two-pulse alignment.

In addition to extending the results of [36, 37] to the case of non-zero temperature, many exploratory simulations were carried out for the present work to study two-pulse alignment. An example is shown in Figure 2.14. Here two-pulse alignment of O_2 at 90 K is considered. The two pulses are both of intensity 2×10^{14} W/cm^2, duration $\tau_{on} = 48.4$ fs, and are separated by a delay of τ_d. The x-axis is the time t from the first pulse. The y-axis is the time delay between the two pulses τ_d. The z-axis is the alignment signal $\langle \cos^2 \theta \rangle$. Although this plot is a bit hard to

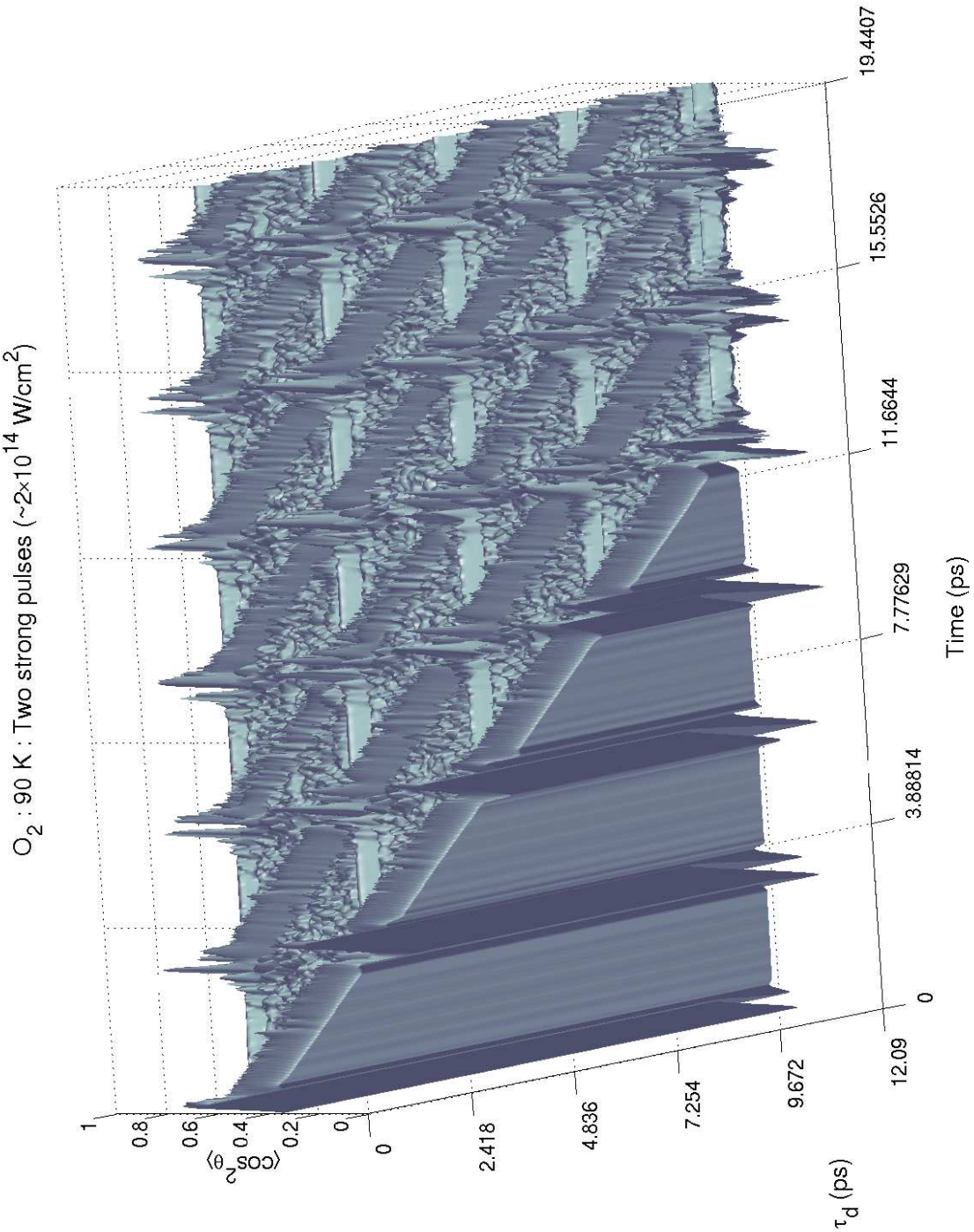

Figure 2.14: A study of two-pulse alignment of O_2.

read at first glance, it represents essentially a complete map of the two-pulse alignment for the given parameters. It can be used to locate the best pulse delay τ_d by comparing the maximum alignment obtained from a single pulse to the maximum alignment obtained following the application of two pulses for all possible delays. In all such studies for a variety of intensities and temperatures, the best two-pulse alignment solutions again showed uniform qualitative features which will now be outlined.

Step 1: Share available energy between pulses

Energy should be balanced such that the first pulse has about 40% of the total available energy. This accomplishes two things: i) Balancing the total energy approximately equally between the two pulses minimizes the maximum instantaneous intensity as seen by the molecules and hence allows one to maximize the total energy pumped into the rotations by setting the energy of each pulse just below the ionization threshold. Any other distribution of energies between the two pulses would necessarily have a lower total energy content, since the strongest pulse can never increase in intensity beyond the ionization threshold. Therefore, diverging far from a roughly 50/50 distribution will simply force the weaker pulse to loose energy without equal increase of energy in the strong pulse. ii) Having a bit more energy in the second pulse was seen to be a generic feature of the optimal solution [37] and this was also found to hold true in the present simulations once temperature effects were included.

Step 2: Find optimal delay for second pulse

The optimal delay of the second pulse is located just before the maximum point of alignment during a strong revival after the first pulse. One then needs to find a strong revival with large alignment created by the first pulse [Figure 2.15(a)]. The optimal delay is then typically just a short time before the maximum as illustrated in Figure 2.15(b). With such a timing, the second pulse catches the molecules as

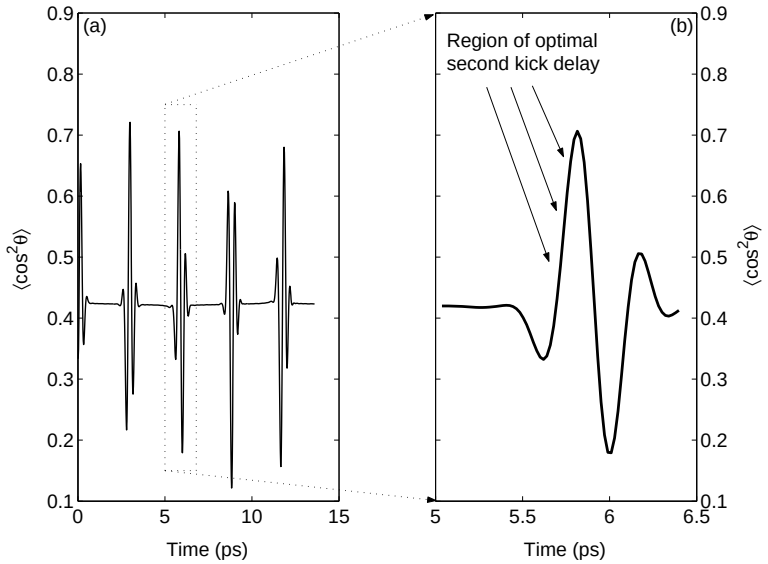

Figure 2.15: (a) Generic alignment signal showing a strong revival chosen for double pulse alignment. (b) Region just before maximum of revival where the optimal second pulse delay is located.

they are approaching the alignment peak and pushes then just a bit more toward an even stronger degree of alignment.

Step 3: Tweak parameters to optimize the alignment

The new point of maximum alignment after the two pulses have been applied should appear a few hundred femtoseconds after the second pulse, Figure 2.16. The region of increased alignment will also appear in subsequent full revivals from this point. Once this maximum is found, the pulse delay as well as the pulse intensity and duration could be tweaked a bit to further optimize the alignment.

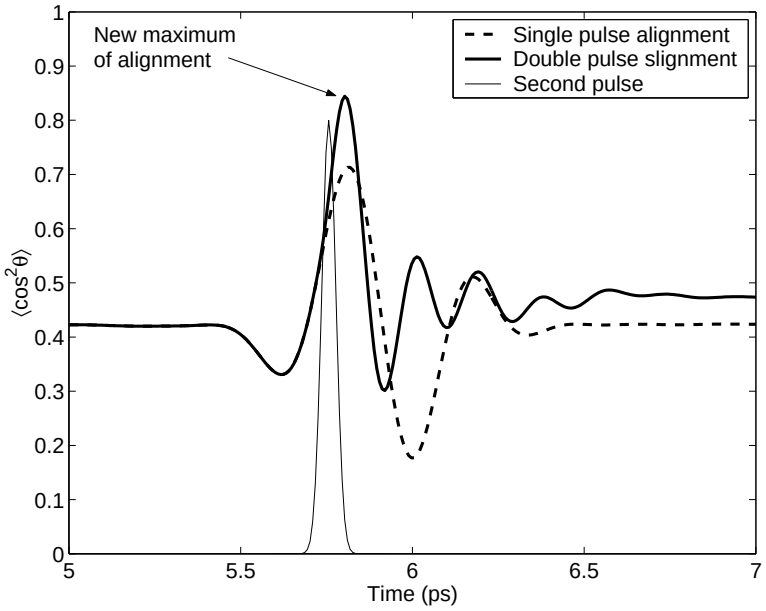

Figure 2.16: Optimal alignment using two pulses. The dashed line shows the alignment using only the first pulse. The thick solid line shows the increased alignment with the inclusion of the second pulse (thin line).

2.4.2 Experimental Demonstration: N_2

This recipe for increased two-pulse alignment has been verified experimentally[4] using the pump-probe time and angle resolved Coulomb explosion technique [38]. Shown in Figure 2.17 is the experimentally measured revival signal for N_2 with the first aligning pulse arriving at $t = 0$ ps. The "\\" region (Pulse 2 Region) shows the particular revival chosen for enhanced two-pulse alignment and is the region in which the second pulse will be placed. The "//" region (Observed Revival), one full revival later than the "\\" region, is the region of observation to measure the increased alignment.

Figure 2.18 shows the results of including the second pulse on the alignment signal. In panel (a), the line 1 shows the alignment in the "\\" region created by the first pulse. The vertical bars show the maximum and minimum alignment attained in the observation region "//" when the second pulse is timed to arrive at the time where the particular bar is located. Panel (b) shows the alignment in the observation region without the second pulse (curve 2), with the pulse located at 8.41 ps (curve $\circ$) which corresponds to the case of maximal increase of alignment, and with the second pulse located at 8.31 ps (curve $\triangle$). The two vertical bars in panel (a) corresponding to these last two cases were plotted with the corresponding shapes as indicators. This experiment shows that the preceding recipe for two-pulse alignment does indeed lead to an enhancement of the alignment signal.

[4]The experimentally measured data shown in this section was again collected by P.W. Dooley, I.V. Litvinyuk, and K.F. Lee [38].

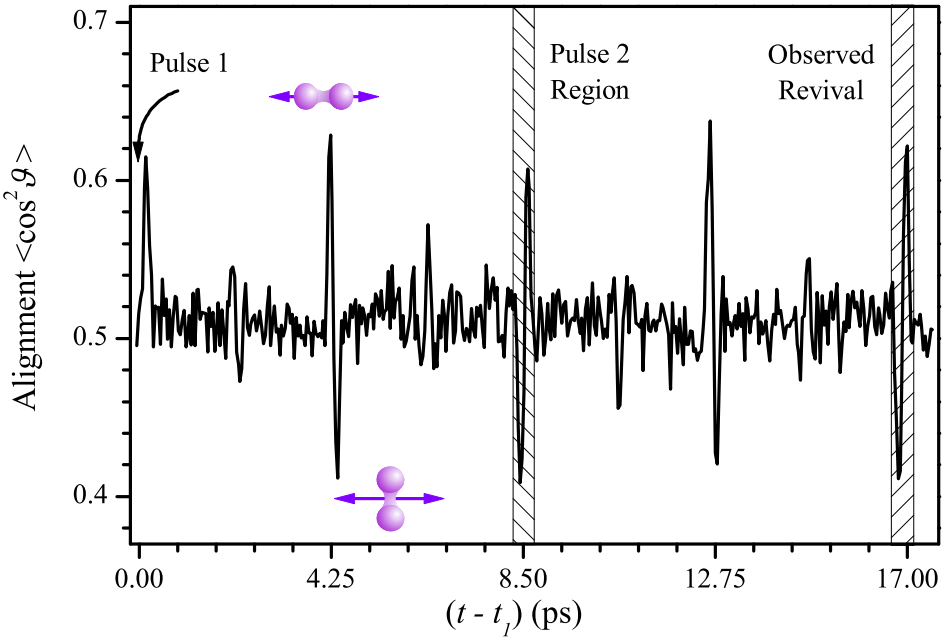

Figure 2.17: Experimental single-pulse revival signal used to choose the timing the second pulse in the two-pulse alignment experiment.

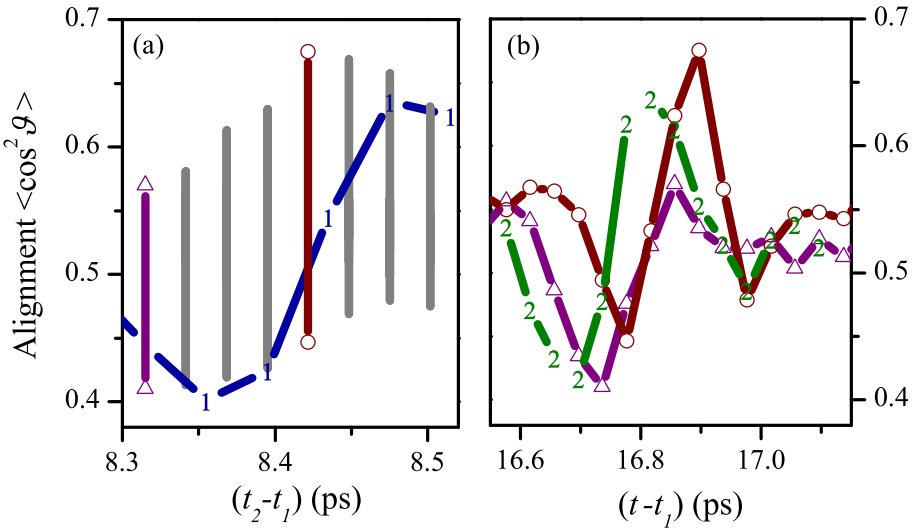

Figure 2.18: Enhanced two-pulse alignment in N_2. (a) Single-pulse alignment signal (curve 1) in the region where the second pulse is to be placed. Vertical bars indicated the maximum and minimum alignment attained in the observation region when the second pulse arrived timed to that point along the revival. (b) Alignment signal in the observation region showing the single-pulse alignment (curve 2), the alignment with the second pulse timed at $t_2 - t_1 = 8.41$ ps (curve $\circ$), and with the second pulse timed at $t_2 - t_1 = 8.32$ ps (curve $\triangle$).

2.5 Switched Wave Packets

2.5.1 Preparation and Switching Effects

Another method of creating field-free alignment, called *switched wave packets*, in a sense mixes the regimes of adiabatic and short-pulse alignment. First, the laser field is slowly turned on to align the molecules, as in adiabatic alignment. Then, at the peak of the field, the pulse is abruptly switched off, projecting these aligned eigenstates immediately onto the field-free basis populating non-stationary wave packets of the field-free system. These wave packets will then continue to evolve field-free exhibiting revival dynamics as in the case of short-pulse alignment.

Figure 2.19 demonstrates this idea for a distribution of N_2 at 50 K (note that only even states were included in this illustrative example.) The pulse shape used (top panel) had a turn-on time of 15 ps, and was turned off instantaneously at the peak of the field. The alignment of the distribution (bottom panel) is seen to adiabatically increase as the field is turned on and exhibit revival dynamics after the truncation of the field. Angular distributions (middle panel) are shown for various points in time given by the position of the distribution along the time.

The requirements for adiabatic turn on have already been discussed. However, in the case of switched wave packets, a condition for the switching time is also needed. The aligned wave packet at the peak of the laser pulse can be expanded in the field-free basis

$$\Psi = \sum_J A_{J,M} |J, M\rangle. \tag{2.39}$$

If the pump pulse were to be instantaneously switched off, as is the case in the example seen in Figure 2.19, the state Ψ would evolve as

$$\Psi(t) = \sum_J A_{J,M} e^{-iB_0 J(J+1)t} |J, M\rangle. \tag{2.40}$$

In a realistic case, however, the switching time can not be made arbitrarily short and the superposition in Equation (2.39) will necessarily be perturbed ($A_{J,M} \rightarrow A'_{J,M}$) by the time the field is off. This means that the degree of alignment obtained in

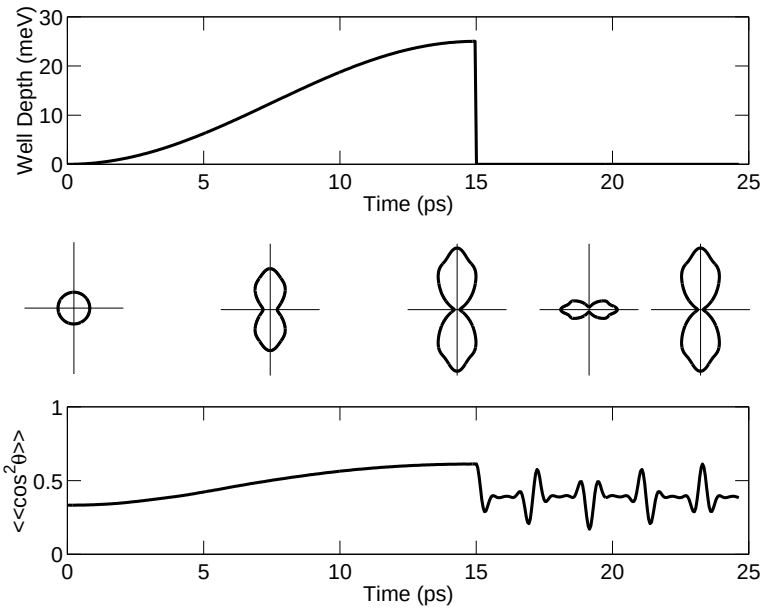

Figure 2.19: Creation of a rotational switched wave packet in N_2 at 50K. Top: The well depth, $U_0(t)$, showing the shape of the aligning laser field. Middle: The averaged angular probability distribution of the ensemble for select times. Bottom: The averaged time-dependent alignment of the ensemble.

the revivals will not match the degree of alignment of the wave packet at the peak of the field. Instead, the alignment during the revival will be lower due to the distortion of the wave packet during the turn-off. However, a good projection of the aligned state at the peak of the laser field can still be made on to the field-free states if the switching time is short enough that the expansion coefficients do not change appreciably $A'_{J,M} \approx A_{J,M}$.

A simple method to estimate the switching time considers the field-free spreading of the ground state wave packet of the molecule in the aligning potential during the time scale of the turn-off. Using a harmonic approximation for the potential near the minimum, the ground state wave function is approximately

$$\Psi_g(\theta) \approx A \exp\left[-\frac{\theta^2}{2a^2}\right] \tag{2.41}$$

where A is a normalization constant and $a^2 = \sqrt{B_0/U_0}$. The field-free spreading of this wave packet with time is

$$\Psi_g(\theta, t) = \frac{aA}{\sqrt{a^2 + i2B_0t}} \exp\left[-\frac{\theta^2}{2(a^2 + i2B_0t)}\right]. \tag{2.42}$$

The time-dependent probability density is

$$|\Psi_g(\theta, t)|^2 = \frac{A^2}{\sqrt{1 + (2B_0t/a)^2}} \exp\left[-\frac{\theta^2}{a^2 + (2B_0t/a)^2}\right]. \tag{2.43}$$

The switching time required for negligible spreading of this wave packet is then found from the denominator of the exponential

$$a^2 > (2B_0\tau_{sw}/a)^2 \quad \longrightarrow \quad \tau_{sw} < \frac{1}{2\sqrt{U_0B_0}}. \tag{2.44}$$

Another method of finding the condition on the switching time comes from the uncertainty principle. The size of the wave packet can be estimated from the ground state of the harmonic approximation which gives $\Delta\theta \approx a = \sqrt[4]{B_0/U_0}$. The

uncertainty principle allows one to estimate the angular momentum

$$\Delta\theta\Delta J \sim 1 \quad \longrightarrow \quad \Delta J \sim 1/\Delta\theta. \tag{2.45}$$

Requiring that the rotor with this angular momentum moves less than, say, the size of the wave packet during the switching time gives

$$\tau_{sw}\Delta J/I < \Delta\theta \quad \longrightarrow \quad \tau_{sw} < I\Delta\theta^2 = \frac{1}{2\sqrt{B_0 U_0}}, \tag{2.46}$$

where $I = 1/(2B_0)$ is the moment of inertia. Again the same estimate for the switching time is found.

2.5.2 Experimental Demonstration: CO_2

Experimental demonstration[5] of a switched wave packet was carried out on a CO_2 gas [34]. The unusually shaped laser pulse required for switched wave packets was created as follows. First, a roughly 200 ps pulse was chosen for the adiabatic turn-on. The abrupt truncation of this pulse was achieved by using a plasma shutter triggered by a strong 80 fs pulse. The femtosecond pulse was timed with the peak of the picosecond pulse [34]. In this setup, the two pulses are focused into a liquid jet. The picosecond pulse is keep at lower intensity and sees a transparent jet. The arrival of the much stronger femtosecond pulse, however, initiates a plasma in the jet immediately creating a reflective surface. This suddenly turns off the transmission of the picosecond pulse. Using such method, a switching time of $\tau_{sw} = 110$ fs was achieved. The resulting picosecond pulse with $\tau_{on} = 125$ ps and sharp turn-off $\tau_{sw} = 110$ fs, as measured in a cross correlation experiment with an 80 fs pulse, is shown in Figure 2.20(a). This pulse fulfills the estimated limits (2.31) and (2.44) for the required adiabatic turn-on $\tau_{on} \gg 14$ ps and fast turn-off $\tau_{sw} \ll 2$ ps.

This laser pulse, with intensity $\sim 10^{11}$ W/cm^2 was then focused into a CO_2 gas at room temperature. The rotational wave packet thus induced in the CO_2 gas was

[5]The experimentally measured data shown in this section was courtesy of J. Underwood and A. Stolow

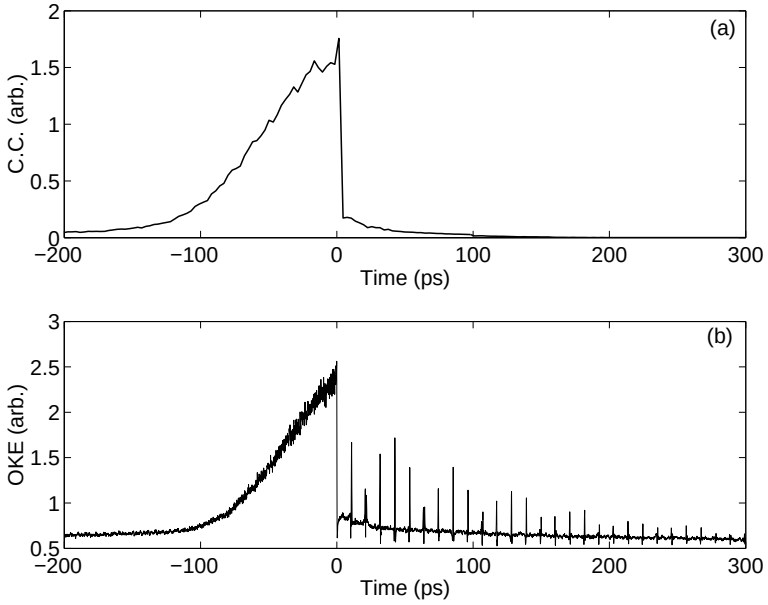

Figure 2.20: Experimental demonstration of a switched wave packet. (a) Cross correlation (C.C.) of the switching 1.064 μm pulse with an 80 fs, 800 nm pulse: τ_{on} = 125 ps, τ_{sw} = 110 fs. (b) Optical Kerr effect signal ($\propto \langle \cos^2 \theta \rangle$) generated by the switching laser pulse when focused into a CO_2 gas.

measured using the Optical Kerr effect (OKE) of a lower intensity 80 fs probe pulse, i.e. the rotation of the polarization of the probe pulse due to the non-homogeneous angular distribution of the molecules. The light from the OKE signal was mixed with a second field of constant amplitude in a heterodyned measurement. In this technique, the measured signal is proportional to [74]

$$\text{signal} \propto [\langle \cos^2 \theta \rangle - 1/3 + C]^2 \tag{2.47}$$

where the constant C describes the heterodyned signal contribution. Figure 2.20(b) plots the observed signal showing the adiabatic increase of the molecular alignment during the slow turn-on of the laser and the subsequent rotational revival dynamics following the abrupt turn-off. The exponential decay of the revival amplitudes was caused by collision-induced decoherence of the rotational wave packets due to the large density of CO_2 used in this particular experiment.

Turning now to the spectrum of this signal, it is first noted that since the basic alignment signal $\langle \cos^2 \theta \rangle$ is squared in the heterodyned measurement (2.47), the expected frequencies will included more than just the ω_J previously discussed. In particular, there will be sum and difference frequencies which arise from the squaring of a signal with multiple frequencies, for example,

$$\begin{aligned} [\cos \omega_1 t + \cos \omega_2 t + C]^2 &= \cos^2 \omega_1 t + \cos^2 \omega_2 t + C^2 + \\ &\quad 2 \cos \omega_1 t \cos \omega_2 t + 2C \cos \omega_1 t + 2C \cos \omega_2 t \\ &= \frac{1}{2}[\cos 2\omega_1 t + \cos 2\omega_2 t + \cos(\omega_1 + \omega_2)t + \cos(\omega_1 - \omega_2)t] + \\ &\quad 2C[\cos \omega_1 t + \cos \omega_2 t + C] + constants. \end{aligned} \tag{2.48}$$

Here, the square of the signal includes the original frequencies (ω_1 and ω_2) plus the sum ($2\omega_1$, $2\omega_2$, and $\omega_1 + \omega_2$) and difference ($\omega_1 - \omega_2$) frequencies.

Figure 2.21 plots both the experimental spectrum of the measured signal along with the results of a simulation modeling the same signal. The simulation used a pulse with $\tau_{on} = 125$ ps, $\tau_{sw} = 110$ fs, and $I_0 = 1 \times 10^{11}$ W/cm$_2$. The initial CO_2 distribution was at room temperature (295 K). Three progressions can be seen in

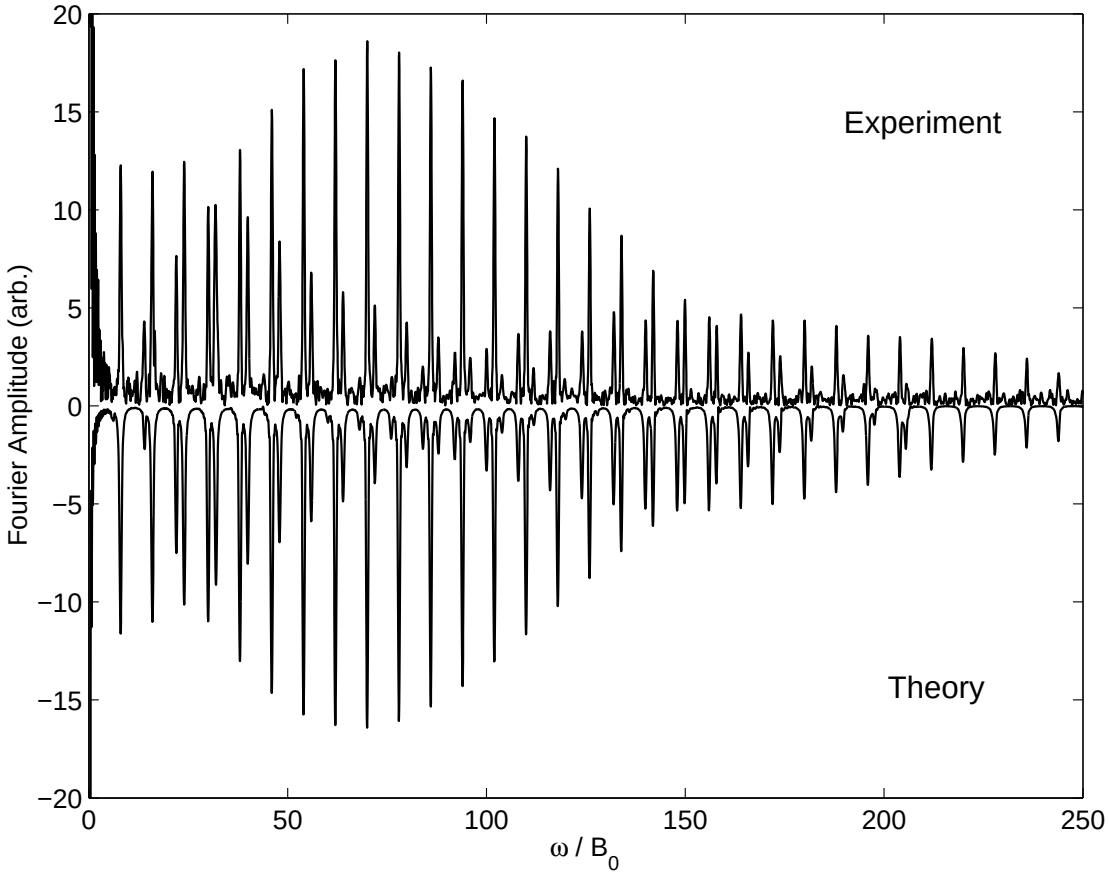

Figure 2.21: Experimental and theoretical Fourier amplitudes for the switched wave packet experiment in CO_2.

the spectra corresponding to the three series of frequencies: the low-ω progression (0 to $\sim$100) is the difference frequencies, the mid-ω progression ($\sim$10 to $\sim$200) is the original frequencies, and the high-ω progression ($\sim$80 to $\sim$250) is the sum frequencies.

Chapter 3

Control of Rotational Wave-Packet Dynamics

3.1 Optical Centrifuge: Forced Acceleration of Molecular Rotations

[*Note: Much of the work presented in this section pertaining to the optical centrifuge was previously submitted to the University of Waterloo as part of the author's* 4^{th} *year undergraduate research project. However, both the author and the author's supervisor of the present Ph.D. thesis wish to included a sample of results on the optical centrifuge for the sake of completeness of the author's work on strong field control of molecular rotations.*]

3.1.1 Basic Idea

Forced molecular rotation induced by strong laser fields, a specific example of molecular control first proposed in [42] and named *optical centrifuge*, was recently observed in experiment [43]. Here, a strong non-resonant laser pulse is used to rotationally accelerate diatomic molecules from low angular momentum states to the

point of rotational dissociation. The process can be understood by a simple extension of the ideas of molecular alignment in strong fields. An anisotropic molecule placed in a linearly polarized field tends to align with the polarization vector via the AC Stark shift. Gently rotating the laser polarization will carry along the molecule in the angular well and force the molecule to rotate as the laser polarization turns.

The process of initial trapping and rotational acceleration to the point of dissociation [44] is outlined in this section. A stability analysis of the optical centrifuge with respect to noise in the experimental laser pulse has also been considered and can be found elsewhere [45].

A linearly polarized laser field with slowly rotating polarization can be written as

$$\vec{\mathcal{E}}(t) = \mathcal{E}_0 f(t) \cos\omega t \big(\hat{\mathbf{x}} \cos\phi_L(t) + \hat{\mathbf{y}} \sin\phi_L(t)\big) \tag{3.1}$$

Here $f(t)$ is the pulse envelop and ω_L is the carrier frequency of the laser pulse. The angle ϕ_L is the instantaneous direction of the laser polarization. To achieve angular acceleration, the laser polarization needs to be smoothly rotated. The discussion considers the case of linear acceleration

$$\phi_L = \frac{\beta t^2}{2} \tag{3.2}$$

in the following calculations. It can be checked that this field is simply a combination of two counter-rotating circularly polarized beams which are oppositely chirped relative to one another

$$\begin{aligned} \vec{\mathcal{E}} &= \frac{\mathcal{E}_0}{2}[\hat{\mathbf{x}} \cos(\omega t + \phi_L(t)) + \hat{\mathbf{y}} \sin(\omega t + \phi_L(t))] \\ &+ \frac{\mathcal{E}_0}{2}[\hat{\mathbf{x}} \cos(\omega t - \phi_L(t)) - \hat{\mathbf{y}} \sin(\omega t - \phi_L(t))]. \end{aligned} \tag{3.3}$$

Consider a linearly polarized field with the polarization slowly rotating in the xy-plane as shown in Figure 3.1. A diatomic molecule placed in this field will tend to align with the laser polarization. The resulting angular potential arising from

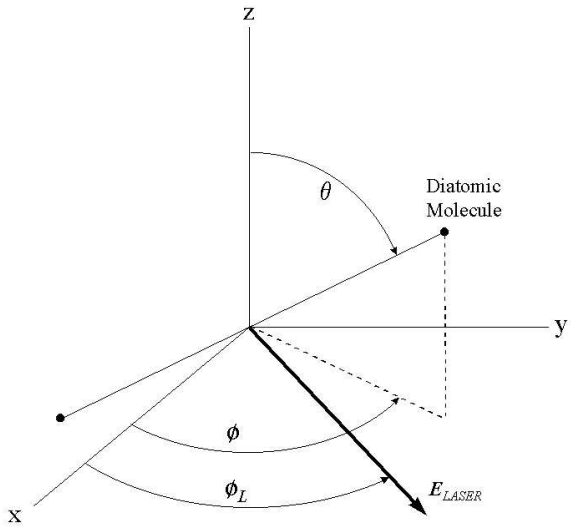

Figure 3.1: Geometry of the problem. θ and ϕ are the angular coordinates of the molecular axis in a fixed frame. E_{LASER} is confined to the xy-plane, with ϕ_L the angle between the laser polarization and the x-axis.

the AC Stark shift is

$$V(\theta, \phi, t) = -U_0(t) \sin^2(\theta) \cos^2(\phi - \phi_L(t)) \tag{3.4}$$

where the depth of the angular potential well, U_0, is

$$U_0(t) = \frac{1}{4}\mathcal{E}^2(t)(\alpha_\parallel - \alpha_\perp). \tag{3.5}$$

The full Hamiltonian of the system, in spherical coordinates, is

$$H = -\frac{\hbar^2}{2\mu}\nabla^2 + V(\theta, \phi, t) + V(R) \tag{3.6}$$

with

$$\nabla^2 = \frac{1}{R^2}\frac{\partial}{\partial R}\left(R^2\frac{\partial}{\partial R}\right) + \frac{1}{R^2 \sin\theta}\frac{\partial}{\partial \theta}\left(\sin\theta\frac{\partial}{\partial \theta}\right) + \frac{1}{R^2 \sin^2\theta}\frac{\partial^2}{\partial \phi^2} \tag{3.7}$$

where μ is the reduced mass of the molecule; $\mu = 17.73$ amu for Cl_2. The bond

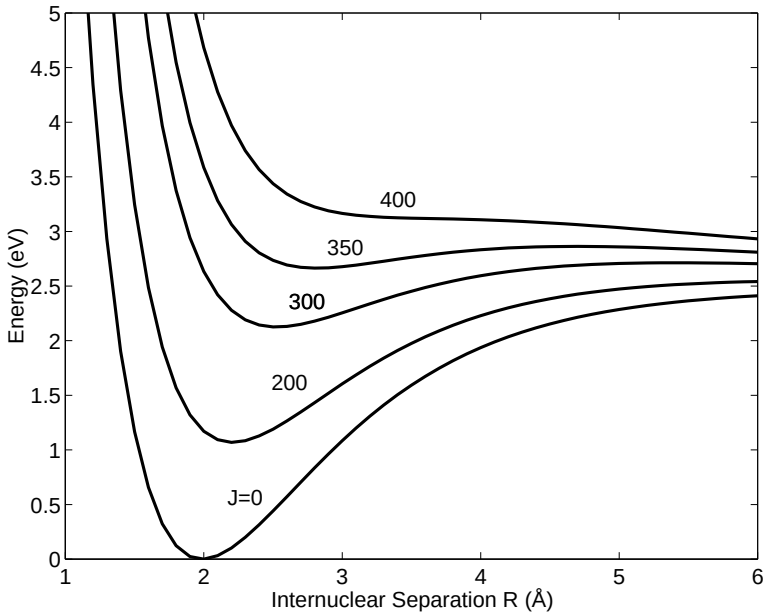

Figure 3.2: Ground state Cl_2 Morse potential including the centrifugal contribution for a subset of J states. By J=400 there is no longer a radial well an the molecule is forced to slide down the potential hill and dissociate.

potential, $V(R)$, is modeled as a Morse potential

$$V(R) = D_0\Big(1 - e^{-\gamma(R-R_e)}\Big)^2 \tag{3.8}$$

with parameters matching Cl_2 ($D_0 = 2.479$ eV, R_e=1.988 Å, $\gamma = 1.07$). Although a full numerical solution to the 3D Hamiltonian is not unattainable, there exist several factors permitting the use of lower dimensional approximations to Equation (3.6), which will greatly reduce the computational workload.

Figure 3.2 shows the radial potential including the centrifugal contribution. During the early stages of the rotational acceleration process, when the angular momentum of the molecule J is smaller than $\sim$100 (in units of $\hbar$), the internuclear separation is not expected to change appreciably, as can be seen in Figure 3.2. If initially the molecule is vibrationally cold, the R dependence of the Hamiltonian (3.6) can be neglected, leading to a 2D rigid rotor model for the early trapping

stages with the Hamiltonian

$$H_{\theta\phi} = -\frac{\hbar^2}{2I}\left(\frac{\partial^2}{\partial\theta^2} + \cot\theta\frac{\partial}{\partial\theta} + \frac{1}{\sin^2\theta}\frac{\partial^2}{\partial\phi^2}\right) + V(\theta,\phi,t). \tag{3.9}$$

Here $I = \mu R_e^2$ is the moment of inertia of the molecule at the bond equilibrium.

As the angular acceleration progresses and the molecule gains angular momentum of J >100, the bond stretch can not be ignored any longer. Furthermore, if any attempt to model dissociation is to be made, the bond stretch must be taken into account. However, at large J another simplification becomes possible. Due to selection rules, the molecules trapped by the centrifuge pulse gain angular momentum only about a well-defined axis given by the direction of propagation of the laser pulse, the z-axis in the chosen frame. This means that the molecules make transitions to and from states where $J \approx J_z$. At values of J >100, these $J \approx J_z$ states are extremely well localized in the xy-plane. The θ dependence of the full Hamiltonian (3.6) can now be neglected and the system can be represented, in 2D polar coordinates, by the Hamiltonian

$$H_{R\phi} = -\frac{\hbar^2}{2\mu}\left(\frac{\partial^2}{\partial R^2} + \frac{1}{R}\frac{\partial}{\partial R} + \frac{1}{R^2}\frac{\partial^2}{\partial\phi^2}\right) + V(\phi,t) + V(R) \tag{3.10}$$

where $V(\phi,t) = V(\theta,\phi,t)\big|_{\theta=\pi/2}$.

To sum up, two model systems are considered. The first is a 3D rigid rotor on a sphere and is useful for the early trapping stages of the centrifuge process. This model will also be used to illustrate a method of single high-J state creation. The second model includes one rotational and one vibrational degree of freedom and is accurate in simulating high J and J_z dissociation dynamics of the optical centrifuge. The two models could be meshed together by fitting the trapped J_z probability distribution near $J \approx 100$. The particular numerical methods used to calculate the quantum evolution of these two models can be found elsewhere [44].

3.1.2 Initial Trapping of Rotational Wave Packet

If the laser polarization rotates with angular acceleration, the molecule will follow provided that the acceleration is not too high. The upper limit on the angular acceleration β follows from the Newton law,

$$\beta \ll {}_{\max}\nabla V/I \approx U_0/I \tag{3.11}$$

where I is the moment of inertia and ${}_{\max}\nabla V \approx U_0$ is the maximum torque that can be applied to a molecule by the angular potential (3.4).

In addition to this restriction on β, there are also important restrictions on the centrifuge turn-on time t_{on} that arise in the case of constant linear chirp considered herein. Firstly, it is impossible in the classical picture to get the highest possible angular trapping efficiency with an instantaneous laser turn-on [42]. To trap molecules of all orientations the laser must sweep out an angle of about π during the turn-on, $\beta t_{on}^2/2 > \pi$. This puts a lower bound on the laser turn-on time. Secondly, there is an upper bound to the turn-on. It comes from the fact that if the turn-on is too long, the angular trap will be rotating too quickly to confine a molecule by the time the pulse has reached full intensity. The kinetic energy gained by a molecule during the laser turn-on is $K \approx U_0/2 + I(\beta t_{on})^2/2$. Here the first term comes from the virial theorem and the second is due to the rotation of the frame. The molecule will stay trapped after the turn-on if $K < U_0$. Together, these two arguments lead to the approximate restriction for t_{on}

$$\sqrt{\frac{2\pi}{\beta}} < t_{on} < \sqrt{\frac{U_0}{I\beta^2}}. \tag{3.12}$$

Choosing a well depth of $U_0 = 50$ meV and using $I_{Cl_2} = 4.564\times10^5$ au, Equation (3.11) leads to $\beta \ll 4.0 \times 10^{-9}$ au. Then by choosing $\beta = 6.0 \times 10^{-10}$ au, which clearly satisfies the previous condition on β, Equation (3.12) leads to $t_{on} \approx 2.5$ ps.

Figure 3.3 shows the dependence of the trapping probability on the laser chirp

β. Here, and for all following trapping simulations, the pulse envelop was

$$f(t) = \begin{cases} \sin^2\left(\frac{\pi t}{2t_{on}}\right) & \text{if } t \leq t_{on} \\ 1 & \text{if } t > t_{on}. \end{cases} \tag{3.13}$$

The laser turn-on was fixed at $t_{on} = 2.42$ ps which is typical in the experiment [43]. The plots were calculated from the time propagation of $H_{\theta\phi}$. An initial state with fixed J and J_z was propagated under the influence of the centrifuge pulse until a good separation between the trapped and non-trapped packets was achieved. The inset on Figure 3.3 shows the time-evolution of a particular case corresponding to $\beta = 6 \times 10^{-10}$ au and an initial angular momentum state of $|J, J_z\rangle = |6, -6\rangle$. The non-trapped part of the wave function forms a wave packet oscillating around $J_z = 0$, while the trapped part of the wave function forms a wave packet that gains angular momentum as it accelerates with the trap. The trapped packet oscillates in the angular well with its harmonic frequency of $\omega_h = \sqrt{2U_0/I}$.

The two curves shown correspond to initial angular momentum states of $|6, 6\rangle$ and $|6, -6\rangle$. $J = 6$ is a typical experimental value of the initial angular momentum of Cl_2 at T = 30 K (note $J \simeq \sqrt{kT/I}$) and $J_z = J$ and -J correspond to the expected highest trapping and lowest trapping cases respectively. For $J_z = J$, the molecule is initially rotating strongly with the angular trap and can be easily trapped. For J_z = -J, the molecule is initially rotating strongly against the angular trap and can easily fall out of the trap. There is seen to be good trapping efficiency (>80%) for the range of $\beta = 2 \times 10^{-10}$ to 6×10^{-10} au, which corresponds to the laser chirp rate $\beta = 0.12$ to 0.35 nm/ps.

The drop in trapping probability seen for values of β greater than the above range, most prominent in the J_z =-6 curve, agrees with the suggested maximum chirp of $\beta \approx U_0/(2\pi I) = 6.3 \times 10^{-10}$ au from [42]. This drop at high β values has a simple explanation. Since t_{on} is fixed in these simulations, increasing β means increasing the angular velocity of the trap at $t = t_{on}$. For large values of β, the laser polarization is spinning too fast by the time the molecule feels the trap for the molecule to respond. The molecule is therefore not trapped.

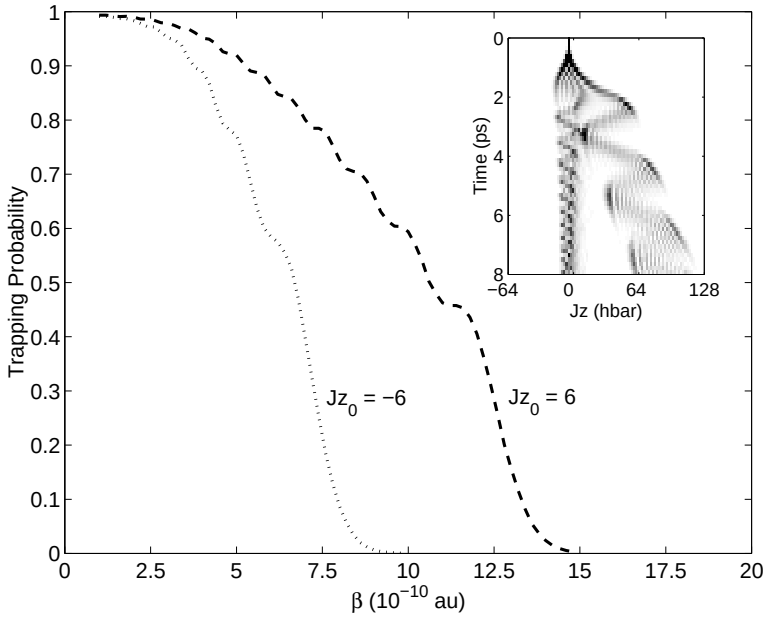

Figure 3.3: The dependence of the trapping probability on the laser chirp β. Laser turn-on was 2.42 ps. $J_z = 6$ and J_z=-6 correspond to the expected highest and lowest trapping probabilities. Inset shows the time-evolution of the J_z probability distribution for a specific case of $|J, J_z\rangle = |6, -6\rangle$. White represents zero amplitude in the plot of wave function evolution.

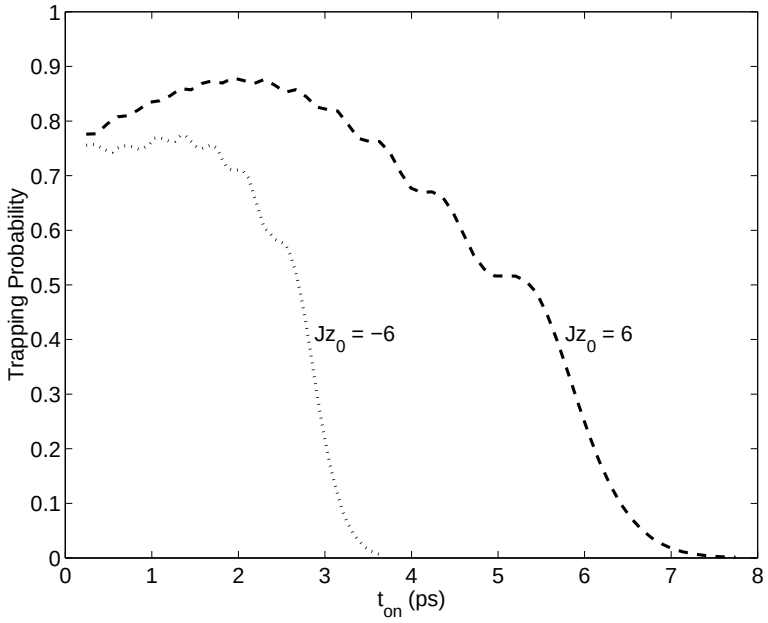

Figure 3.4: The dependence of the trapping probability on the laser turn-on t_{on}. Laser chirp was $\beta = 6 \times 10^{-10}$ au = 0.35 nm/ps. $J_z = 6$ and J_z=-6 correspond to the expected highest and lowest trapping probabilities for $J = 6$.

Figure 3.4 shows the dependence of the trapping probability on the laser turn-on time. The laser chirp was fixed at $\beta = 6 \times 10^{-10}$ au = 0.35 nm/ps. The plots were calculated from the time propagation of $H_{\theta\phi}$. $J_z = 6$ and J_z=-6 correspond again to the expect highest and lowest trapping probabilities.

As previously mentioned, it is impossible to get the highest possible angular trapping efficiency with an instantaneous laser turn-on. This effect is clearly seen in the trapping plots. If the turn-on is too short, the portion of the wave packet located on the peaks of the angular trap does not have time to react and fall into the well and can therefore not be accelerated with the trap. As the turn-on is increased the trapping efficiency is seen to pass through an optimum trapping region. The classically derived estimate for the optimum turn-on is, from (3.12), 2.47 ps $< t_{on} <$ 2.53 ps for the chosen parameters. The actual optimum region is seen to be a bit lower in turn-on value with 1.5 ps $< t_{on} <$ 2.5 ps. For large turn-on values, the laser polarization is once again spinning too fast by the time the molecule feels the angular trap for the molecule to respond, as was the case for large β values, and the molecule will not be trapped.

The optical centrifuge, as can be seen in the inset of Figure 3.3, produces a spread of J states within a single wave packet even when starting from a single rotational state. The reason for this is two fold. Firstly, a quick, highly non-adiabatic laser turn-on is needed to efficiently trap the molecules if a linear chirp is used (see Equation (3.12)). This non-adiabatic trapping process will cause population of many eigenstates states of the angular trap. Secondly, the optical centrifuge lacks any adiabatic return to the field-free system. Such an adiabatic return could be achieved by a slow and smooth turn-off of the laser field. A method of removing this spread of J states from the process, at least when starting from a pure state (i.e. no temperature), will now be outlined.

First, the non-adiabatic turn-on necessary for efficient trapping in the case of linear chirp must be removed. This can be achieved by using adiabatic alignment prior to the centrifuge pulse to prepare the rotational wave packet in a single eigenstate of the potential. The centrifuge pulse would then follow immediately after the peak of the adiabatic alignment pulse. Although the molecules are now starting

in an eigenstate of the angular well as the laser polarization starts to rotate, it must be ensured that a negligible number of transitions between the instantaneous eigenstates are induced by the rotational acceleration of the angular trap. This can easily be ensured by using a small chirp rate β for the centrifuge pulse.

A specific $J = J_z$ state can then be selected by halting the rotational acceleration of the trap at a specific rotational frequency given by

$$\Omega_f \approx \frac{\hbar \tilde{J}_z}{I} \tag{3.14}$$

where Ω_f is the final rotational frequency of the angular trap and $\tilde{J}_z$ is the target $J = J_z$ state. Once the rotational acceleration of the trap has stopped, the trap continues to rotate with frequency Ω_f.

The last step is to slowly and smoothly turn off the laser adiabatically to prevent transitions between the trap states.

Figure 3.5 shows the results of a simulation that illustrates the above outlined scheme. The initial state of the system was the ground state of the angular trap assumed to be prepared by adiabatic alignment. The laser intensity was at full strength at $t = 0$. The trap underwent constant acceleration ($\phi_L = \beta t^2/2$) with $\beta = 0.5 \times 10^{-10}$ au for a time of $t = 0 \rightarrow T_0$ where $T_0 = 36$ ps. For times greater than T_0, the trap was spun at a constant frequency of $\Omega_f = \dot{\phi_L}(T_0) = \beta T_0$ while the laser was slowly turned off over a time of 360 ps. From Equation (3.14), this Ω_f should selectively excited the $J_z \approx 34.25$ state. The simulations show excellent selective population of the $J_z = 36$ state. Analysis of the full $\theta - \phi$ final wave function showed this $J_z = 36$ state to be the $|J, J_z\rangle = |36, 36\rangle$ state.

3.1.3 Rotational Acceleration and Dissociation

Figure 3.6 shows the full evolution of the optical centrifuge propagated with $H_{R\phi}$. The laser underwent a 2.42 ps laser turn-on after which the pulse intensity was left constant for the duration of the centrifuge acceleration process. The initial state was $|n, J_z\rangle = |0, 0\rangle$ where n is the vibrational quantum state of the radial Morse

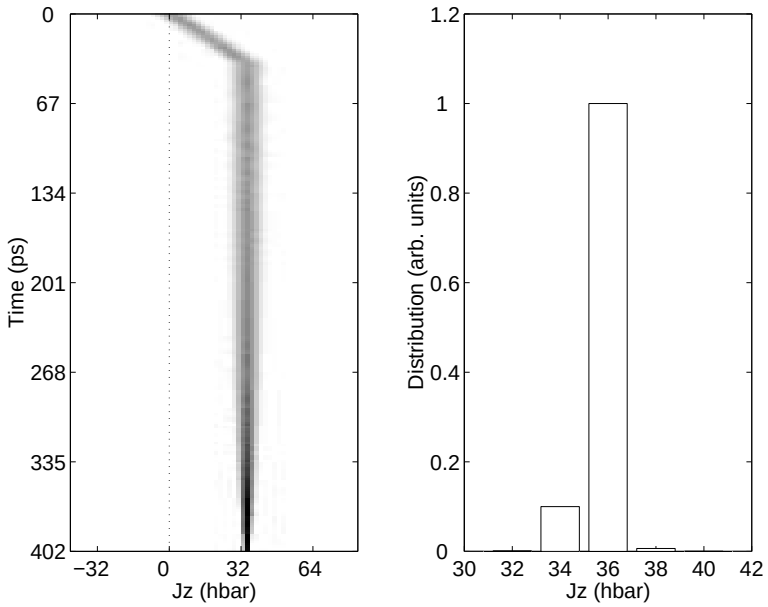

Figure 3.5: Example of single J state creation using a slight variation of the optical centrifuge scheme. Left: Time evolution of the J_z distribution. White represents zero amplitude. Right: Final population of J_Z states after the laser pulse has been turned off.

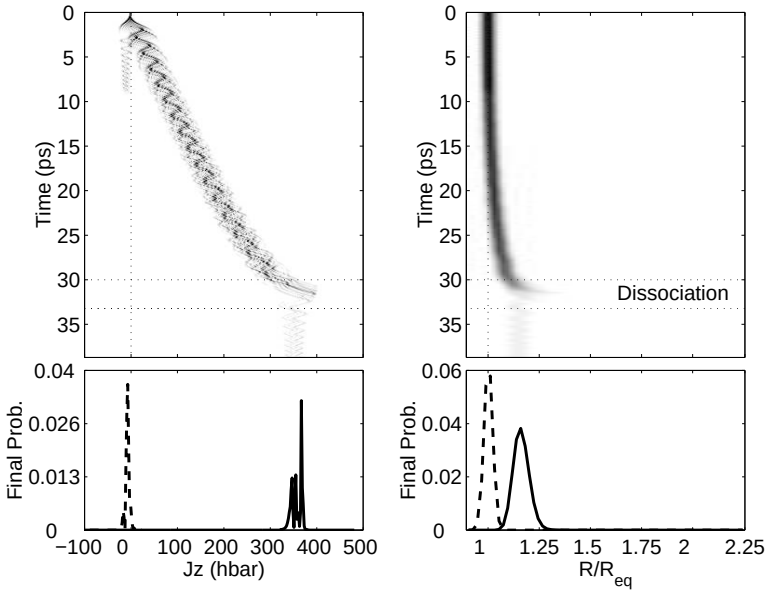

Figure 3.6: Top: Optical centrifuge evolution. Initial State $|n, J_z\rangle = |0, 0\rangle$, $\beta = 4.6 \times 10^{-10}$ au, $U_0 = 50$ meV, and $t_{on} = 2.42$ ps. Low-J_z wave packet was absorbed at about $t = 8.5$ ps. Dissociation probability was 73%. White represents zero amplitude in the plots of wave function evolution. Bottom: Final J_z and R distributions (see text).

potential. Values of $\beta = 4.6 \times 10^{-10}$ au, $U_0 = 50$ meV, and $t_{on} = 2.42$ ps were used. The low-J_z wave packet was absorbed at about $t = 8.5$ ps, as can be seen in the J_z evolution plot. The bottom line plots show the final J_z and R distributions of the undissociated molecules.

The dashed low-J_z, low-R distributions are those of the absorbed part of the wave function that was not angularly trapped and stayed at low-J. They are not calculated exactly, but inferred from the corresponding J_z, R distributions before low-J_z absorption. The solid lines represent the directly calculated final high-J_z and high-R distributions of the trapped but non-dissociated molecules. As the trapped wave packet is accelerated to the point of dissociation and escapes from the radial potential, it quickly spreads and is absorbed at the grid boundary. This is why there is very little density beyond $R/R_{eq} \approx 1.25$. The final calculated dissociation probability was 73%.

The pulse envelope $f(t)$ remains constant after the laser turn-on. Therefore, Figure 3.6 illustrates the features of the centrifuge dynamics that are independent of (possibly non-ideal) pulse profiles and is valid for pulses longer than seen in the experiment [43]. The harmonic oscillations of frequency ω_h present in the trapping simulations (Figure 3.3) are seen to persist coherently up to the dissociation event. J_z increases linearly with time until just before dissociation. This linear regime is indicative of adiabatic evolution. Here the molecules on average follow the acceleration of the trap with small oscillations in the well decoupled from the accelerated motion. Just before dissociation J_z is seen to diverge from linearity. This is consistent with the classical model [42] in which both $\dot{J}_z$ and $-\phi$ undergo a fast increase just before dissociation. The wave packet starts to lag behind the rotating trap, and as a result some of the population falls from the angular trap. This lost population is the wave packet seen at high-J_z and high-R ($R \approx 1.2$) after the dissociation event.

3.2 Control of Revival Dynamics

3.2.1 Rotational Revival Dynamics

As seen in the case of short-pulse and switched wave packet alignment, once a field-free localized wave packet is excited, its initial localization is quickly lost (see Figure 2.9 or Figure 3.7). However, the quantized nature of the spectrum may lead to periodic revivals of the wave packet localization, as is the case for rotational wave packets. As will be seen below, at the moments of fractional revivals the wave packet re-localizes into several equally spaced[1] copies with well-defined relative phases. The central idea of the control scheme presented in this section is to control the wave-packet evolution by inducing relative phase shifts between these wave packet copies at fractional revivals. This approach combines aspects of the control methods of Tannor, and Rice [75] and Brumer and Shapiro [76]. Like the former, it uses wave-packet motion. Like the latter, it relies on the interference of multiple pathways – but here these pathways originate from multiple copies of the initial wave packet. Created at fractional revivals, they play the role of 'slits' in further evolution.

Dealing with wave-packet dynamics, e.g. in molecules, one is often interested in seemingly simple choices: is a molecular axis aligned or not, where is the vibrational wave packet localized, etc. At this level one is only interested in the general aspects of wave-packet evolution rather than detailed information such as amplitudes and phases of specific eigenstates. Such limited information is further justified when the wave packet is created from a thermal initial distribution.

It is shown here that, if only a limited amount of information about the wave-packet position or localization is desired, its evolution can be effectively mapped onto a few-state system. The number of 'states' is determined by the amount of information one wants to track and/or the degree (detail) of control one wants to exert. The existence of the mapping relies on the presence of revival structures

[1] In action-angle variables, these copies are equally spaced in the angle of their motion along the orbit.

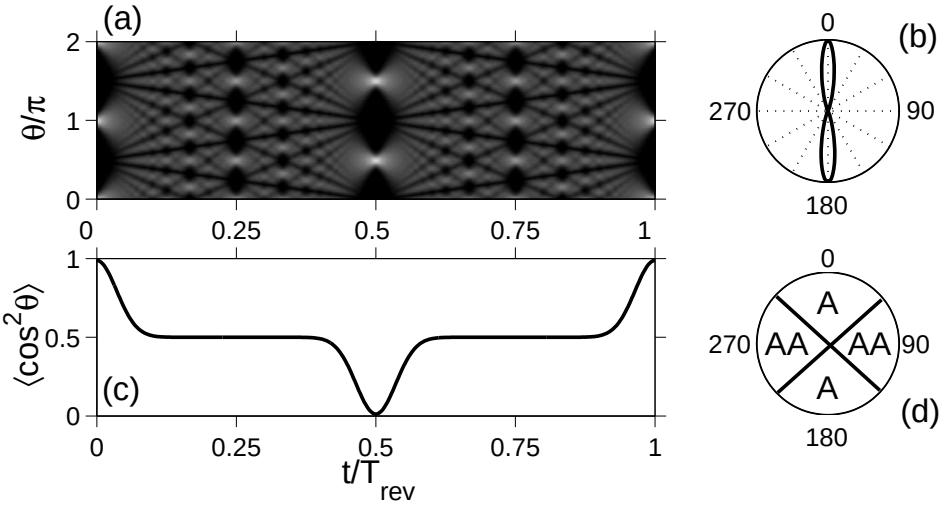

Figure 3.7: (a) Evolution of an angular wave packet initially placed at $\theta = 0$ and $\theta = \pi$. Absolute value of the wave function is shown by brightness with black being zero amplitude. (b) Angular distribution for initial wave packet $\Psi(t)$. (c) Time evolution of wave packet's alignment. (d) Aligned (A) and anti-aligned (AA) regions on the rotor's trajectory.

in the wave-packet dynamics. The basis states of the effective few-state system are time-periodic on the fractional revival time scale, reminiscent of the Floquet states. They track the evolution of the wave-packet symmetries on the spatial and temporal scales of the fractional revivals.

These ideas are illustrate using molecular alignment and orientation as examples. It is shown that relatively weak and short control pulses can implement analogs of $\pi/2$-pulses in the effective few-state system, turning off and on previously induced field-free alignment. Furthermore, these pulses can (partially) convert alignment into field-free orientation.

Consider first a 2D rigid rotor confined to a plane without temperature (3D molecular rotors which include temperature effects are discussed later). Its eigenstates are $\psi_M(\theta) = (1/\sqrt{2\pi})e^{iM\theta}$ and the spectrum is $E_M = BM^2$, where B is the rotational constant. A linearly polarized laser field creates the angular potential $U(\theta) = -U_0 \cos^2\theta$. It aligns the rotor with the direction of laser polarization, creating a rotational wave packet $\Psi(\theta, t = 0) = \sum_M a_M \psi_M(\theta)$ localized near $\theta = 0$

and π. Note that $U(\theta)$ is π-periodic and does not change the parity of the initial state.

Consider now the free evolution of an initially aligned even state $\Psi(\theta, t=0) \propto \exp(-\beta\theta^2)+\exp(-\beta(\theta-\pi)^2)$, which only contains even $M \equiv 2n$ states (the following discussion could have equally used only odd states). The spectrum of this subset is $E_n = 4Bn^2$. The "up" and "down" ($\theta = 0$ and $\theta = \pi$) are not distinguished. Shifting θ by π is equivalent to the 2π rotation of the effective angular variable $\tilde{\theta} = 2\theta$: $\psi_n(\theta) \sim e^{i2n\theta} = e^{in\tilde{\theta}}$.

Figure 3.7(a) shows spreading and revivals of this wave packet $\Psi(t)$ with $\beta = 20.0$ and $B = 1$ [Figure 3.7(b)], over the revival period $T_{rev} \equiv 2\pi/(E_n''/2!) = \pi/2B$. At $T_{rev}/2$ the initial wave packet revives into a single copy shifted by $\pi/2$, and at $T_{rev}/4$ it splits into two copies spaced by $\pi/2$. In general, at $T_{rev}/2K$ the wave packet splits into K copies. These copies are the 'slits' from which the multiple pathways in Figure 3.7(a) originate: modifying their phases controls interferences in the subsequent evolution.

Figure 3.7(c) shows that the commonly used measure of alignment – $\langle\cos^2\theta\rangle$ – provides only limited information about the rich dynamics between the revivals. However, if one is only interested in controlling alignment, this measure is adequate: it is enough to know whether the wave packets are localized in the aligned (A) or anti-aligned (AA) regions [Figure 3.7(d)].

While $|\Psi(t=0)\rangle \equiv |A\rangle$ is maximally localized in the aligned region, $|\Psi(t = T_{rev}/2)\rangle \equiv |AA\rangle$ is maximally localized in the anti-aligned region and is $|A\rangle$ rotated by $\theta = \pi/2$ ($\tilde{\theta} = \pi$). Their free evolution during $T_{rev}/4$ is:

$$e^{-iH_0T_{rev}/4}|A\rangle = \frac{1}{\sqrt{2}}\left[-e^{i\pi/4}|A\rangle + e^{i\pi/4}|AA\rangle\right] \tag{3.15}$$

$$e^{-iH_0T_{rev}/4}|AA\rangle = \frac{1}{\sqrt{2}}\left[-e^{i\pi/4}|AA\rangle + e^{i\pi/4}|A\rangle\right]. \tag{3.16}$$

Superpositions of $|A\rangle$ and $|AA\rangle$ can yield arbitrary alignment between its maximal and minimal values. If one only cares about wave-packet localization in the A or AA regions, as does the measure $\langle\cos^2\theta\rangle$ in Figure 3.7(c), then one needs only

to look at the rotor at multiples of $T_{rev}/4$. Equations (3.15) and (3.16) allow one to find eigenstates of the evolution over $T_{rev}/4$:

$$|0\rangle = \frac{1}{\sqrt{2}}\left[|A\rangle + |AA\rangle\right]; \qquad |1\rangle = \frac{1}{\sqrt{2}}\left[|A\rangle - |AA\rangle\right]. \tag{3.17}$$

These are analogs of the Floquet states: each revives at every multiple of $T_{rev}/4$, up to a global phase which defines the quasienergy of the state. Using Equations (3.15) and (3.16) one can check that the quasienergies are $\epsilon_0 = 0$ for $|0\rangle$ and $\epsilon_1 = 2\pi/T_{rev}$ for $|1\rangle$. Figures 3.8(a) and (b) shows the evolution of $|0\rangle$ and $|1\rangle$ for the 2D rotor. They reproduce themselves every $T_{rev}/4$; the dynamics in between remains unnoticed by $\langle\cos^2\theta\rangle$.

3.2.2 Control by Phase Shifts

The field-free alignment revivals can be switched on or off by controlling the relative phase of the aligned and anti-aligned wave packets at $T_{rev}/4$. Indeed, the field-free evolution turns the initially aligned state $|A\rangle \propto |0\rangle + |1\rangle$ (Figure 3.7) into $|0\rangle - i|1\rangle$ at $T_{rev}/4$, with anti-aligned lobes shifted by $\pi/2$ relative to the aligned ones. Adding $\pi/2$ phase to the aligned lobes transforms the state $(|0\rangle - i|1\rangle)/\sqrt{2}$ to $|0\rangle$ (up to a global phase), switching off alignment revivals. In Figure 3.8(c) and 3.8(d) an instantaneous phase kick $K(\theta) = \exp\left[i(\pi/2)\cos^2\theta\right]$, i.e. $\Psi(\theta) \rightarrow K(\theta)\Psi(\theta)$ was applied at $t = T_{rev} + T_{rev/4}$. The control pulse stops the evolution observed by the $\langle\cos^2\theta\rangle$ measure [Figure 3.8(d)]. Adding the $\pm\pi/2$ phase to these lobes again at $t = 2T_{rev} + 3T_{rev/4}$ changes $|0\rangle$ back to $|0\rangle \pm i|1\rangle$, resurrecting the revivals.

Thus, given the ability to perform phase operations on the wave packets, the rotor dynamics at the level of the $\langle\cos^2\theta\rangle$ measure could be treated and controlled as if dealing with only a two-level system. A short linearly polarized pulse acting on a polarizable molecule which turns $V(\theta, t) = -U(t)\cos^2\theta$ on and off before the wave packets had a chance to move imparts the phase $\delta\varphi = \exp[-i\int V(\theta, t)dt]$ where the integral extends over the duration of the pulse. $\delta\varphi$ can be used to induce phase shifts between different packets at fractional revivals. Results of finite-time control

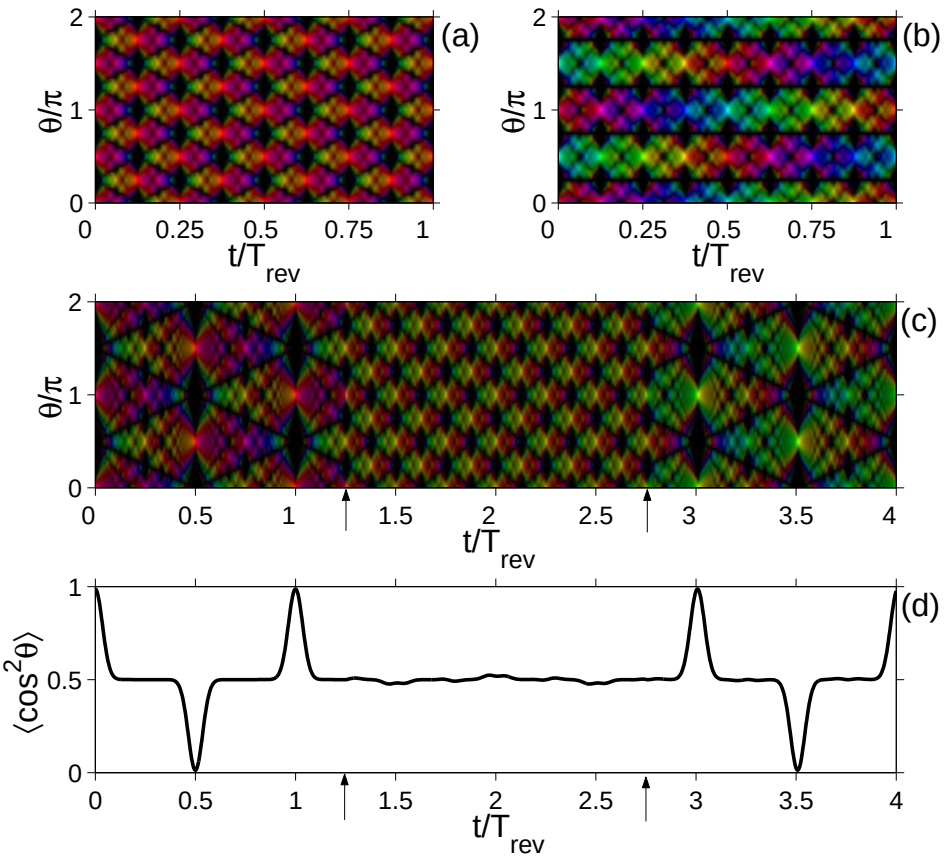

Figure 3.8: (a,b) Evolution of the states $|0\rangle$ and $|1\rangle$ on the revival time scale. Wavefunction amplitude is shown by brightness and the phase is shown by color (or hue in the HSL color system) (c,d) Evolution of the wave function and of $\langle \cos^2 \theta \rangle$ for the alignment being switched off and on. Arrows indicate the moments when the laser pulses are applied.

pulses acting on a thermal ensemble of O_2 molecules are shown below (Figure 3.10).

In addition to controlling alignment dynamics, this control scheme can be extended to control *orientation* dynamics of dipolar molecules. For homonuclear diatomics, there is nothing to distinguish "up" from "down" once the molecule is aligned. However, heteronuclear diatomics, once aligned, can still see a difference between "up" and "down": one aligned configuration of the heteronuclear would have atom A on top and atom B on the bottom, while the other configuration would have atom B on top and A on the bottom. Forcing all the heteronuclear molecules into the same configuration, for example having all A atoms on top, would be called orientation.

So far only a rotor without the permanent dipole moment not distinguishing between "up" and "down" directions in Figure 3.7(d) has been considered considered. Consequently, only even $M = 2n$ were used. Consider now an oriented rotor with a permanent dipole μ and spectrum $E(M) = BM^2$ where M is both even and odd. The revival period now is $T_{rev} \equiv 2\pi/(E''_M/2!) = 2\pi/B$. Similar to alignment, the evolution can be described on the most coarse-grained scale as a succession of superpositions of oriented $|up\rangle$ and anti-oriented $|down\rangle$ states, with basis states $|0'\rangle = (|up\rangle + |down\rangle)/\sqrt{2}$ and $|1'\rangle = (|up\rangle - |down\rangle)/\sqrt{2}$. Up to the replacing $\theta \Leftrightarrow \tilde{\theta}$, the quantum carpets for $|0'\rangle$ and $|1'\rangle$ are qualitatively similar to those in Figures 3.7 and 3.8.

At $T_{rev}/4$ the oriented state $|up\rangle = (|0'\rangle + |1'\rangle)/\sqrt{2}$ becomes $(|0'\rangle - i|1'\rangle)/sqrt2$ and is similar to an aligned state. This suggests that an aligned state can be converted into the oriented one. If the aligned state is made of even M, it looks like $|0'\rangle$ and is converted into $(|0'\rangle - i|1'\rangle)/sqrt2$ by a $\pi/2$ relative phase shift of the "up" lobe. Further free evolution turns it successfully into $|down\rangle$ (anti-oriented), $(|0'\rangle + i|1'\rangle)/sqrt2$ and $|up\rangle$ (oriented) after $T_{rev}/4$, $T_{rev}/2$, and $3T_{rev}/4$ respectively. The required phase shift can be imparted by a "half-cycle" THz pulse [77, 78] interacting with a permanent dipole, $V(\theta, t) = -\mu\mathcal{E}(t)\cos\theta$.

Initial temperature adds a serious complication: for odd M the aligned state is similar to $|1'\rangle$. The same $\pi/2$ relative phase shift of the upper lobe converts it into $(|0'\rangle + i|1'\rangle)/sqrt2$, yielding $|up\rangle$ (oriented), $(|0'\rangle - i|1'\rangle)/sqrt2$ and $|down\rangle$ (anti-

oriented) after $T_{rev}/4$, $T_{rev}/2$, and $3T_{rev}/4$ respectively. Equal incoherent mixture of $|0'\rangle$ and $|1'\rangle$ (thermal ensemble) yields zero net orientation at these times.

This difficulty is overcome by manipulating the wave-packet interferences at a finer time scale, applying phase shifts at multiples of $T_{rev}/8$ rather than $T_{rev}/4$. To describe arbitrary revival pattern at multiples of $T_{rev}/8$, one must break the orbit $\theta = 0..2\pi$ into four parts and look at the superpositions of the four localized states, $|right\rangle$, $|left\rangle$, $|up\rangle$, and $|down\rangle$. Diagonalizing $\exp[-iH_0T_{rev}/8]$ as a 4×4 matrix in the basis of these states, four Floquet-like eigenstates which revive every $T_{rev}/8$ are found:[2]

$$\begin{aligned}
|00\rangle &= (|up\rangle + |left\rangle + |down\rangle + |right\rangle)/2 \\
|01\rangle &= (|up\rangle + |left\rangle - |down\rangle - |right\rangle)/2 \\
|10\rangle &= (|up\rangle - |left\rangle + |down\rangle - |right\rangle)/2 \\
|11\rangle &= (|up\rangle - |left\rangle - |down\rangle + |right\rangle)/2
\end{aligned} \tag{3.18}$$

All four orthogonal states are either odd or even on the whole orbit $0..2\pi$ and on each of its halves. The state $|00\rangle$ has quasienergy $\epsilon_{00} = 0$, the states $|01\rangle$ and $|11\rangle$ have $\epsilon_{01} = \epsilon_{10} = 2\pi/T_{rev}$, and $\epsilon_{11} = 8\pi/T_{rev}$.

The two aligned states are expressed in this basis as $|0'\rangle = (|00\rangle + |10\rangle)/\sqrt{2}$, and $|1'\rangle = (|01\rangle + |11\rangle)/\sqrt{2}$. Their evolution at $T_{rev}/8$ and $3T_{rev}/8$ is different: $|0'\rangle$ revives at the equator ($\theta = \pi/2, 3\pi/2$) while $|1'\rangle$ revives at the poles ($\theta = 0, \pi$) [Figure 3.9(a) and (b)]. The half-cycle pulse $U(\theta, t) = -\mu E(t) \cos\theta$ applied, say, at $3T_{rev}/8$ imparts the phase shift to the two lobes of $|1'\rangle$ while inducing no relative phase shift to the two lobes of $|0'\rangle$. After $T_{rev}/4$, the state $|1'\rangle$ becomes oriented while $|0'\rangle$ is again localized at the equator [Figure 3.9(a) and (b)]. For an equal mixture of even and odd M states in the initial ensemble, half of the ensemble can be oriented while another half of the ensemble remains unoriented and localized at the equator, Figure 3.9(c). The pulse also kicks the lobes of the state $|1'\rangle$ at the equator, but the acquired momentum is small compared to the momentum spread there: only small orientation of $|1'\rangle$ is created (Figure 3.9(c), thin line).

So far only the 2D rotor has been considered. However, the same scheme can

[2]The two-qubit notation in Equation (3.18) connects control of the wave-packet symmetries with quantum logic as outline in Section 3.2.3

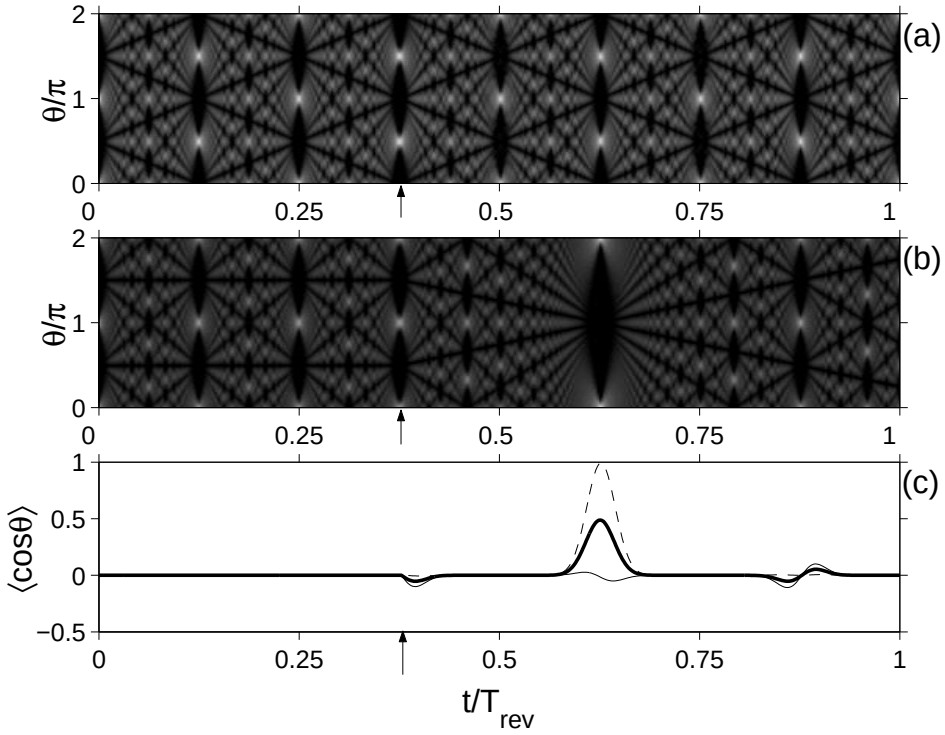

Figure 3.9: (a,b) Evolution of the states $|0'\rangle$ and $|1'\rangle$ in the control scenario discussed in the text. Brightness shows probability density. (c) Orientation of the state $|1'\rangle$ (dashed line), $|0'\rangle$ (thin line), and of their incoherent sum (thick line). Laser pulse is shown by the arrows.

be used in 3D, with minor adjustments. Firstly, in 3D $|right\rangle$ and $|left\rangle$ overlap due to axial symmetry, but the $\cos^2\theta$ potential does not act on them. Secondly, at $T_{rev}/8$ the linear term in the 3D spectrum $E(J) = J(J+1)$ shifts revived wave packets by $\pi/4$ from the poles and the equator. The control pulses are applied slightly before or after the exact revival, when the revived wave packets are at the pole and the equator.

Figure 3.10(a) demonstrates switching off and on rotational revivals for an ensemble of O_2 molecules with temperature $T = 50$ K. (Note that the θ used for these 3D simulations is again the polar angle used throughout the thesis, and no longer the 2D rotational angle used above in this section.) The initial alignment is created using a $\sin^2$ pulse with with peak intensity $I_0 = 1.5 \times 10^{14}$ W/cm^2 and FWHM duration of the pulse $\tau_{on} = 50$ fs. This pump pulse was chosen to match that used in recent experiments [31] where the peak intensity was set just below the ionization threshold to ensure strong alignment. The aligning pulse has its peak at t = 50 fs in the figure. The revivals are switched off and on by applying a weaker control pulse ($I_0 = 0.18 \times 10^{14}$ W/cm^2, $\tau_{on} = 50$ fs) at times 4.30 and 10.15 ps.

Figure 3.10(b) shows how a half-cycle pulse converts alignment of the OCS molecule ($B = 0.2039$ cm$^-$1, $\Delta\alpha = 4.1\mathring{A}^3$, $\mu = 0.709$ [79]) into orientation. The initial alignment is created using a pulse with $I_0 = 8.26 \times 10^{11}$ W/cm^2 and $\tau_{on} = 50$ fs. The half-cycle pulse used to create orientation $E(t) = E_0 \exp\left[-4 \ln 2 (t/\tau_{hc}^2)\right]$ has amplitude $E_0 = 8.11 \times 10^5$ V/cm and duration $\tau_{hc} = 500$ fs and was applied 20.536 ps after the aligning pulse.

Unlike other schemes of laser orientation of dipolar molecules [80] where the degree of orientation is determined by the strength of the half-cycle pulse, here the degree of orientation is determined by the *aligning* pulse. This aspect is similar to Ref. [81] which uses a strong laser field and a weaker DC field to orient a molecule. However, in [81] the strength of the interaction with the DC field μE must amount to kT to get strong orientation, while in the present scheme it is the strength of the aligning laser pulse alone that determines the degree of orientation. The half-cycle pulse simply cause interferences which converts the alignment into orientation.

This control scheme is not limited to rotors, but is applicable to any system with

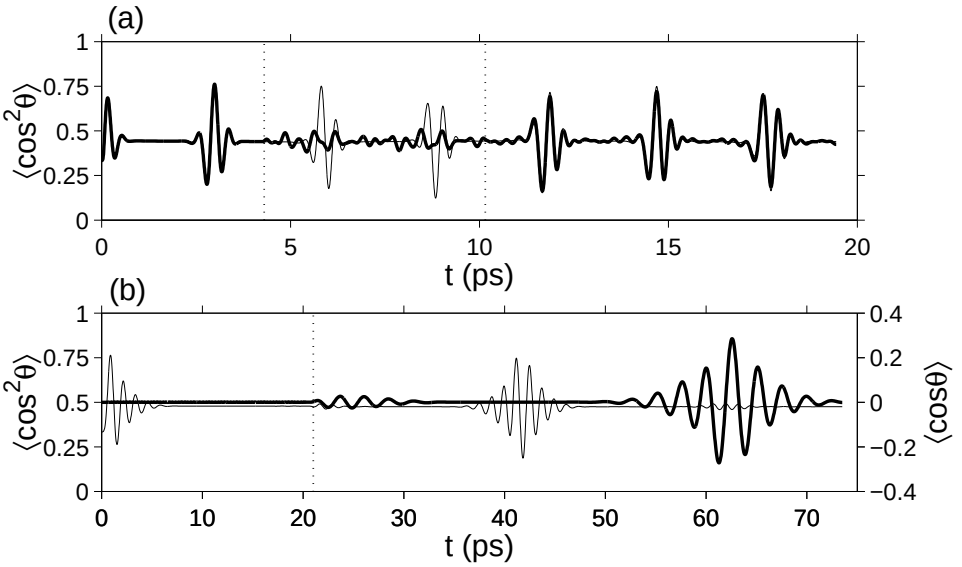

Figure 3.10: (a) Alignment of O_2 molecules at 50 K with (thick line) and without (thin line) the control pulses. (b) Alignment (thin line) and orientation (thick line) of OCS molecules at 10 K with the control pulse.

a quadratic spectrum, with or without the initial temperature, as long as the control interactions depend on the wave-packet position. A wave packet centred around n_0 in a system with a quadratic spectrum can be viewed as a carrier Ψ_{n_0} modulated by the envelope $f(\phi, t)$ [82], where the angle ϕ is the phase of the corresponding classical motion. The envelope spreads and revives exactly like a 2D rotor. As for the 2D rotor, the Floquet-like states track the symmetries of the envelope shifted by the linear motion.

This scheme also gives insight to controlling wave packets for thermal ensembles, when the system starts with an incoherent superposition of many initial eigenstates $n^{(i)}$. The initial laser pulse has to be strong enough to create similar wave packets $\Psi^{(i)}$ for every $n^{(i)}$. If the revival pattern of $\Psi^{(i)}$ is independent of its central state $n_0^{(i)}$ (determined by the initial state $n^{(i)}$), then the control pulses in this scheme would act in a similar way on all wave packets $\Psi^{(i)}$ and one needs only be concerned with the phase shifts of the wave-packet replicas, unrelated to kT.

Control of thermal ensembles is also possible when the revival dynamics for

different $n_0^{(i)}$ is not the same. This is the case with orientation. From the orientation perspective, incoherence of the initial distribution *is not removed* by the aligning pulse. In the envelope description, the wave packet with odd n_0 can be viewed as that with even n_0 (e.g. $n_{0\,even} = n_{0\,odd} - 1$), with an additional envelope modulation that turns the even n_0 into odd. An initially incoherent mixture of even and odd states is turned into a mixture of the the even ($|0'\rangle$) and the odd ($|1'\rangle$) envelopes for the aligned states. Different revival patterns for $|0'\rangle$ and $|1'\rangle$ allowed us to selectively affect only one of these states while leaving the other virtually unchanged, yielding an incoherent mixture of the oriented state and a state localized near the equator.

3.2.3 Quantum Logic Perspective

This control scheme of applying phase shifts at moments of fractional revivals can also be viewed from a quantum logic perspective [47]. Here, analogs of logical qubits are defined using wave-packet shape and symmetries. The control pulse acting at the fractional revivals are then view as gates implementing transformations between the qubits of the system. This view is outlined using wave packets of molecular vibrations.

Consider a wave packet $\Psi(t) = \sum_n C_n(t)\phi_n$, with amplitudes $C_n(t) \propto \exp(-iE_n t)$ distributed around a state $|n_0\rangle$ (E_n, ϕ_n are the energies and wave functions of the states). Just as with a superposition of optical waves, the wave packet can be described by a carrier and an envelope [82–85]. The carrier is given by the stationary wave function ϕ_{n_0} while the wave-packet envelope f is defined as:

$$f(t, \tilde{\theta}) \equiv \sum_n C_n(t) \exp[i(n - n_0)\tilde{\theta}] \tag{3.19}$$

It moves along the classical orbit associated with $|n_0\rangle$ and $\tilde{\theta}$ is the phase (angle) of that motion [82–85]. For an equidistant spectrum $E_n - E_{n_0} = \omega_0(n - n_0)$ the envelope is $f(t, \tilde{\theta}) = f(\tilde{\theta} - \omega_0 t) = f(\theta)$ and its shape is unchanged during the motion, which occurs with the period $T_0 = 2\pi/\omega_0$. Anharmonicity in the spectrum $E_n - E_{n_0} = \omega_0(n - n_0) + \Omega(n - n_0)^2$ leads to the wave-packet spreading and revivals:

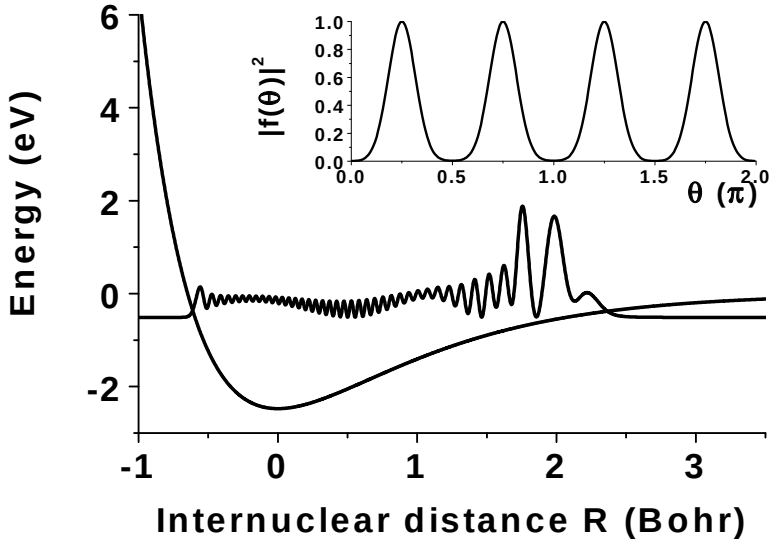

Figure 3.11: Wave packet ($|\Psi|^2$) made of $\sim$8 eigenstates in a Morse oscillator at $t = T_0/8 + T_{rev}/8$ and its envelope as the function of the classical angle θ (inset).

after time $T_{rev} = 2\pi/\Omega$ the wave packet re-localizes (revives) at its initial position. At the fractional revival time $T_{rev}/2M$ the wave packet splits into M *orthogonal* clones $F_i(\theta)$ spaced by $\Delta\theta = 2\pi/M$ [72].

Figure 3.11 is obtained by propagating the initial wave packet on the Cl_2-like potential modeled as a Morse oscillator $V(x) = D[1-e^{-ax}]^2 - D$ with $x = R - R_{eq}$, $D = 2.47$ eV, $a = 1.07$ a.u. The wave packet with reduced mass $m = 31270$ a.u. starts as Gaussian, $C_v(t=0) \propto e^{-(v-v_0)^2/\sigma^2}$, with $v_0 = 38$ and $\sigma = 4/\sqrt{\ln 2}$ (i.e. FWHM=8 levels). Near $v = 38$ the vibrational period is T_0 =130 fs and T_{rev} $\approx$8.31 ps. The fractional revival about $t = T_{rev}/8$ is immediately visible in the envelope representation [Equation (3.19) and Figure 3.11, inset], which removes carrier oscillations and brings out the underlying symmetries in the wave function.

The definition of wave packet 'bits' in terms of $f(\theta)$ is illustrated in Figure 3.12 for a two-bit system. These states are defined as four orthogonal superpositions of the 'basis' wave packets F_i obtained from the initial wave packet at the fractional revival time $T_{rev}/8$ (the four orthogonal clones in Figure 3.11, inset.) In general,

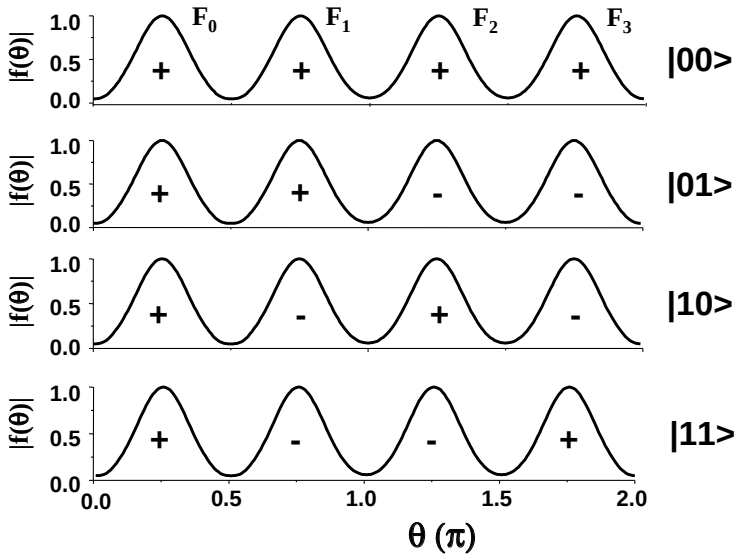

Figure 3.12: Four orthogonal basis states of the envelope function for the two-bit system. The signs give relative phases of the basis wave packets.

for K bits one divides $\tilde{\theta} = 0...2\pi$ in 2^K equal intervals. The states of the bits are determined by the *symmetry* of $f(\theta)$ with the resolution increasing in powers of 2. Reminiscent of the Fast Fourier transform, the lowest bit distinguishes between $f(\theta)$ even or odd on the whole orbit, the second bit distinguishes parity on every half of the orbit, the third would do it for every quarter, etc. For K-bit computation, structures finer than $2\pi/2^K$ in $f(\theta)$ are unresolved.

Thus, all basis wave packets in phase correspond to the ground state $|0...00\rangle$. A flip of the first (lowest) bit corresponds to multiplying $f(\theta)$ by $e^{i\pi} = -1$ on the second half of the phase orbit, $\theta = \pi...2\pi$. A flip of the second bit corresponds to multiplying $f(\theta)$ by $e^{i\pi}$ on the second and the fourth quarters of the orbit, thus doubling the modulation frequency. To flip the third bit one doubles the modulation frequency again, etc.

Each wave-packet bit distinguishes, on its own scale, not only between 'odd' and 'even', but also between 'left' and 'right'. As clear from Figure 3.12, the states $(|0\rangle + |1\rangle)/\sqrt{2}$ and $(|0\rangle - |1\rangle)/\sqrt{2}$ of the first bit correspond to the wave function

concentrated on the left side ($\theta < \pi$) or on the right side ($\theta > \pi$) of the whole orbit. The states $(|0\rangle + |1\rangle)/\sqrt{2}$ and $(|0\rangle - |1\rangle)/\sqrt{2}$ of the second bit describe the wave function concentrated on the left or the right sides of each half-orbit, the third bit would do the same for each quarter-orbit, and so on.

Analogs of single-bit and two-bit logical operations are now to be constructed. They are demonstrated for a two-bit system in a Morse oscillator. First considered are analogs of Rabi oscillation in a single qubit.

As seen from Figure 3.12, flipping the first bit requires changing the phases of two basis wave packets on the right side of the orbit by π. This operation flips the first bit independently of the state of the second bit, i.e. performs both $|00\rangle \Leftrightarrow |01\rangle$ and $|10\rangle \Leftrightarrow |11\rangle$ transitions. In general, for the j-th bit the phase orbit $\theta = 0..2\pi$ is divided into $J = 2^j$ equal parts, and on every second one of these parts the envelope $f(\theta)$ is multiplied by $\exp(i\phi)$. This procedure performs the operation

$$U_R = e^{i\phi/2} \begin{pmatrix} \cos\phi/2 & -i\sin\phi/2 \\ -i\sin\phi/2 & \cos\phi/2 \end{pmatrix} \tag{3.20}$$

on the j-th bit while all others are unaffected. Equation (3.20) can be derived by applying the above procedure to the $(|0\rangle \pm |1\rangle)/\sqrt{2}$ states of the $j-th$ bit: one is unaffected while the other acquires a global phase $\exp(i\phi)$. Up to the phase factor $e^{i\phi/2}$, U_R is equivalent to Rabi oscillation between the states $|0\rangle$ and $|1\rangle$ of the j-th qubit.

A phase shifter can be implemented by a local modification of the potential, i.e. by non-resonantly coupling it to another potential energy surface. This results in a position-dependent AC Stark shift, i.e., slightly shifts the potential near the turning point while the laser field is on. A wave packet moving through the turning point acquires extra phase $e^{i\Delta S}$ where ΔS is the change in the classical action. The non-resonant pulse must be timed within the window that the wave packet spends near the turning point. This restricts the number of basis wave packets that can be cleanly addressed, the number of qubits that can be encoded and, hence, the control over the wave-packet shape: a one-bit control does not resolve below a half-orbit,

two-bit control does not resolve below a quarter-orbit, etc.

Numerical simulations [Figure 3.13(a)] show how such phase shifter flips the first bit for the same initial wave packet and surface as in Figure 3.11 (see Figure 3.13 caption for the pulse parameters). The pulse non-resonantly couples the main surface near the inner turning point to an auxiliary surface also chosen as a Morse oscillator. Shifted down by the energy of one photon, the auxiliary surface is $V'(x) = D'(1 - \exp(-a'(x + \delta)))^2 - D' + \Delta E$ with $D' = 5.44$ eV, $\Delta E = 4.02$ eV, $\delta = 0.2$ and $a' = 1$ a.u. The electronic dipole matrix element is assumed R-independent. Figure 3.13(a) shows that the phase of the last two basis wave packets is flipped by π, as desired. Errors such as narrowing or widening of the basis wave packets are visible in Figure 3.13 but remain unresolved (until accumulated) by the two-bit description, which does not see below a quarter-orbit.

A phase shifter can be also used for multi-bit gates. For K bits, phase shifting of a single basis wave packet results in a K-bit operation. Figures 3.13(b) and (c) show the result of numerical simulation for the CNOT-type gate in the two-bit system. Applying the laser pulse for the quarter-period when the wave packet F_2 passes the turning point does not change the second bit if the first bit is in the state $(|0\rangle + |1\rangle)/\sqrt{2}$ ['left', Figure 3.13(b)], but flips the second bit if the first one is in $(|0\rangle - |1\rangle)/\sqrt{2}$ ['right', Figure 3.13(c)].

Changing the phases of basis wave packets is not sufficient – one also needs to change their relative amplitudes. This yields the ability to approximate arbitrary single-bit gate. For example, the Hadamard states of the first bit used in the previous example require merging half of the basis wave packets with their counterparts which are half-orbit away. To implement the Hadamard transform on the first bit the state $|00\rangle$ has to be transformed into $(|00\rangle + |01\rangle)/\sqrt{2}$ ('left'), the state $|01\rangle$ into $(|00\rangle - |01\rangle)/\sqrt{2}$ ('right'), and likewise for the states $|10\rangle$ and $|11\rangle$ – all using the same operation.

Wave-packet spreading and revivals give a natural way to accomplish this goal. Indeed, waiting for a fractional revival $T_{rev}/4$ and correcting phases one transfers a single basis wave packet into two packets on the opposite sides of the orbit with arbitrary relative phase. Similarly, four packets with arbitrary phases can be obtained

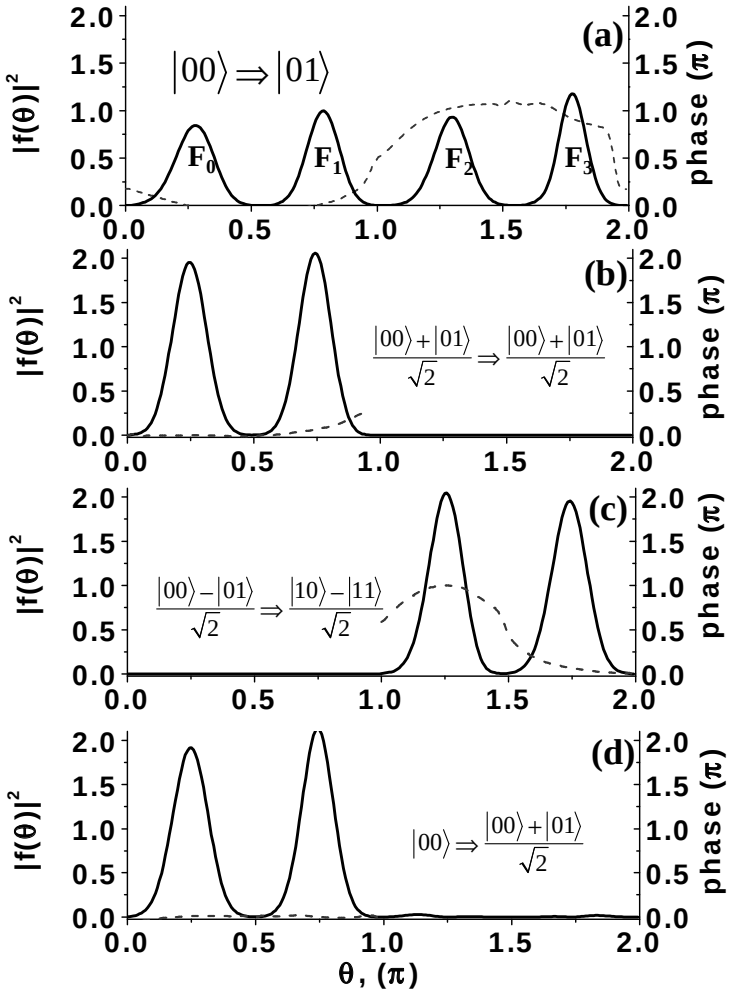

Figure 3.13: Numerical simulations of first bit flip (a), CNOT-type gate (b), (c), and Hadamard transform on the first bit (d). Transitions are labeled on the panels. Solid line: $|f(\theta)|^2$, dashed - phase of $f(\theta)$ Pulse envelope is $e^{-(t/\sigma_T)^8}$. (a) FWHM=$T_0/2$=65 fs with coupling $\mu E = 5.47 \times 10^{-3}$ a.u., (b) and (c) FWHM= $T_0/4$=32.5 fs and $\mu E = 6.04 \times 10^{-3}$ a.u., (d) FWHM=$T_0/2$=65 fs and $\mu E = 5.47 \times 10^{-3}/\sqrt{2}$ a.u.

from a single wave packet at $T_{rev}/8$, using the phase operation. Conversely, any four or two wave packets can be merged into one. This gives a guideline for implementing Hadamard transforms. Figure 3.13(d) shows a simulation of revival-based Hadamard transform $\hat{H}_1$ for the first bit, for the same model system as above. It is achieved by applying $\pi/2$ phase shift on the $\theta > \pi$ part of the orbit and waiting for $T_{rev}/4$. Hadamard transforms for higher bits are less trivial, but still possible. For example, Hadamard transform $\hat{H}_2$ for the second bit can be implemented as $\hat{H}_2 = \widehat{\Phi}_1^{\dagger}\ \widehat{(T_{rev}/8)}\ \widehat{\Phi}_3\ \widehat{(T_{rev}/4)}\ \widehat{\Phi}_2\ \widehat{(T_{rev}/8)}\ \widehat{\Phi}_1$ where $\hat{T}$ denotes free evolution over the time T and $\hat{\Phi}_m$ are diagonal 4x4 matrices with main diagonals as follows: $\widehat{\Phi}_1 : (e^{-i\pi/4}, 1, -e^{-i\pi/4}, 1)$, $\widehat{\Phi}_2 : (e^{i\pi/2}, 1, -1, 1)$, $\widehat{\Phi}_3 : (1, 1, 1, e^{i\pi/2})$.

As an example of possible control schemes, Figure 3.14 shows how the bit operations control the revival structure and evolution within vibrational period. The pulse parameters (see Figure 3.14) are well within the present-day technology. Panel (a) shows $\langle R(t)\rangle = \langle\Psi(t)|R|\Psi(t)\rangle$ of the same vibrational wave packet as used for Figures 3.11 and 3.13. Oscillations of the initially localized wave packet are damped by its spreading. Strong re-localization of the wave packet occurs near the half ($t = T_{rev}/2$) and the full revival.

The only difference between $\Psi(T_{rev}/4)$ and $\Psi(3T_{rev}/4)$ is that the first bit is flipped. Hence, flipping the first bit at $T_{rev}/4$ will bring the system to $3T_{rev}/4$. This is shown in Figure 3.14(b): the revival near $t = T_{rev}/2$ is now π out of phase compared to $t = T_{rev}/2$ but identical to $t = T_{rev}$ in Figure 3.14(a). Thus, the arrival of the revived wave packet to the turning point is shifted by half of the vibrational period $T_0/2$. Small oscillations of $\langle R\rangle$ immediately after the first bit-1 flip, are the result of small errors of the operation. However, these errors are removed by the second flip of the first bit at $t/T_{rev} = 3/4$.

The difference between $\Psi(T_{rev}/8)$ and $\Psi(7T_{rev}/8)$ is a $\pi/2$ rotation of the second bit. The control pulse in Figure 3.14(c) performs $\pi/2$ rotation of the bit 2 at t/T_{rev} = 1/8, 3/8, 5/8,... Now full revivals are accelerated to occur at every $T_{rev}/4$. The amplitude of subsequent revivals decreases: the errors add constructively. Here every $\pi/2$ rotation was implemented by adding a $\pi/2$ phase shift to packets 1 and 3. Alternatively, one can first apply a $\pi/2$-shift to packets 0 and 4 at $T_{rev}/8$ followed

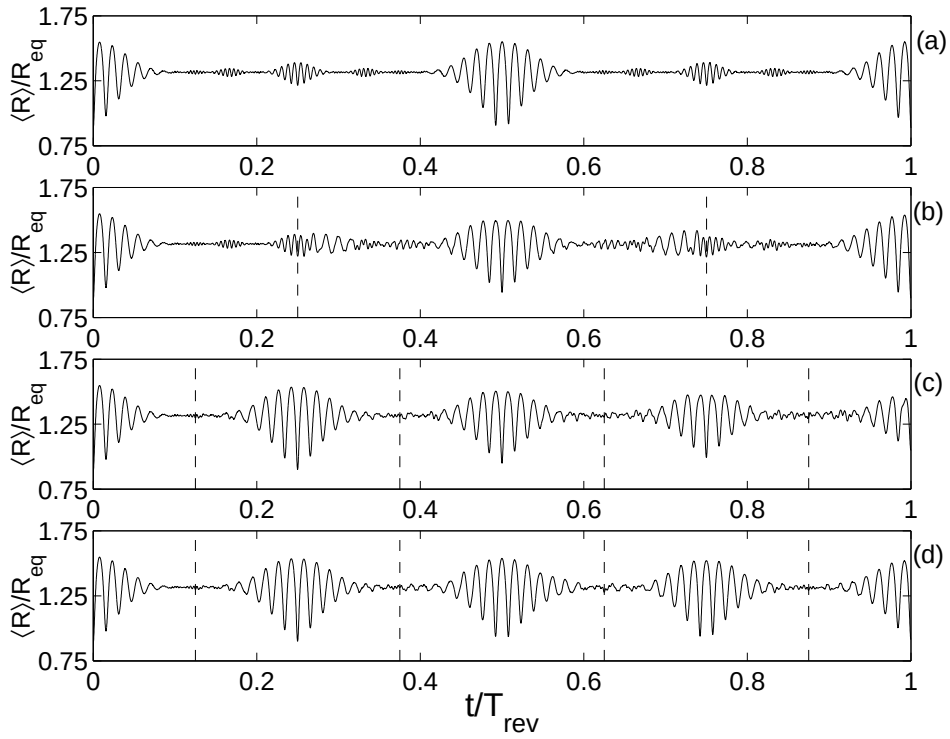

Figure 3.14: Control of wave-packet revivals by logical operations. Dashed lines show when short control pulses with envelope $e^{-(t/\sigma_T)^8}$ are applied. (a) - free evolution, (b) each operation uses FWHM=65 fs pulses with $\mu E = 5.47 \times 10^{-3}$ a.u., (c) each operation uses two FWHM=32.5 fs pulses with $\mu E = 6.04 \times 10^{-3}/\sqrt{2}$ a.u. applied to packets 2 and 4, (d) each operation uses two FWHM=32.5 fs pulses with $\mu E = 6.04 \times 10^{-3}/\sqrt{2}$ a.u. applied in alternating manner to packets 1,3 and 0,2

by a $\pi/2$-shift to packets 1 and 2 at $3T_{rev}/8$, etc (i.e., alternating $\pi/2$ and $-\pi/2$ rotation of the second bit), see Figure 3.14(d). Now the errors add destructively: the amplitude no longer decreases as in (c).

The multilevel analogs of quantum gates do not make a scalable quantum computer in a single wave packet. Adding one qubit requires doubling the number of states (or basis wave packets). Since the system is non-degenerate, the maximal frequency needed for control grows as $N\omega_0$. Still the above approach could be usefully applied for quantum information processing: it shows how one can use multilevel structure of many existing physical systems effectively, encoding several qubits in the quantum state of a single particle. Moreover, one does not have to worry about level-by-level addressability: as soon as free evolution commutes with the overall symmetry of the wave function, the symmetry can be used to encode quantum information. The wave-packet bits can be individually addressed, and a universal set of logical operations was constructed with only two physical operations – phase shift and free evolution – applied over a sequence of fixed time intervals T_0/N and $T_{rev}/2N$. Moreover, computational output can be measured in a bitwise manner with standard femtosecond techniques which naturally distinguish between 'left' and 'right' states of each bit: time-resolved fluorescence, ionization, or dissociation can tell whether the wave packet is on the right or the left half of the orbit, in the first or third vs the second or fourth quadrant, etc.

3.3 Quantum Control of Chaotic Kicked Rotors

The delta-kicked rotor has served as a paradigm for both classical and quantum chaos for many years. It is interesting, however, to note that although analogous (and beautiful) experiments in atom optics have been carried out (e.g. [86,87]), this long studied theoretical system has yet to be experimentally implemented with actual rotor systems, despite the long-time existence of a simple experiment proposal using polar molecules in a pulsed microwave field [88].

Recently, Gong and Brumer proposed a model for quantum control of chaotic diffusion in the delta-kicked rotor [48]. The authors then extended their model to the same experimental scenario of molecules in microwave fields mentioned above [49]. The initial superposition state considered in the Gong-Brumer model consisted of two rotational states.

The work presented in this section has two essential objectives. The first is to elucidate the physical mechanism behind the Gong-Brumer quantum control scenario. The second is to present an novel and experimentally feasible model of the kicked rotor system using polarizable linear molecules interacting with a strong laser through the AC Stark shift. In this model, the Gong-Brumer scenario can be extended to use wave packets of molecular alignment comprised of many field-free rotational states. Furthermore, the control scenario is shown to be temperature robust if using these aligned wave packets, which makes the experiment much simpler from the implementation point of view.

3.3.1 Kicked Rotor Dynamics

The classical Hamiltonian of the kicked rotor in a plane is given by

$$H = \frac{L^2}{2I} + A_0 \cos\theta \sum_j \delta(t/T - j) \tag{3.21}$$

where L is the angular momentum, I is the moment of inertia, A_0 is the kick strength, and T is the period of the kick. Hamilton's corresponding equations

of motion for the classical trajectories can be written in the form of a discrete mapping [50]

$$L_{n+1} = L_n + A_0 T \sin\theta_n \tag{3.22}$$

$$\theta_{n+1} = \theta_n + T L_{n+1}/I. \tag{3.23}$$

By defining the reduced momentum $l_n = TL_n/I$ and introducing $K = A_0 T^2/I$, the mapping becomes

$$l_{n+1} = l_n + K\sin(\theta_n + l_n/2) \tag{3.24a}$$

$$\theta_{n+1} = \theta_n + (l_{n+1} + l_n)/2 \tag{3.24b}$$

which is known as the *standard map*. Physically, the mapping as written above kicks the rotor in the middle of the interval T and is seen to depend only on the single parameter K. For values of $K >\approx 1$ the classical dynamics exhibits chaotic motion and unbounded diffusive energy growth [50].

The quantum equation of motion starts with the canonical quantization $L \rightarrow \widehat{L} = -i\hbar\partial/\partial\theta$ to give

$$\widehat{H} = -\frac{\hbar^2}{2I}\frac{\partial^2}{\partial\theta^2} + A_0\cos\theta\sum_j \delta(t/T - j). \tag{3.25}$$

Here as well an analytical solution for the one-period propagation can be found [50] and is given by the propagator

$$\widehat{U} = \exp\left[i\frac{\tau}{4}\frac{\partial^2}{\partial\theta^2}\right]\exp\left[-ik\cos\theta\right]\exp\left[i\frac{\tau}{4}\frac{\partial^2}{\partial\theta^2}\right] \tag{3.26}$$

where the parameters $\tau = \hbar T/I$ and $k = A_0/\hbar$ were introduced and the kick was again placed in the middle of the interval T. In the basis of field-free eigenstates

$\langle\theta|m\rangle = (1/\sqrt{2\pi})\exp[im\theta]$, $m = 0, \pm1, \pm2...$,

$$\begin{aligned}\langle m'|\widehat{U}|m\rangle &\equiv U_{m'm} \\ &= (-i)^{m'-m} e^{-i\frac{\tau}{4}(m'^2+m^2)} J_{m'-m}(k). \end{aligned} \tag{3.27}$$

where $J_m(x)$ are Bessel functions. Unlike the classical case, the quantum propagator has two independent parameters, τ and k. The product of these two parameters gives the classical K, while τ is the reduced Planck constant of the system. Note that in this notation the reduced momentum is $l = \tau m$.

3.3.2 Two-state Coherent Control

The recently proposed control [48, 49] considers an initial two-state quantum superposition with phase coherence, for example,

$$|\Psi_0\rangle = |2\rangle \pm |1\rangle. \tag{3.28}$$

The two quantum standard map parameters are chosen to be $\tau = 1$ and $k = 5$ which are typical of those used in the previous studies. The observable to be controlled is the average energy of the quantum system after n kicks

$$\langle E_n\rangle = \langle\Psi_n|\frac{1}{2}\widehat{l}^2|\Psi_n\rangle \tag{3.29}$$

The classical dynamics for initial classical distributions with sharp momentum of $l = 1$ and/or $l = 2$ show unbounded diffusive behaviour: the average classical energy

$$\widetilde{E}_n = \frac{1}{2J}\sum_{j=1}^{J}\left[l_n^{(j)}\right]^2, \tag{3.30}$$

where the sum over j implies a sum over the initial distribution, grows linearly within the number of kicks. In general for $K > 1$, $\widetilde{E}$ grows linearly according to the diffusion law $\widetilde{E} \simeq D(K)n$, where n is the number of kicks applied to the rotor and $D(K)$ is an oscillating but increasing function of K [89, 90]. Figure

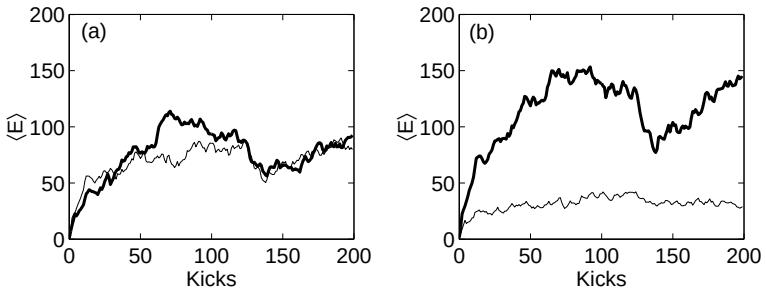

Figure 3.15: Quantum energy diffusion and localization: (a) Time evolution of the average energy $\langle E_n \rangle$ for the initial states $|2\rangle$ (thick) and $|1\rangle$ (thin). (b) Average energy for initial states $|2\rangle + |1\rangle \equiv |\Psi_+\rangle$ (thick) and $|2\rangle - |1\rangle \equiv |\Psi_-\rangle$ (thin).

3.15(a) shows the quantum energy diffusion for the two initial $|m\rangle$ propagated individually. Firstly, the quantum energy does not show unbounded growth but instead fluctuates around some mean energy of localization in the long time (or many kick) limit. Secondly, there are only minor differences between the evolution and localization of the $|2\rangle$ and $|1\rangle$ states. Figure 3.15(b) plots the average energy for $|\Psi_0\rangle = |2\rangle + |1\rangle \equiv |\Psi_+\rangle$ (thick line) and $|2\rangle - |1\rangle \equiv |\Psi_-\rangle$ (thin line). There is now a large difference in the long time energy localization when the phased superpositions $|2\rangle \pm |1\rangle$ are used, demonstrating the coherent control via initial phase coherence of the two eigenstates.

An interesting quantum-classical connection emerges if the control scenario is considered from a phase-space perspective. The classical Poincaré section for the chosen parameters was seen to exhibit predominantly chaotic dynamics spotted with small islands of stable dynamics. Figure 3.16(a) shows a Poincaré section of the system. The Poincaré section was constructed by dense sampling of the remaining islands of stability, which appear as solid areas, and sparse sampling of the chaotic region. The momenta of the quantum eigenstates involved are plotted as horizontal lines at $l = 1 = 0.318\pi$ and $l = 2 = 0.636\pi$. Note that the momentum of the eigenstates are seen to lie near to and cross one of the islands of stability.

A common estimate of the regions of classical phase-space which are relevant to the quantum dynamics is given by the Husimi distribution, which is a quantum analog of a classical phase-space distribution. The Husimi distribution $\mathcal{H}(\theta_0, l_0)$

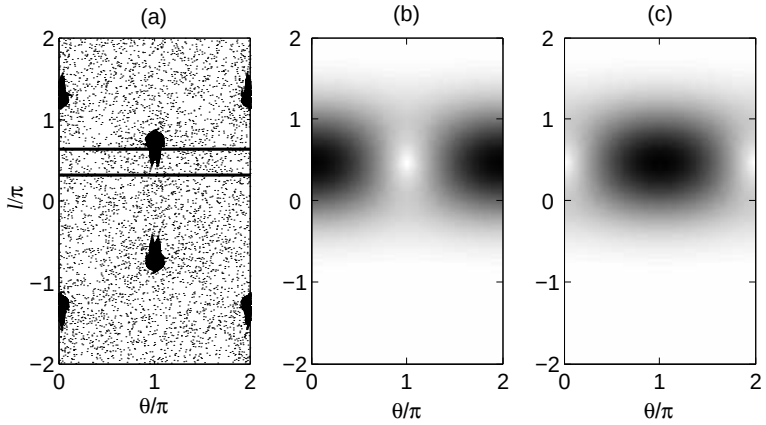

Figure 3.16: Comparison of the classical phase space with the quantum Husimi distributions. (a) Classical Poincaré section. (b) Husimi distribution for the state $|\Psi_+\rangle$ and (c) for the state $|\Psi_-\rangle$ [white is zero amplitude, black is large amplitude].

can be given as the amplitude of projection onto Gaussian wave packets

$$\mathcal{H}(\theta_0, l_0) = |\langle \theta_0, l_0 | \Psi \rangle| \tag{3.31}$$

where

$$|\theta_0, l_0\rangle \propto \exp[(\theta - \theta_0)^2 + i l_0(\theta - \theta_0)] \tag{3.32}$$

Figure 3.16(b) and (c) show the Husimi distributions for the two initial state $|\Psi_+\rangle$ and $|\Psi_-\rangle$ respectively. The interference caused by the phasing of the eigenstates is seen to effect the θ-localization. In the $|\Psi_+\rangle$ case, there is *destructive* interference of the phase-space in the region overlapping with the classical island of stability, while *constructive* interference is seen in this region for the $|\Psi_-\rangle$ superposition. Since the superposition which shows good overlap with the island of stability is also the superposition with localizes to the lower energy, these plots suggest that the suppression of energy absorption seen in the control scenario arises by trapping quantum population in classical islands of stability.

Further evidence for this interpretation is found by following the time-dependence of the wave function. Figures 3.17(a) and (b) plot intensity maps of the time-dependent probability in θ-space $|\Psi(\theta, t)|^2$ between the 150^{th} and the 200^{th} kicks.

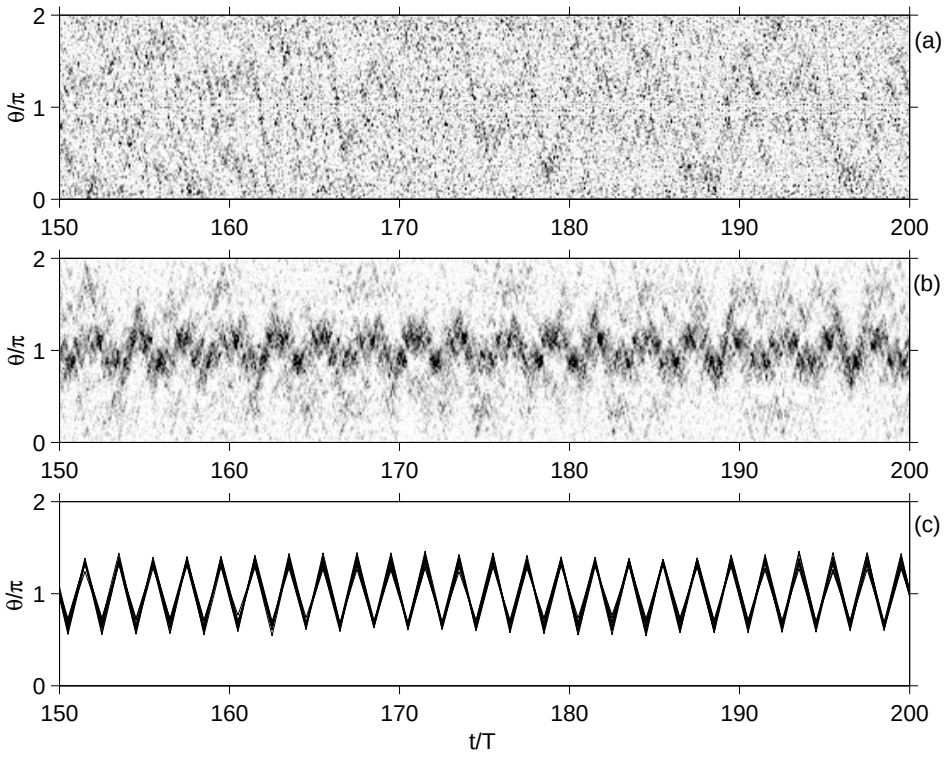

Figure 3.17: Quantum carpets during kicked rotor evolution which plots $|\Psi(\theta,t)|^2$ [white is zero amplitude, black is large amplitude]. (a) Evolution of the initial state $|\Psi_+\rangle = |2\rangle + |1\rangle$ and (b) of the state $|\Psi_-\rangle = |2\rangle - |1\rangle$. (c) Classical trajectories from the island of stability overlapped by the Husimi distribution for the initial $|\Psi_-\rangle$ state.

Panel (a) is for $|\Psi_+\rangle$ while panel (b) corresponds to $|\Psi_-\rangle$. The evolution of $|\Psi_+\rangle$ is seen to have an essentially random distribution over θ with time while that of $|\Psi_-\rangle$ shows localization around $\theta = \pi$. Panel (c) of the figure plots a few classical trajectories sampled from the overlapping island of stability. These classical trajectories exhibit qualitatively similar character as the pattern of θ-localization seen panel (b). These trajectories then play a strong role in the quantum dynamics and indeed one could say all of the control is a result of trapping a large portion of the quantum population in the classical island of stability.

One might note that the θ-localization seen in the quantum probability does not follow exactly the path of the classical trajectories. This is due in large part to the

choice of the reduced Planck constant: for smaller values of τ the quantum dynamics is more classical-like and the θ-localization more closely resembles the classical path. However, in the case of smaller τ (and hence more classical-like behaviour), the degree of control over the quantum localization of the energy diffusion becomes smaller and the θ-localization becomes less pronounced. Furthermore, the quantum dynamics for the chosen value of τ exhibit tunneling effects between the overlapped stability island and its mirror image at $(\theta, l) \approx (\pi, -0.7\pi)$. The classical trajectories for this mirror image island are identical to those of Figure 3.17(c) except for a time shift of T (i.e. when the trajectories started in the upper island are at $\theta = \pi + \Delta\theta$ those started in the lower island are at $\theta = \pi - \Delta\theta$.) The correspondence of the θ-localization with the classical paths from a single island is then distorted due to flow of population between these two classically isolated sets of stable trajectories.

As final evidence of the link between the character of the quantum dynamics and the islands of stability, it is shown that excitation of the higher energy island located at $(\theta, l) \approx (0, 1.3\pi)$ is possible based on the above developed ideas. Overlap with this region of phase-space can be achieved by choosing the two states $|5\rangle$ ($l = 1.59\pi$) and $|6\rangle$ ($l = 1.91\pi$) for the initial superposition. The Husimi distributions for $|\Psi_-\rangle = |5\rangle - |6\rangle$ and $|\Psi_+\rangle = |5\rangle + |6\rangle$ are as those for the states $|5\rangle - |6\rangle$ and $|5\rangle + |6\rangle$ respectively except they are now centered about $l = 1.75\pi$ as opposed to $l = 0.477\pi$ in the previous case. Inspection of the Poincaré section Figure 3.16(a) shows that now the superposition which gives high amplitude near $\theta = 0$ (i.e, $|5\rangle + |6\rangle$) will have the larger overlap with the relevant island of stability and hence it should be this superposition which shows strong θ-localization and lower asymptotic energy localization.

Figs.3.18(a) and (b) show the time-dependence of the probability $|\Psi(\theta, t)|^2$ for the $|5\rangle \pm |6\rangle$ states but this time panel (a) is for $|\Psi_-\rangle$ and panel (b) is for $|\Psi_+\rangle$. It is indeed the $|\Psi_+\rangle$ state which exhibits strong localization in θ-space. As this observed θ-localization suggests, it is also $|\Psi_+\rangle$ which localizes to the lower asymptotic average energy in this case.

The classical support for the θ-localization seen in Figure 3.18(b) is shown in Figure 3.18(c). These trajectories were sampled from the $(\theta, l) \approx (0, 1.3\pi)$ island

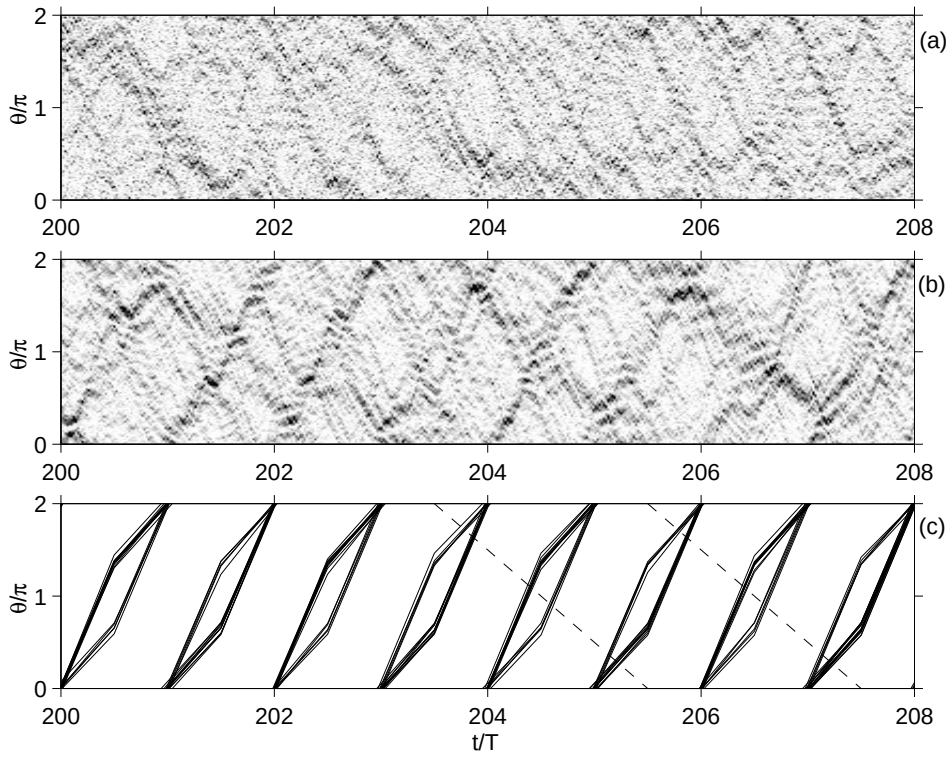

Figure 3.18: Quantum carpets during kicked rotor evolution which plots $|\Psi(\theta,t)|^2$ [white is zero amplitude, black is large amplitude]. (a) Evolution of the initial state $|\Psi_-\rangle = |5\rangle - |6\rangle$ and (b) of the state $|\Psi_+\rangle = |5\rangle + |6\rangle$. (c) Classical trajectories from the island of stability overlapped by the Husimi distribution for the initial $|\Psi_+\rangle$ state.

in question as well as from its tunneling partner located at $(\theta, l) \approx (0, 2.7\pi)$ with which the quantum dynamics shares population. Again the classical trajectories qualitatively mimic the θ-localization seen in the quantum dynamics.

Additional tracks of localized density in the $|\Psi_+(\theta,t)|^2$ plot can be seen. The dashed lines in Figure 3.18(c) show segments of *unstable* periodic classical trajectories which closely resemble these additional tracks suggesting that they are in fact scars, regions of increase density localized around isolated classical unstable periodic trajectories. Unlike the θ-localization around the islands of stable classical motion which can be clearly identified for all times in the region of energy localization, these scars were seen to appear and disappear as function of time. For

example, the scars are well resolved in the second half of the Figure 3.18(b) but seem to be smeared and distorted in the first half of the plot. It is quite interesting that the corresponding classical trajectory supporting the scar is nowhere near the initial Husimi distribution in phase-space. In fact, the classical support for the scar has *negative* momentum. This shows that, in addition to the effects of stable islands in the classical phase, scars can also play a role in trapping quantum population in the control scenario.

3.3.3 Control with Aligned Wave Packets

The preceding section showed that the coherent control proposed in the kicked rotor system can be related to small residual islands of stability in the classical phase space allowing for trapping of a large portion of the probability density at low angular momentum. The field-free dynamics of aligned rotational wave packets offers another method of control since the specific angular distribution, and hence overlap with the classical space, can be controlled simply by inducing a time delay between the creation of the rotational wave packet and the start of the chaos-inducing pulse train.

The kicks needed to model the kicked rotor system are applied to the molecular wave packet by a train of (ideally) delta-kick laser pulses interacting with the molecular rotor through the AC Stark shift

$$\widehat{H} = \frac{\widehat{J}^2}{2I} - A_0 \cos^2(\theta) \sum_n \delta(t/\tau_0 - n), \tag{3.33}$$

where $A_0 = \frac{1}{4}(\alpha_\parallel - \alpha_\perp)I_0$ is the effective kick strength for laser intensity I_0. In practice it is not possible to create ideal delta-kick pulses. However, as long as the pulse duration is much less than the rotational response of the molecule in question, the delta-kick picture is a good approximation.

The laser-included potential has a periodicity in θ double that of the kicked rotor studied above. However, the classical dynamics using the $\cos^2\theta$ potential for the kick can be reduced to the standard map with θ re-scaled by a factor of 2.

With the notation $\tau = \hbar\tau_0/I$, $k = A_0\tau_0/\hbar$, $\tilde{J} = 2J\tau/\hbar$, and $\tilde{\theta} = 2\theta$, the map can be written as

$$\begin{aligned} \tilde{J}_N &= \tilde{J}_{N-1} + (2k\tau)\sin(\tilde{\theta}_{N-1} + \tilde{J}_{N-1}/2) \\ \tilde{\theta}_N &= \tilde{\theta}_{N-1} + (\tilde{J}_N + \tilde{J}_{N-1})/2. \end{aligned} \tag{3.34}$$

For values of $2k\tau > 5$, the classical dynamics is predominantly chaotic and the average energy of any given ensemble simply grows linearly with the number of kicks. The diffusion rate of the energy in this regime depends only on the parameter $2k\tau$ and is independent of any particular initial phase space structure: the trajectories quickly diffuse and completely fill the energetically available phase space. In the simulations which follow, the parameters chosen give $2k\tau = 9.1$ and it was checked that the classical dynamics for this value of $2k\tau$ is independent of the degree of alignment in the initial classical phase-space distribution.

The model system considered is an initially aligned distribution of N_2 molecules subject to a pulse train with $\tau_0 = 1.21$ ps and $A_0 = 27.2$ meV. A delay between the moment of alignment and the start of the pulse train is used to induce phase shifts between the populated eigenstates using field-free evolution. The initial alignment of the molecules was created by the short-pulse method with a turn-on time of τ_{on} = 48.4 ps and a well depth of $U_0 = 54$ meV. The quantum dynamics governed by Equation (3.33) was calculated numerically.

Figure 3.19 shows the results for an initial rotational temperature of $T = 0$ K (i.e. only J = 0 in the initial distribution before the alignment pulse.) Plot (a) shows the average energy of the wave packet, $\bar{E} = \langle \widehat{J}^2/2I \rangle$, after 87 kicks as a function of the time delay between the turn off of the aligning field and the first kick in the pulse train. Recall that the effect of the time delay is to vary the relative phases of the eigenstates in the aligned superposition by field-free evolution. One can see that varying the phases by field-free evolution leads to quite strong enhancement or suppression (about a factor of 5) of the average energy of the system. Plot (b) shows the average energy of the system as a function of the number of kicks applied for the maximum and minimum cases of plot (a). This shows that by controlling

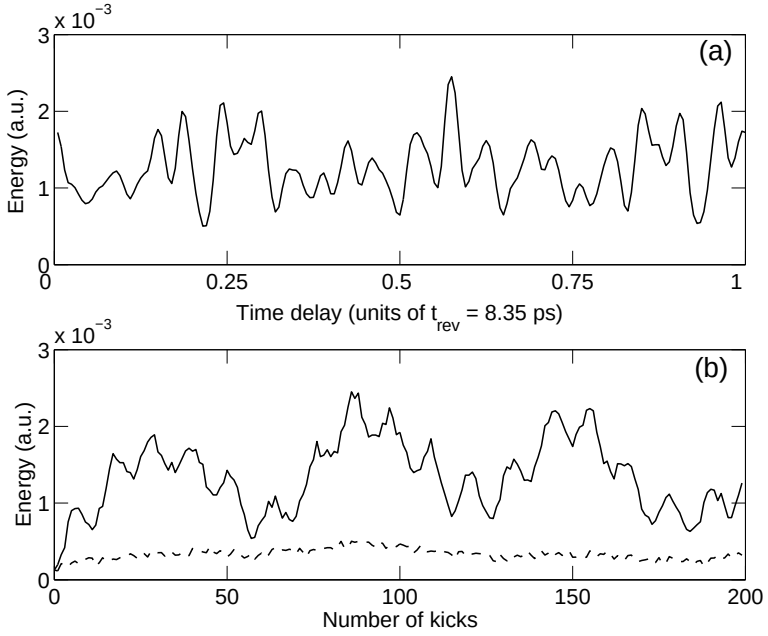

Figure 3.19: Degree of control over the chaotic diffusion for a rotationally cold ensemble ($T = 0$ K).

only the relative phases in the quantum superposition one can control the quantum localization of the classically chaotic system.

Figure 3.20 shows a similar calculation but now for an initial rotational temperature of $T = 50$ K. Plot (a) showing the energy as a function of the turn-off/pulse train time delay was taken after 38 kicks. There remain fringes in the average energy as a function of time delay but the contrast is less than in the $T = 0$ K case, the variation is $\sim$35% of the maximum energy for number of kicks greater than $\sim$100. When the calculations were again repeated for $T = 100$ K (not shown), the fringes were reduced to $\sim$20% of the maximum energy.

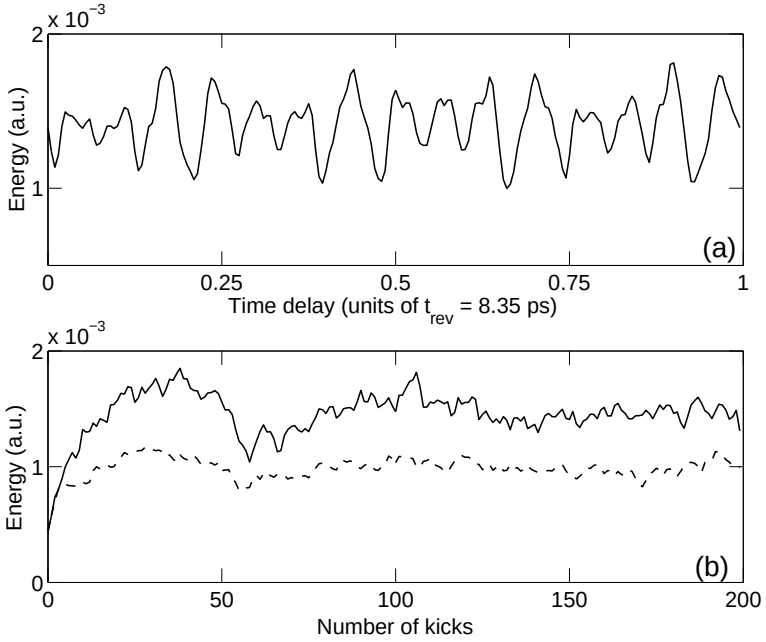

Figure 3.20: Degree of control over the chaotic diffusion for a rotational temperature of $T = 50$ K.

Chapter 4

Applications of Molecular Alignment

4.1 Pulse Compression

Molecular phase modulation opens the route to pulse compression to the single-cycle regime in the visible and near-UV [32, 91–97]. In this approach, a laser pulse or pulses induce vibrational or rotational excitation of molecules. Interaction with the resulting time-dependent modulation of the refractive index is used for compression.

Two opposite limits of this scheme have been studied experimentally. In the first limit [91, 92], molecules interact with two concurrent long pulses. Careful tuning of pulse frequencies at the medium input above the Raman resonance results in a train of compressed ∼2fs pulses at the output. In the second limit [93–96], the input pump pulse is short compared to the response time (vibrational or rotational) of the molecules. This ensures uniform excitation of the medium as seen by a delayed probe pulse which is then compressed to a single short pulse. In this limit the medium excitation is relatively weak, limiting the rate at which new bandwidth is generated.

Considered here is an intermediate excitation regime, combining strong molecular excitation characteristic for the first limit with the compression of a single

pulse characteristic for the second limit. Similar to [93–97], the pump-probe approach is used, but the pump duration is increased beyond the impulsive regime to increase the molecular excitation and the rate at which the new bandwidth is generated. This shortens the required propagation length, and hence lessens the effects of medium dispersion which become detrimental for large bandwidth. The pump pulse is now long enough to be modified by the Raman response during propagation, leading to non-uniform excitation across the propagation length. By optimizing the duration and intensity of the input pulse, (i) the molecular excitation is in turn optimized (a combination of alignment strength and duration), (ii) the non-uniformity of the excitation across the fiber as the pump is modified during the propagation is minimized, (iii) the propagation length is shortened to minimize effects of dispersion, and (iv) effects of ionization due to the strong pump pulse are ensured to be negligible.

The pump-probe approach decouples the medium response from the details of the probe pulse being compressed. The probe can then be pre-shaped *at the input* [32] (when its bandwidth is still narrow and can be handled by standard techniques [53, 54]) to pre-compensate for dispersion in the Raman medium and optical elements after the fiber.

From a theoretical standpoint, the intermediate regime requires the solution of the time-dependent Schroedinger equation for the Raman response of the medium concurrent with the Maxwell equation for the pump. The non-perturbative Raman response, electronic Kerr effect, linear dispersion in the molecular medium and the effect of the free electrons created by the pump are included in the propagation as well as self-steepening and pump/probe walk-off. Input probe pulses at both 800 nm and 400 nm are considered.

4.1.1 Pump Pulse Propagation

The Maxwell equation for the strong pump pulse propagating in the hollow core fiber can be written, in atomic units, as

$$\frac{\partial E_s}{\partial x} + \frac{1}{c}\frac{\partial E_s}{\partial t} = -\frac{2\pi}{c}\frac{\partial P_s}{\partial t}. \tag{4.1}$$

This equation does not assume the slowly varying envelope approximation, but instead includes the reflected waves to first order only [98].

The polarization P_s is given by

$$P_s = P_\theta + P_K + P_{f.e.} \tag{4.2}$$

where P_θ, P_K, and $P_{f.e.}$ are due to molecular orientation, the electronic Kerr response, and the free electrons respectively. P_θ is [32]

$$P_\theta = N[\alpha_\perp(\omega) + \Delta\alpha(\omega)\langle\cos^2\theta\rangle(x,t)]E_s(\omega) \tag{4.3}$$

where N is the molecular number density, $\alpha_\perp(\omega)$ and $\alpha_\parallel(\omega)$ are the perpendicular and parallel polarizabilities of the molecule, and $\Delta\alpha(\omega) = \alpha_\parallel(\omega) - \alpha_\perp(\omega)$. The polarizabilities are normalized to their static values, $\alpha_{\perp,\parallel}(\omega) = \alpha^{(0)}_{\perp,\parallel} f_{\perp,\parallel}(\omega)$ with the functions $f_{\perp,\parallel}(\omega)$ given by $f_\perp(\omega) \approx f_\parallel(\omega) \approx f(\omega)$ with $f(\omega)$ taken from Ref. [99]. The average alignment $\langle\cos^2\theta\rangle$ is calculated by solving the Schrödinger equation [32]

$$i\frac{\partial}{\partial t}\Psi(\theta,x,t) = \left[\frac{\widehat{J}^2}{2I} - \frac{\Delta\alpha|E_s|^2(x,t)}{4}\cos^2\theta\right]\Psi(\theta,x,t) \tag{4.4}$$

and averaging $\cos^2\theta$ over both the wave packet and an initial Boltzmann distribution for a given temperature. The electronic Kerr response is $P_K = \chi^{(3)}(N)|E_s|^2$ where $\chi^{(3)}(N)$ is the third-order susceptibility of the medium (see e.g. Ref. [61]). The free electron contribution is

$$P_{f.e.} = -N[W(x,t)/\omega^2]E_s(\omega) \tag{4.5}$$

where $W(x,t)$ is the ionization probability calculated using [100].

From a computational perspective, Equation (4.1) is solved by first going to the moving frame $\tau = t - x/v_s$ where v_s is about the speed at which the pump pulse propagates. The wave equation then becomes

$$\frac{\partial E_s}{\partial x} = -\frac{2\pi}{c}\frac{\partial P_s}{\partial \tau} - \left[\frac{1}{c} - \frac{1}{v_s}\right]\frac{\partial E_s}{\partial \tau} \equiv \widehat{\mathcal{L}} E_s. \tag{4.6}$$

The pump pulse is specified for all time at the input of the hollow core fiber ($x = 0$), and then is propagated through the fiber by standard finite difference methods

$$E_s\big|_{x+1}^{t} = E_s\big|_{x-1}^{t} + 2\Delta_x \widehat{\mathcal{L}} E_s\big|_{x}^{t} \tag{4.7}$$

where Δ_x is the step size in the x direction. P_θ and $P_{f.e.}$ are handled by writing them as

$$P_\theta = N[\alpha_\perp^{(0)} + \Delta\alpha^{(0)}\langle\cos^2\theta\rangle(x,\tau)]\widehat{\mathrm{FT}}\{f(w)E_s(\omega)\} \tag{4.8}$$

and

$$P_{f.e.} = -NW(x,\tau)\widehat{\mathrm{FT}}\{[1/\omega^2]E_s(\omega)\}. \tag{4.9}$$

where $\widehat{\mathrm{FT}}$ means Fourier transform. These forms of P_θ and $P_{f.e.}$ assume that $\langle\cos^2\theta\rangle$ and W vary negligibly over one period of the laser cycle for the frequencies involved. The needed time derivatives in $\widehat{\mathcal{L}}$ are calculated again by finite difference methods $\partial F/\partial\tau = [F^{t+1} - F^{t-1}]/2\Delta_\tau$ where $F = E_s$, P_θ, P_{NL}, or $P_{f.e.}$ as needed and Δ_τ is the step size in time.

The pump pulse at the input was $E_s(x=0) = \mathcal{E}_s \exp[-(\tau/\sigma_\tau)^2 - i\omega_s\tau]$ with ω_s corresponding to 800 nm. The molecular medium, N_2, was at 90 K and density of 10^{20} cm^{-3}. To optimize the pump, the pump intensity is first fixed to obtain about 0.1% ionization at the end of the pulse and the pulse duration was varied. The maximum of the resulting field free alignment as a function of pulse duration is shown in Figure 4.1, with strongest alignment for $\sigma_\tau^{(0)} \approx 105$ fs. For the propagation, pulse durations somewhat less than $\sigma_\tau^{(0)}$ were started with as a first guess since the pump stretches during the propagation. Propagating the pump through the full length of the fiber (15 cm), the intensity and duration of the pump is then adjusted

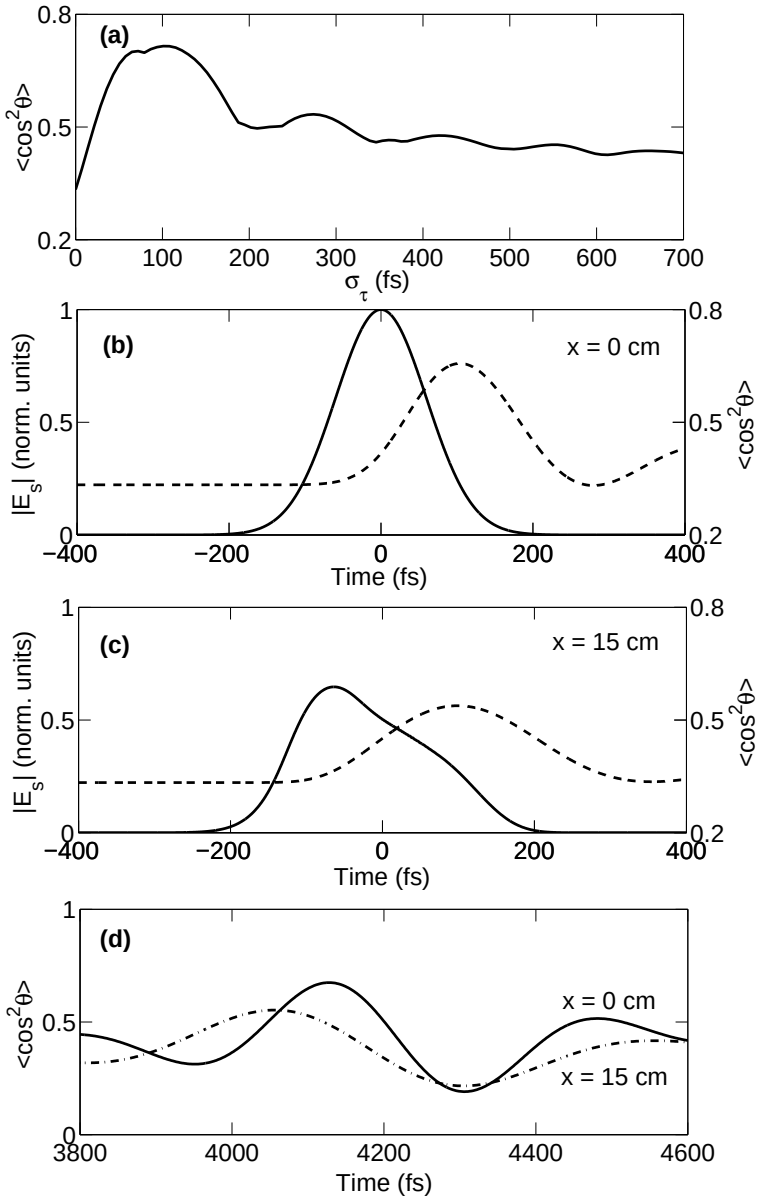

Figure 4.1: Propagation of the optimized pump pulse, $\sigma_\tau = 60$ fs, for intensity 6.5×10^{13} W/cm^2. (a) Alignment at the input of the fiber vs pump duration for 8×10^{13} W/cm^2 (b) Pump pulse (solid) and alignment (dashed) at the input of the fiber for $\sigma_\tau = 60$ fs vs time. (c) Same at the fiber output. (d) Alignment recurrence at the input and output of the fiber used to compress the probe

until desirable alignment (combination of alignment strength and duration) across the full length of the fiber was achieved. Figs.4.1(b) and (c) show the pump pulse at both the input ($x = 0$ cm) and the output of the fiber ($x = 15$ cm) along with the alignment $\langle \cos^2 \theta \rangle (t)$.

As the pump propagates through the medium, the alignment induced by the pump causes it to see a higher index of refraction on the trailing end. This results in a modification of the pump across the medium. The strong pump also undergoes small but noticeable self-phase modulation due to the $\chi^{(3)}$ term. Ionization by the pump was low, so that the free electron dispersion caused only small perturbations to the propagation. The resulting recurrence in the molecular alignment to be used to modulate the weak probe pulse is shown in Figure 4.1(d) at both the input and the output of the fiber. Although the recurrence structure also changes across the medium due to the modification of the pump, the modulation depth and structure is still adequate to compress the probe pulse.

4.1.2 Compression of Probe Pulse

The weak probe E_w is propagated using the same Equation (4.1) with polarization P_w due to molecular alignment and free electrons:

$$\begin{aligned} P_w &= P_\theta + P_{f.e.} \\ P_\theta &= N[\alpha_\perp(\omega) + \Delta\alpha(\omega)\langle \cos^2 \theta \rangle (x, \tau - \tau_d)] E_w(\omega) \\ P_{f.e.} &= -N[W(x)/\omega^2] E_w(\omega) \end{aligned} \tag{4.10}$$

Now $\langle \cos^2 \theta \rangle$ is a known function calculated during the propagation of the pump. The pump-probe delay τ_d is an optimization parameter and $W(x)$ is the ionization probability at the end of the pump pulse throughout the medium. The intensity of the probe is limited by requiring negligible nonlinear effects as it compresses in the glass, as well as negligible modification of the prepared rotational response in the fiber.

A part of the compression scheme is a 0.2 mm CaF_2 window after the fiber.

The optimal probe at the input of the fiber was found by propagating a 1 fs target pulse backward through first the CaF_2 window (using a Sellmeier-type formula) and then the fiber. Both the fiber length and the time delay τ_d were varied until the minimum bandwidth pulse was obtained at the fiber input. Typical τ_d correspond to ∼4200 fs in Figure 4.1(d).

This optimization process yields an input spectrum with narrow FWHM but broad wings [32]. Since it could be difficult to experimentally shape these wings, it is demanded in the optimization that they be absent in the input probe. Thus, a masking function is applied to the optimal input spectrum obtained by the backward propagation. The truncated input probe was then propagated forward through the fiber and the CaF_2 window to obtain the compressed output pulse.

The 800 nm probe (Figure 4.2) was optimized with a propagation length of 15 cm, limited by medium dispersion, while the 400 nm probe (Figure 4.3) used 6.5 cm (phase modulation rate $\omega(dn/dt)$ scales with ω.) Plots (a) show the probe pulses along with the instantaneous frequency at the input after the wings in the spectra of the optimal solutions were truncated. With the pulses written as $E(\tau) = |E(\tau)| \exp[-i\phi(\tau)]$, where $|E(\tau)|$ is real, the instantaneous frequency is defined as $\omega(\tau) \equiv d\phi(\tau)/d\tau$. The thick lines in plots (b) show the corresponding input spectra. For the 800 nm probe, the input bandwidth corresponding to a 5 fs pulse was allowed. For the 400 nm probe, the allowed bandwidth corresponded to 10 fs pulse. Although not shown on the plots, the phase of input spectrum already varied less than $\pi/2$ from one pixel to the next when discretized into only 128 pixels.

Plots (c) and (d) show these probe pulses and their spectra after the fiber and the CaF_2 window. The 800 nm probe has compressed to FWHM = 1.2 fs and the 400 nm probe has compressed to FWHM = 1.4 fs. To characterize the wings of a pulse, the *effective full width* EFM = $\sqrt{8 \ln 2 \langle (t - \langle t \rangle)^2 \rangle}$ is used (for a Gaussian pulse EFW = FWHM, for a sech(t/σ) pulse EFW = 1.4 FWHM). The EFW measures for the two compressed pulses shown above are 2.7 fs for the 800 nm probe and 3.8 fs for the 400 nm probe. If only 10 fs bandwidth is allowed for 800 nm probe, the optimized results are FWHM=1.7 fs and EFW=2.4 fs.

The thin lines in Figures 4.2(c) and refFig400nm(c) show alternate optimized

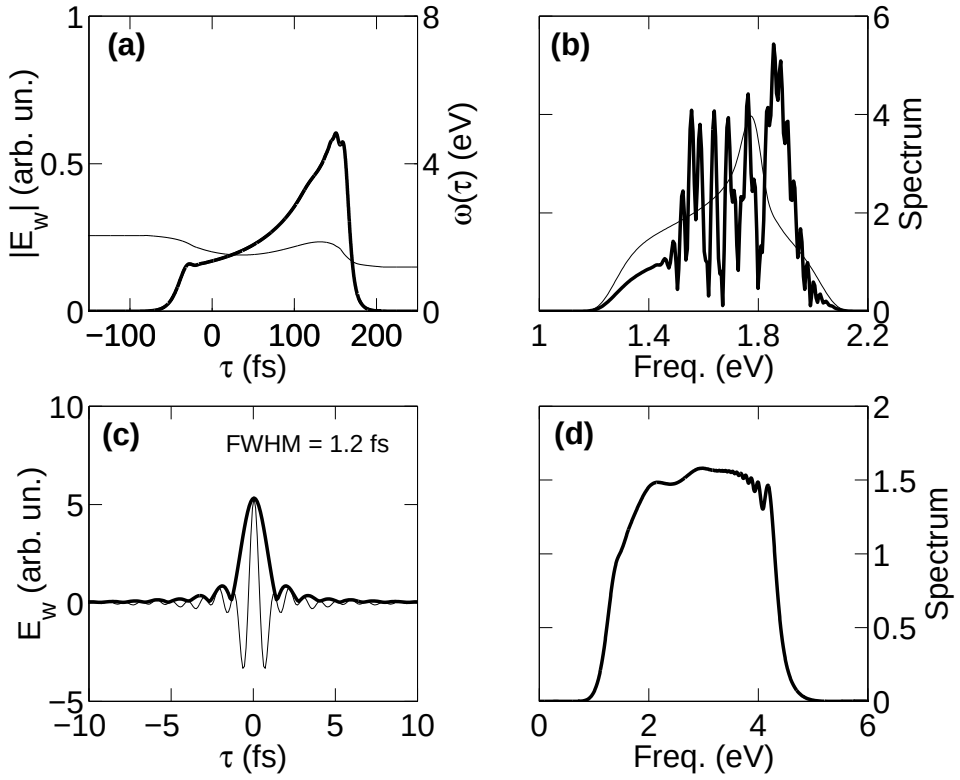

Figure 4.2: Compression of 800 nm probe pulse. (a) The amplitude (thick) and instantaneous frequency (thin) of the probe at the fiber input. (b)Optimized spectrum (thick) of the probe in (a) and the spectrum of an alternate probe (thin, see text) at the fiber input. (c) Compressed probe (envelope-thick, field-thin) and (d) spectrum after propagation through the medium and through the CaF_2 window.

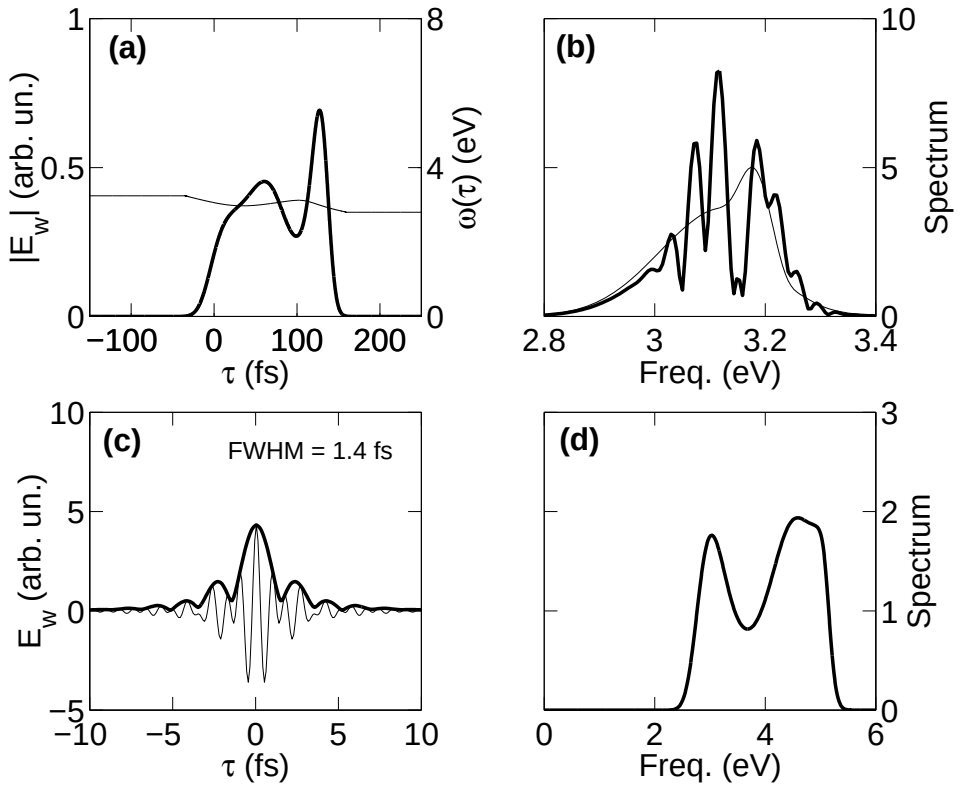

Figure 4.3: As Figure 4.2 but for probe optimized for 400 nm at the input of the fiber.

pulses where the additional criterion of a smooth input spectrum was enforced. Using these alternate input pulses, the 800 nm probe was compressed to FWHM = 1.5 fs (EFW = 2.5 fs) with a propagation length of 10 cm, and the 400 nm probe was compressed to FWHM = 2.1 fs (EFW = 3.0 fs) with a propagation length of 5.25 cm.

4.2 Laser-Induced Electron Diffraction

4.2.1 Diffraction in a Strong Laser Field

Intense laser pulses can generate a diffraction image of a molecule using the molecule's own electrons [101–103], with sub-Å spatial and nearly 1 fs temporal resolution. After strong-field ionization, the electron wave packet is first pulled away from the ion by the electric field of the laser. Within the same laser cycle, the electric field reverses its direction and the electron can be driven back to re-collide with the parent ion. Elastic scattering takes the diffraction image of the parent molecule (Figure 4.4) [102].

From the ion's perspective, during the recollision the electron current density exceeds 10^{10} A/cm^2 and is concentrated within a small fraction of the laser cycle ($<$ 1fs) [103], exceeding these characteristics in conventional approaches to ultrafast electron diffraction (see e.g. [60]) by many orders of magnitude. The energy W of the returning electron reaches $3.17U_p$ [104], where $U_p = E^2/4\omega^2$ is the average electron oscillation energy and E, ω are the field amplitude and frequency (atomic unites are used everywhere). For the Ti:Sapph laser $W \approx 133$ eV at the intensity $I \approx 7 \times 10^{14}$ W/cm^2 and can be increased as λ^2 by increasing the wavelength λ, yielding sub-Å spatial resolution. A laser pulse can also be used to align [105] molecules, emphasizing the diffraction pattern.

These advantages do not come for free: the nature of the electron pulse and the presence of the strong laser field lead to several complexities. These complexities are identified and analyzed numerically and analytically. Procedures for recovering the undistorted diffraction image are described. The main ingredients in the recipe are: (i) tunnel ionization regime, (ii) special cuts in the photo-electron spectra, (iii) the use of nearly single-cycle pulses $E(t)\cos(\omega t + \varphi)$ with stabilized carrier-envelope phase φ. Ref. [106] describes 3-dimensional *ab initio* numerical simulations which demonstrate how the internuclear distance for diatomics can be identified in multiphoton regime. This work suggests a general recipe for obtaining the overall diffraction image.

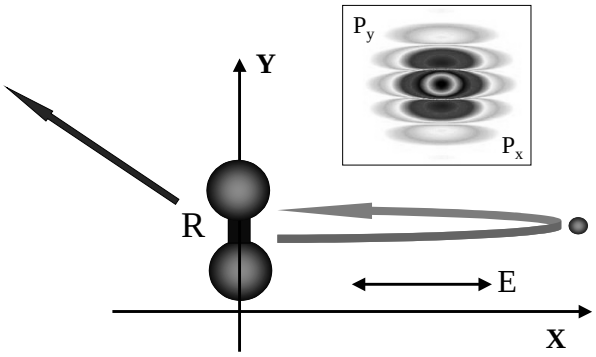

Figure 4.4: Diffraction during strong-field ionization. Inset sketches ground state in the velocity space, with shades of gray coding the probability.

An example of a diatomic molecule aligned perpendicular to the field $E\cos\omega t$ polarized along the x axis is used, see Figure 4.4. Numerically, the same H_2^+-like 2D model as in [102] is used with the soft-Coulomb electronic potential ($a = 0.5$ a.u.)

$$\begin{aligned} V_M(x,y|R) &= V_A(x,y-R/2) + V_A(x,y+R/2) = \\ &= -\frac{1}{\sqrt{x^2+\left(y-\frac{R}{2}\right)^2+a^2}} - \frac{1}{\sqrt{x^2+\left(y+\frac{R}{2}\right)^2+a^2}} \end{aligned} \tag{4.11}$$

The internuclear distance is frozen at $R = 4$ a.u. ($I_p = 0.96$ a.u.). Reading the re-collision induced diffraction image forces one to deal with several unavoidable complexities outlined below.

(1) Imprint of the initial state during tunneling. Consider the limit of tunnel ionization $\gamma^2 = I_p/2U_p \ll 1$, where I_p is the ionization potential. For each moment of ionization t_0, the newly created electronic wave packet in the continuum

$\Delta\Psi(\mathbf{v}_\perp, t_0)$ depends on the transverse velocity $\mathbf{v}_\perp$ as (see e.g. [18]):

$$\Delta\Psi(\mathbf{v}_\perp, t_0) \propto \langle \mathbf{v}_\perp | \Psi_i \rangle e^{-\frac{v_\perp^2}{2}\tau_T(t_0)} \tag{4.12}$$

Here $\tau_T(t_0)$ is the tunneling time, $\omega\tau_T(t_0)\cos\omega t_0 = \gamma$. The Gaussian shape due to tunneling filters the Fourier-transform $\langle \mathbf{v}_\perp | \Psi_i \rangle$ of the initial orbital Ψ_i which already carries the imprint of the orbital's structure (Figure 4.4, inset). This distorts the shape of the ionizing wave packet. The laser parameters are chosen to minimize such distortions.

(2) Holographic-type structures. The nonzero width of the Gaussian velocity distribution $\Delta v \sim 1/\sqrt{\tau_T}$ Equation (4.12) gives rise to a holographic-type interference in the final electron spectrum. For example, the deflection of the electron recolliding with the velocity $\mathbf{v} \parallel \mathbf{x}$ creates transverse component $v_\perp$ after the scattering. If $v_\perp$ is within the Δv, the scattered wave will interfere with the reference wave that has started with nonzero $v_\perp$ and has missed the ion. Similar interference occurs for an atom.

(3) Large scattering angles. For typical recollision energies ~ 100 eV, deflection with relevant transverse velocities $v_\perp \sim \pi/R$ corresponds to large scattering angles θ. Quickly decreasing cross sections $d\sigma(\theta)$ distort the diffraction image.

(4) Distortions induced by the laser field. After the scattering, the electron's longitudinal velocity is changed by the laser field while the transverse velocity remains unaffected. Therefore, for a given recollision energy, the electron's final energy after the 'elastic' scattering depends on the deflection angle. The angle-resolved spectrum for a fixed final energy *does not* correspond to the diffraction pattern for a given recollision energy.

(5) Interference between diffraction images taken at different energies. The recollision energy ranges from 0 to $\sim 3.2U_p$ [104]. In the absence of the laser field energy-resolved spectra would discriminate between the diffraction images taken at different energies. However, in the presence of a laser field, electrons re-colliding with different energies at different times t may end up with the same final velocity vector $\mathbf{v}$. The resulting interference is caused exclusively by the laser field.

4.2.2 Recovering the Diffraction Image

The first step in recovering the diffraction pattern is to account for the laser-induced change in the electron energy after the scattering. In the strong low-frequency field, large electron oscillation amplitude $\alpha = E/\omega^2$ ($\alpha \approx 40$ a.u. at $I \approx 7 \times 10^{14}$ W/cm^2 and $\lambda = 800$ nm) separates the recollision into three stages: (i) electron approach with the velocity v, (ii) fast recollision during an interval $\Delta t \sim R/v$ much shorter than the laser cycle (in a quarter-cycle the electron covers the distance $\alpha \gg R$), (iii) free oscillation in the laser field after the recollision. Since $\omega\Delta t \ll 1$, scattering occurs at a well-defined phase $\phi = \omega t$ and velocity $v(t)$. Without the laser field, the elastic scattering means $v_x^2 + v_y^2 = v^2$ where v is the incoming velocity and v_x, v_y are the parallel and perpendicular velocities after the scattering. The laser-induced oscillation changes this to

$$(v_x - v_0 \sin\omega t)^2 + v_y^2 = v^2(t); \qquad v_0 = E/\omega \tag{4.13}$$

where v_x, v_y are the *final* velocities at the detector and $v(t)$ is the incoming velocity (along x-axis). Equation (4.13) assumes a fast collision and means that the diffraction image taken at a given energy $v(t)^2/2$ lies on the circular cut through the electron spectrum with the radius $v(t)$ and the origin shifted by $v_0 \sin\omega t$. Each time of recollision defines its own circle (both the radius and the shift); the overall spectrum is their superposition.

A simple recollision model [104] assumes that after tunneling at t_0 the trajectory starts near the origin with negligible velocity. In this model $v(t) = v_0(\sin\omega t_0 - \sin\omega t)$ and the time of ionization t_0 corresponding to t is given by

$$\omega(t - t_0)\sin\omega t_0 + (\cos\omega t - \cos\omega t_0) = 0 \tag{4.14}$$

Equation (4.14) means that at t the electron returns to its initial position at t_0. However, after tunneling the electron appears at some distance $x(t_0)$ from the origin. For a given recollision moment t, this changes the recollision energy. In the tunneling limit the correction is [107] $v^2(t)/2 \Rightarrow v^2(t)/2 - I_p dt_0/dt$ where $t_0(t)$

is still defined by Equation (4.14). The cut in the electron spectrum for a given recollision energy from Equation (4.13) becomes

$$(v_x - v_0 \sin\omega t)^2 + v_y^2 = v_0^2(\sin\omega t_0 - \sin\omega t)^2 - 2I_p\frac{dt_0}{dt} \tag{4.15}$$

or, introducing dimensionless velocity $\mathbf{u} \equiv \mathbf{v}/v_0$,

$$(u_x - \sin\omega t)^2 + u_y^2 = (\sin\omega t_0 - \sin\omega t)^2 - \gamma^2\frac{dt_0}{dt}, \tag{4.16}$$

For the most energetic ($\simeq 3.17U_p$) trajectories $dt_0/dt \simeq 0.32$: the correction is small in the tunneling regime.

To check this simple recipe for removing the effect of the laser field, re-scattering for a single phase of birth $\omega t_0 = 17°$ is simulated, which corresponds to the maximum return energy. First, a classical trajectory starting at the 'exit' of the tunneling barrier $x_0 \approx I_p/E\cos\omega t_0$ is propagated from $\omega t_0 = 17°$ to the zero of the laser field $\omega t^* = \pi/2$. The position and velocity of the trajectory at $\omega t^* = \pi/2$ is used to initialize a Gaussian wave packet which is then propagated by solving the time-dependent Schroedinger equation in 2D for the model molecule Equation (4.11), starting at $\omega t^* = \pi/2$. The wave-packet width is set equal to that found by solving the Schrödinger equation over one half-cycle, starting in the ground state. Propagation in the electric field $E\cos\omega t$ with $\omega = 0.057$ a.u. and $E = 0.14$ continues until $\omega t = 2\pi$. With such a setup, the first re-collision is completed, the later returns have not occurred yet, and the vector-potential $A(t) = -v_0\sin\omega t$ is equal to zero at the turn-off, resulting in the zero velocity shift due to the instantaneous turn-off.

Figure 4.5(a) shows the $|\Psi|$ at $\omega t = 2\pi$ in the velocity space. Figure 4.5(b) shows the calculation for an identical initial condition for a single scattering center $V = -1.3/\sqrt{x^2 + y^2 + a^2}$ which provides an atomic-like reference with the same ionization potential. As expected, the spectrum lies on the circle with a shifted origin. The circular cut [Figure 4.5(c)] has the diffraction minima and maxima at the expected positions. The triple-peaked structure of the zero-order maximum is due to the holographic-type interference, which is also present in the reference

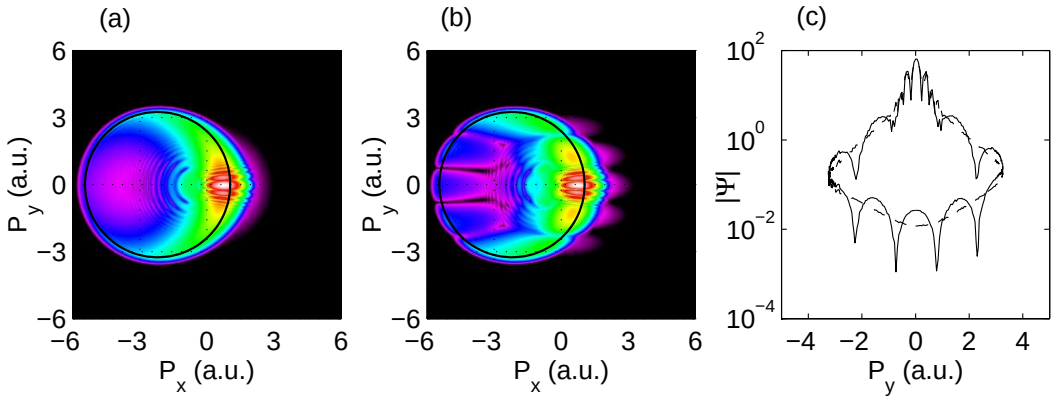

Figure 4.5: Recollision-induced diffraction for a single phase of birth. (a) $|\Psi(v_x, v_y)|$ for a model diatomic molecule, each new color corresponds to the next order of magnitude; (b) Reference signal for a model atom; (c) Circular cuts for the atom (dashed) and the molecule (solid)

atomic-like signal and disappears when the transverse velocity width is set to zero by setting $\Psi(x, y) = \Psi(x, 0)$ at $\omega t^* = \pi/2$. The hologram region is narrow due to narrow transverse distribution in the initial wave packet.

Having learned how to make proper cuts and how to identify holograms, laser-induced interference of different trajectories in the final spectrum can now be analyzed.

Direct vs re-scattered trajectories. The amplitude $a(\mathbf{v})$ to detect an electron with velocity $\mathbf{v}$ has contributions from both direct (no re-collision) and re-scattered electrons: $a = a_d + a_r$. The energy spectrum of the direct electrons has a cutoff at $2U_p$ and is narrowly focused along the laser polarization; see [18] and Equation (4.12). The holographic interference is also present there. Outside this region, only re-scattered trajectories and their interference is present.

Interference of long and short rescattered trajectories. In the strong field limit, the amplitude $a_r(\mathbf{v})$ factorizes into the product of the amplitudes of the consecutive processes of tunnel ionization a_{ion}, propagation in the laser field a_{pr}, scattering a_{sc}

and propagation to the end of the pulse:

$$\begin{aligned} a_r(v_x, v_y) &= \sum_t a_{ion}[t_0(t)] a_{pr}[t_0(t) \to t] \times \\ &\times \; a_{sc}[(v(t), 0) \to (v_x - v_0 \sin\omega t, v_y)] \; a_{pr}[t \to \infty] \end{aligned} \tag{4.17}$$

The summation is carried over all moments of recollision t which lead to the same final v_x, v_y. In contrast to standard above-threshold ionization, where such interference of 'quantum trajectories' (see e.g. [108]) is studied for a given *final* energy, here the angular pattern is taken at a given *recollision* energy. Such $t = \text{const}$ cuts do not correspond to a fixed final energy, changing the set of interfering trajectories: one of the moments of t in the sum Equation (4.17) is fixed for all v_x, v_y; others change as v_x, v_y are changed along the cut.

To minimize the number of interfering trajectories, phase-stabilized nearly single-cycle pulses with zero carrier-envelope phase, $E(t) = Ef(t)\cos\omega t$, are used in the simulations. This suppresses contributions of rescattered trajectories that start with phases other than $0 < \omega t_0 < \pi/2$, as well as the contributions of late and multiple returns. However, this does not eliminate the interference of two trajectories that start within the same quarter-cycle ($0 < \omega t_0 < \pi/2$) and return within the same cycle ($\omega t < 2\pi$). These are the short ($\omega t < \phi^*$) and long ($\omega t > \phi^*$) trajectories, where $\phi^* \simeq 4.4$ is the phase of the highest energy trajectory ($3.17U_p$). The key problem for diffraction related to these trajectories is that their recollision energies are different.

The interfering trajectories and phases can be identified for given v_x, v_y using Equation (4.16). For brevity, the small term $\gamma^2 dt_0/dt$ is dropped, which makes the analysis I_p-independent. In the dimensionless variables $\mathbf{u} = \mathbf{v}/v_0$, immediately after scattering the outgoing velocity in the x direction is

$$u_x^{(out)} = \pm\sqrt{(\sin\omega t_0 - \sin\omega t)^2 - u_y^2} \tag{4.18}$$

for the forward (+) and backward (−) elastic scattering. Here 'forward' and 'backward' mean that, without the laser field, the scattering angle would have been below

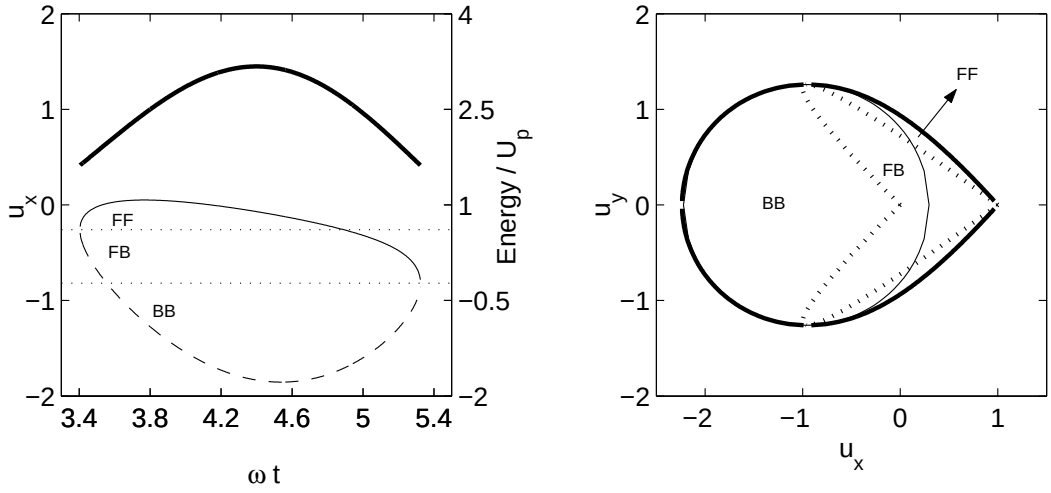

Figure 4.6: (a) Velocities u_x of forward F^+ (solid line) and backward F^- (dashed line) scattering as a function of the return phase $\phi = \omega t$, for $u_y = 0.9$. Thick solid line shows the return energy. Dotted lines separate three regions of interference marked as FF, FB, and BB (see text). (b) Classical cutoff of the angle-resolved spectrum (solid line) and a circular cut for the recollision phase $\phi = 4.4$ (recollision energy $\simeq 3.17U_p$).

or above $\pi/2$. The velocity at the detector is

$$u_x = u_x^{(out)} + \sin\omega t = \sin\omega t \pm$$
$$\pm \sqrt{(\sin\omega t_0(t) - \sin\omega t)^2 - u_y^2} \equiv F^{\pm}(t, u_y) \tag{4.19}$$

The functions $F^{\pm}(\phi, u_y)$ vs ϕ are shown in Figure 4.6(a) for $u_y = 0.9$. For each v_y, $F^{\pm}(\phi, u_y)$ form a loop which means that there are always two different moments of return, corresponding to the same final v_x. Note that the corresponding energies of return [Figure 4.6(a)] are different. The horizontal lines separate different regions of interference: forward-forward (FF) between two forward scattered trajectories, backward-backward (BB) between two backward scattered trajectories, and forward-backward (FB) between one of each. Local maxima (minima) of F^+ (F^+) define the energy cutoffs for each value of v_x. Figure 4.6(b) combines such points to show the classical cutoff of the angle-resolved spectrum and different areas of interference. Dashed circle in Figure 4.6(b) is the cut for $\phi \simeq 4.4$ (recollision energy $\simeq 3.17U_p$), which contains no interference in the 'BB' area.

Figure 4.7 shows numerical simulations of the time-dependent Schroedinger equation for the model potential Equation (4.11), with the peak field $E = 0.14$ a.u. and $\omega = 0.057$ a.u. Panel (a) shows the electron spectrum for 1.25-cycle long $\cos\omega t$ pulse with constant amplitude. The pulse starts at $\omega t = -\pi/2$ and ends at $\omega t = 2\pi$. The ground state is projected out at $\omega t = \pi/2$. Therefore, (i) the ionization occurs predominantly during the half-cycle $-\pi/2 < \phi_0 < \pi/2$, (ii) interference of long and short trajectories is not obscured by multiple returns and (iii) terminating the pulse abruptly at $\omega t = 2\pi$ causes no shift in the free electron velocity. The shape of the angle resolved spectrum is the same as expected from the analytical analysis shown in Figure 4.6(b). The interference of long and short trajectories leads to high-frequency (the corresponding phase difference scales as U_p/ω) ring-like structures in Figure 4.7(a) and (c). It does not mask the diffraction pattern, which is clearly visible along the cut corresponding to the maximum recollision energy in Figure 4.7(a) [see Figure 4.7(b)].

Panels (c) and (d) show simulations for a short pulse with the envelope $f(t) =$

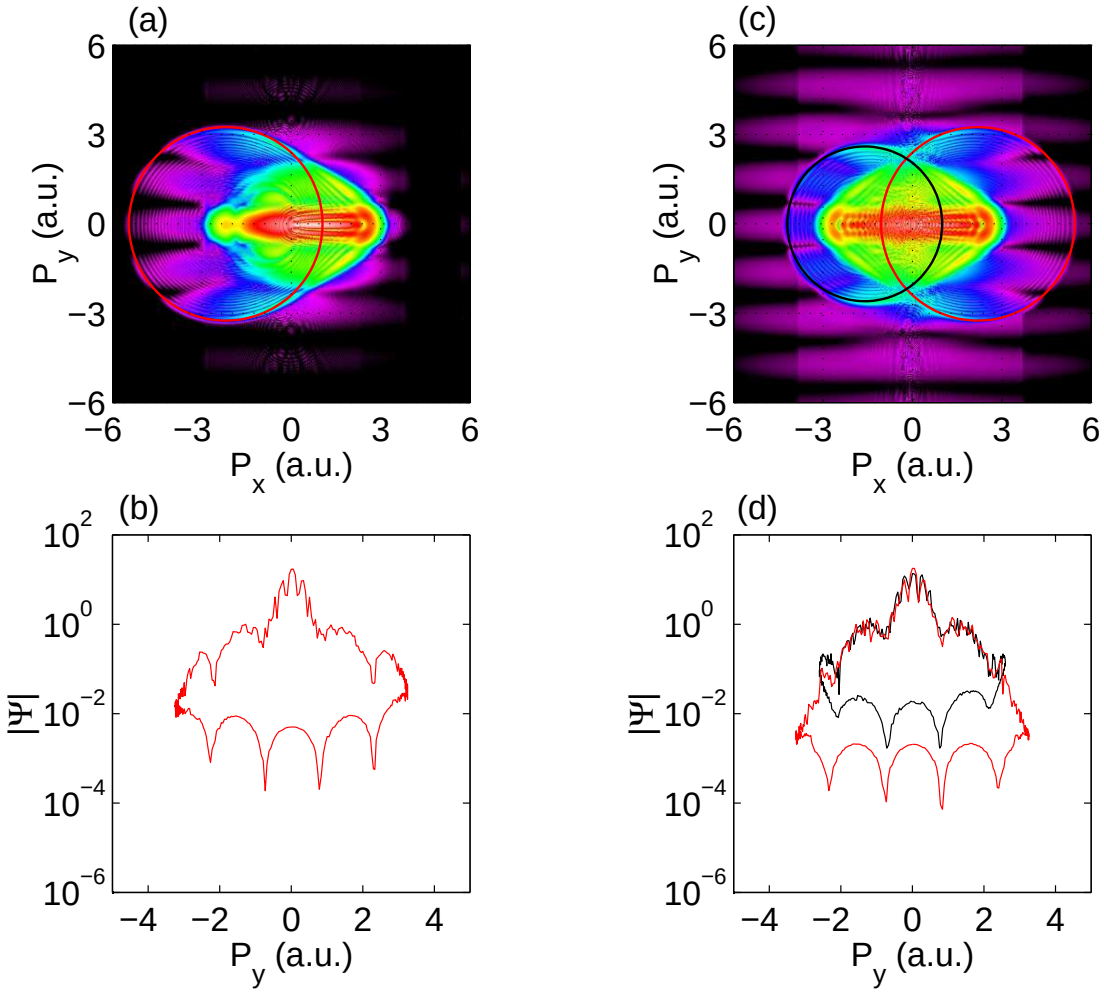

Figure 4.7: (a) Electron spectrum $|\Psi(v_x, v_y)|$ for 1.25-cycle pulse with constant amplitude, $E = 0.14$a.u. ($I \approx 6.9 \times 10^{14}$W/cm^2 and $\lambda = 800$nm, each new colour represents order of magnitude; (b) Spectral cut for fixed moment of recollision ($\omega t \approx 4.4$); (c,d) Same as (a,b) but for a 5 fs pulse $f(t) = \cos^2(\pi t/2T)$, $T = 5$ fs.

$\cos^2(\pi t/2T)$ for $|t| < T$ and $f(t) = 0$ otherwise, for $T = 5$ fs (FWHM=5 fs). The diffraction pattern is still clear along similar cuts, see panel (d). Note that there are now two overlapped spectra similar to Figure 4.7(a), one reflected through $v_y = 0$. They originate from ionization events near $\omega t_0 = 0$ (left image) and near $\omega t_0 = -\pi/2$ (right image). The images are not mirror-symmetric, as would have been the case for the long pulse. The first ionization event near $\omega t_0 = -\pi/2$ has lower probability but higher recollision energy due to the minimal change of the envelope during the oscillation. For the second ionization event, the maximum recollision energy is reduced by the quickly decreasing envelope.

The ring-like structures in the interference of long and short trajectories can be reproduced by the stationary phase analysis Equation (4.17) (which contains no contribution from direct of electrons and hence no hologram). Figure 4.8 shows

$$\aleph(\mathbf{v}) = \left| \sum_n \exp[-iS_1(t^{(n)}, t_0^{(n)}) - iS_2(\mathbf{v}, T, t^{(n)}) + iI_p t_0^{(n)}] \right|^2 . \qquad (4.20)$$

which singles out the interference by setting weights associated with ionization and scattering to unity and omitting the structural contribution. The summation index $n = 1, 2$ goes over the two trajectories that start at $0 < \omega t_0 < \pi/2$ and end up with the same final velocity $\mathbf{v}$. The corresponding moments of re-collision $t^{(n)}$ are found from Equation (4.16) (neglecting the γ^2 term) and $t_0^{(n)} = t_0(t^{(n)})$ are the solutions of Equation (4.14). The actions accumulated before and after the recollision are

$$\begin{aligned} S_1(t, t_0) &= \frac{1}{2} \int_{t_0}^{t} dt' [-v_0 \sin \omega t' + v_0 \sin \omega t_0]^2 \\ S_2(\mathbf{v}, T, t) &= \frac{1}{2} \int_{t}^{T} dt' [\mathbf{v} - \mathbf{e_x} v_0 \sin \omega t_0]^2 . \end{aligned} \qquad (4.21)$$

The number of interference fringes counted along the $v_y = 0$ cut in Figure 4.8 is only slightly less then that counted in Figure 4.7(a). This small difference is currently attributed to the effects of the Coulomb potential.

Thus, despite a series of complications, the diffraction image of the parent molecule can be distilled out of the electron spectrum generated by intense-field

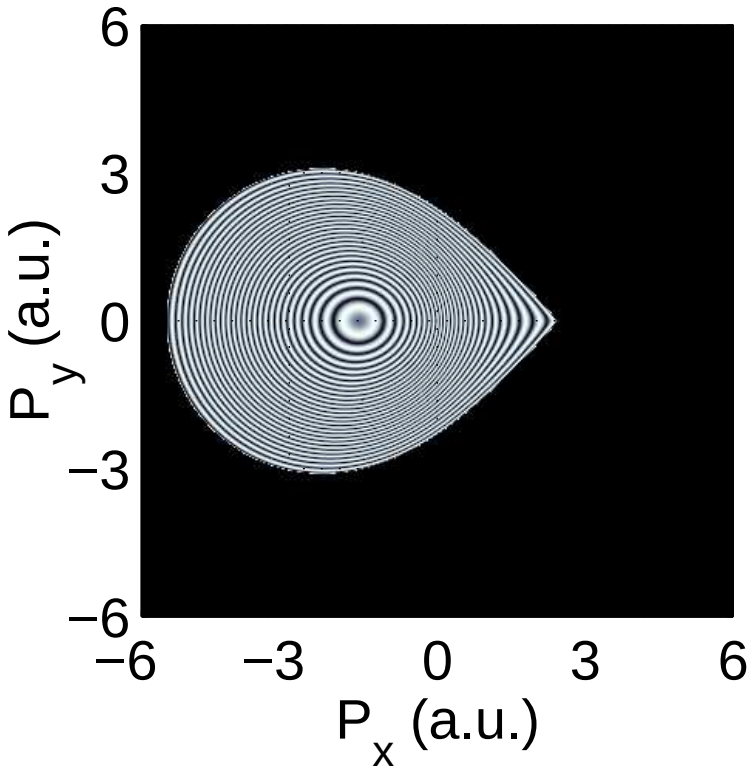

Figure 4.8: Analytical results emphasizing ring-like structures in Figure 4.7(a) caused by interference of short and long trajectories.

ionization.

One of the most interesting directions suggested by this work is the opportunity to use holographic structures to image the molecule. Unlike diffraction, the hologram records both the magnitude *and* phase of the scattering amplitude. In the present calculation, the hologram barely distinguishes atom from molecule: the molecule is aligned perpendicular to the laser field and the initial spread in the transverse velocity is too small to provide sufficient spatial resolution. However, changing the alignment of the molecule would allow one to use the large longitudinal velocity component for holography, increasing the resolution. Another possibility is to use elliptical polarization, either constant or time dependent, to move the wave packet by its half-width along the molecular axis, enhancing the holographic signal near the first maximum while retaining the zero maximum. One can also stretch the molecule.

Chapter 5

Summary and Outlook

Using modern ultrafast laser technology, it is now possible to control the motion of small molecules with lasers. This development contributes to a long history of using light to exert forces on and control matter.

The work presented in this thesis considered the specific case of controlling molecular rotations using strong highly non-resonant low frequency laser fields. Methods of creating both in-field as well as field-free laser-induced molecular alignment have been outlined. The experimental observations of molecular alignment included in the thesis demonstrate that these ideas are not the crazy dreams of a theorist, but are instead readily achievable with modern femtosecond and picosecond laser systems.

Future directions for molecular alignment lie with the 3-dimensional alignment of asymmetric top molecules and in particular field-free 3-dimensional alignment. In linear molecules, there is only one rotational axis and hence only one revival time scale, making field-free alignment using rotational revivals relatively simple. Asymmetric top molecules, on the other hand, have three distinct rotational axes all having different revival time scales. This makes the creation of field-free 3-dimensional alignment a much more difficult problem than in the case of linear molecules.

Additional control scenarios for molecular rotations were considered including

the optical centrifuge, control using phase shifts at fractional revivals, and quantum control of the classically chaotic kicked rotor. Although these control methods are interesting from a fundamental perspective of learning exactly what is possible using light to control molecular rotations, they also fit into a larger context of coherent control [76] and strong field control (e.g. [109] and [110]) of molecules. These fields seek to use quantum control methods to effect and control the outcome of molecular processes with the ultimate goal being laser-control of chemical reactions. The idea is to learn how one can create and control unique quantum superpositions in the hope that such novel quantum states of molecules can effect subsequent molecular processes.

Two applications of aligned molecular states were presented. The first is to use revivals of molecular alignment as a non-linear medium for laser pulse compression. With this method, compression of optical pulse to the nearly single-cycle regime is possible. Similar ideas of pump-probe pulse compression techniques can be applied using dielectrics as a non-linear medium [111, 112]. Using such a setup, nearly single-cycle pulses can be achieved, not only in the optical regime but also in the mid-infrared with compressible wavelengths ranging from 400 nm to 3 μm. These nearly single-cycle pulses represent the shortest pulses physically achievable for these wavelength. In order to go beyond the femtosecond regime, it is necessary to move to shorter wavelengths and higher frequencies. The latest developments in ultrafast pulses lie with extreme ultra-violet attosecond pulse generation [113].

The second application of aligned molecular states was that of laser-induced electron diffraction and imaging. Future directions in this work lie with holography. It was shown herein that the process of laser-induced electron recollision leads not only to diffraction, but also to holography. It remains to be learned how to best read these holographic images taken in the presence of a strong laser field, just as learning how to read the diffraction images in a strong laser field was necessary. Also, implementing these ideas of laser-induced diffraction and imaging in larger molecules offers interesting directions. The next step here would be to apply this technique of diffraction and imaging to triatomics.

Drawing from the developments in laser control of atoms, interesting directions

for the laser control of molecules in general would certainly include cooling and trapping of molecules and the realization of molecular Bose-Einstein condensates. No efficient method of directly cooling a molecular gas is currently known. Attempts at creating ultracold molecules follow the route of photoassociation of ultracold atoms or recombination of ultracold atom pairs using a Feshbach resonance. Using this technique, a molecular Bose-Einstein condensate of about 10^5 Li_2 molecules has just recently been achieved [114]. Although this is indeed an interesting success, the method can not be used to create condensates of arbitrary molecules. A more interesting route would be the development of general methods to directly cool the translational, vibrational, and rotational degrees of freedom of molecules.

Bibliography

[1] P. Lebedev. The experimental study of the pressure of the light. *Ann. Phys.*, 6:433, 1901.

[2] E.F. Nichols and G.F. Hull. A preliminary communication on the pressure of heat and light radiation. *Phys. Rev.*, 13:307, 1901.

[3] E.F. Nichols and G.F. Hull. The pressure due to radiation. *Phys. Rev.*, 17:26, 1903.

[4] A. Einstein. On the quantum theory of radiation. *Phys. Z.*, 18:121, 1917. [for an English translation, see A. Einstein, *The collected papers of Albert Einstein*, translated by A. Engel (Princeton U.P., Princeton, 1997), Vol. 6, pp. 220-233].

[5] O.R. Frisch. Experimental demonstration of Einstein's radiation recoil. *Z. Phys.*, 86:42, 1933.

[6] A. Kastler. Quelques suggestions concernant la production optique et la détection optique d'une inégalité de population des niveaux de quantification spatiale des atomes: Application à l'expérience de Stern et Gerlach et à la résonance magnétique. *J. Phys. Radium*, 11:233, 1950.

[7] J. Brossel, A. Kastler, and J. Winter. Generation optique d'une inégalité de population entre les sous-niveaux Zeeman de l'état fondamental des atomes. *J. Phys. Radium*, 13:668, 1952.

[8] S. Chu. Nobel lecture: The manipulation of neutral particles. *Rev. Mod. Phys.*, 70:685, 1998.

[9] C.N. Cohen-Tannoudji. Nobel lecture: The manipulation of neutral particles. *Rev. Mod. Phys.*, 70:707, 1998.

[10] W.D. Phillips. Nobel lecture: Laser cooling and trapping of neutral atoms. *Rev. Mod. Phys.*, 70:721, 1998.

[11] H.J. Metcalf and P. van der Straten. *Laser Cooling and Trapping*. Springer-Verlag, New York, 1999.

[12] E.A. Cornell and C.E. Wieman. Nobel lecture: Bose-Einstein condensation in a dilute gas, the first 70 years and some recent experiments. *Rev. Mod. Phys.*, 74:875, 2002.

[13] W. Ketterle. Nobel lecture: When atoms behave as waves: Bose-Einstein condensation and the atom laser. *Rev. Mod. Phys.*, 74:1131, 2002.

[14] J.E. Bjorkholm, R.R. Freeman, A. Ashkin, and D.B. Pearson. Observation of focusing of neutral atoms by the dipole forces of resonance-radiation pressure. *Phys. Rev. Let.*, 41:1361, 1978.

[15] T. Seideman. Manipulating external degrees of freedom with intense light: Laser focusing and trapping of molecules. *J. Chem. Phys.*, 106:2881, 1997.

[16] H. Sakai, A. Tarasevitch, J. Danilov, H. Stapelfeldt, R.W. Yip, C. Ellert, E. Constant, and P.B. Corkum. Optical deflection of molecules. *Phys. Rev. A*, 57:2794, 1998.

[17] D. Strickland and G. Mourou. Compression of amplified chirped optical pulses. *Opt. Commun.*, 56:219, 1985.

[18] N. Delone and V. Krainov. *Multiphoton Processes in Atoms*. Springer-Verlag, 1994.

[19] B. Zon and B. Katsnelson. Nonresonant scattering of intense light by a molecule. *Zh. Eksp. Teor. Fiz.*, 69:1166, 1975.

[20] B. Friedrich and D. Herschbach. Alignment and trapping of molecules in intense laser fields. *Phys. Rev. Lett.*, 74:4623, 1995.

[21] T. Seideman. Rotational excitation and molecular alignment in intense laser fields. *J. Chem. Phys.*, 103:7887, 1995.

[22] D. Normand, L.A. Lompre, and C. Cornaggia. Laser-induced molecular alignment probed by a double-pulse experiment. *J. Phys. B: At. Mol. Opt. Phys.*, 25:L497, 1992.

[23] J.J. Larsen, H. Sakai, C.P. Safvan, I. Wendt-Larsen, and H. Stapelfeldt. Aligning molecules with intense nonresonant laser fields. *J. Chem. Phys.*, 111:7774, 1999.

[24] J.J. Larsen, I. Wendt-Larsen, and H. Stapelfeldt. Controlling the branching ratio of photodissociation using aligned molecules. *Phys. Rev. Lett.*, 83:1123, 1999.

[25] J. Ortigoso, M. Rodriguez, M. Gupta, and B. Friedrich. Time evolution of pendular states created by the interaction of molecular polarizability with a pulsed nonresonant laser field. *J. Chem. Phys.*, 110:3870, 1999.

[26] T. Seideman. Revival structure of aligned rotational wave packets. *Phys. Rev. Lett.*, 83:4971, 1999.

[27] T. Seideman. On the dynamics of rotationally broad, spatially aligned wave packets. *J. Chem. Phys.*, 115:5965, 2001.

[28] F. Rosca-Pruna and M.J.J. Vrakking. Experimental observation of revival structures in picosecond laser-induced alignment of I_2. *Phys. Rev. Lett.*, 87:153902, 2001.

[29] F. Rosca-Pruna and M.J.J. Vrakking. Revival structures in picosecond laser-induced alignment of I_2 molecules. I. Experimental results. *J. Chem. Phys.*, 116:6567, 2002.

[30] F. Rosca-Pruna and M.J.J. Vrakking. Revival structures in picosecond laser-induced alignment of I_2 molecules. II. Numerical modeling. *J. Chem. Phys.*, 116:6579, 2002.

[31] P.W. Dooley, I.V. Litvinyuk, K.F. Lee, D.M. Rayner, M. Spanner, D.M. Villeneuve, and P.B. Corkum. Direct imaging of rotational wave-packet dynamics of diatomic molecules. *Phys. Rev. A*, 68:023406, 2003.

[32] V. Kalosha, M. Spanner, J. Herrmann, and M.Yu. Ivanov. Generation of single dispersion precompensated 1-fs pulses by shaped-pulse optimized high-order stimulated Raman scattering. *Phys. Rev. Lett.*, 88:103901, 2002.

[33] M. Spanner and M.Yu. Ivanov. Optimal generation of single-dispersion precompensated 1-fs pulses by molecular phase modulation. *Opt. Lett.*, 28:576, 2003.

[34] J. Underwood, M. Spanner, M.Yu. Ivanov, J. Mottershead, B.J. Sussman, and A. Stolow. Switched wave packets: A route to nonperturbative quantum control. *Phys. Rev. Lett.*, 90:223001, 2003.

[35] E. Péronne, M.D. Poulsen, C.Z. Bisgaard, and H. Stapelfeldt. Nonadiabatic alignment of asymmetric top molecules: Field-free alignment of iodobenzene. *Phys. Rev. Lett.*, 91:043003, 2003.

[36] I.Sh. Averbukh and R. Arvieu. Angular focusing, squeezing, and rainbow formation in a strongly driven quantum rotor. *Phys. Rev. Lett.*, 87:163601, 2001.

[37] M. Leibscher I.Sh. Averbukh and H. Rabitz. Molecular alignment by trains of short laser pulses. *Phys. Rev. Lett.*, 90:213001, 2003.

[38] K.F. Lee, I.V. Litvinyuk, P.W. Dooley, M. Spanner, D.M. Villeneuve, and P.B. Corkum. Two-pulse alignment of molecules. *J. Phys. B: At. Mol. Opt. Phys.*, 37:L43, 2004.

[39] C.Z. Bisgaard, M.D. Poulsen, E. Péronne, S.S. Viftrup, and H. Stapelfeldt. Observation of enhanced field-free molecular alignment by two laser pulses. *Phys. Rev. Lett.*, 92:173004, 2004.

[40] F. Légaré and A.D. Bandrauk. Enhancement of laser-induced molecular alignment by simultaneous photodissociation. *Phys. Rev. A*, 64:031406(R), 2001.

[41] J.J. Larsen, K. Hald, N. Bjerre, and H. Stapelfeldt. Three dimensional alignment of molecules using elliptically polarized laser fields. *Phys. Rev. Lett.*, 85:2470, 2000.

[42] J. Karczmarek, J. Wright, P. Corkum, and M. Ivanov. Optical centrifuge for molecules. *Phys. Rev. Lett.*, 82:3420, 1999.

[43] D.M. Villeneuve, S.A. Aseyev, P. Dietrich, M. Spanner, M.Yu. Ivanov, and P.B. Corkum. Forced molecular rotation in an optical centrifuge. *Phys. Rev. Lett.*, 85:542, 2000.

[44] M. Spanner and M.Yu. Ivanov. Angular trapping and rotational dissociation of a diatomic molecule in an optical centrifuge. *J. Chem. Phys.*, 114:3456, 2001.

[45] M. Spanner, K.M. Davitt, and M.Yu. Ivanov. Stability of angular confinement and rotational acceleration of a diatomic molecule in an optical centrifuge. *J. Chem. Phys.*, 115:8403, 2001.

[46] M. Spanner, E.A. Shapiro, and M.Yu. Ivanov. Coherent control of rotational wave-packet dynamics via fractional revivals. *Phys. Rev. Lett.*, 92:093001, 2004.

[47] E.A. Shapiro, M. Spanner, and M.Yu. Ivanov. Quantum logic approach to wave packet control. *Phys. Rev. Lett.*, 91:237901, 2003.

[48] J. Gong and P. Brumer. Coherent control of quantum chaotic diffusion. *Phys. Rev. Lett.*, 86:1741, 2001.

[49] J. Gong and P. Brumer. Coherent control of quantum chaotic diffusion: Diatomic molecules in a pulsed microwave field. *J. Chem. Phys.*, 115:3590, 2001.

[50] R. Blümel and W.P. Reinhardt. *Chaos in Atomic Physics*. Cambridge University Press, United Kingdom, 1997.

[51] M.S. Child. *Semiclassical Mechanics With Molecular Applications*. Oxford University Press, Oxford UK, 1991.

[52] E. Heller. Bound-state eigenfunctions of classically chaotic Hamiltonian systems: Scars of periodic orbits. *Phys. Rev. Lett.*, 53:1515, 1984.

[53] A.M. Weiner. Femtosecond optical pulse shaping and processing. *Prog. Quant. Electron.*, 19:161, 1995.

[54] F. Verluise, V. Laude, Z. Cheng, Ch. Spielmann, and P. Tournois. Amplitude and phase control of ultrashort pulses by use of an acousto-optic programmable dispersive filter: Pulse compression and shaping. *Opt. Lett.*, 25:575, 2000.

[55] R.L. Fork, C.H. Brito Cruz, P.C. Becker, and C.V. Shank. Compression of optical pulses to six femtoseconds by using cubic phase compensation. *Opt. Lett.*, 12:483, 1987.

[56] A. Baltuška, Z. Wei, M.S. Pshenichnikov, and D.A. Wiersma. Optical pulse compression to 5fs at a 1-MHz repetition rate. *Opt. Lett.*, 22:102, 1997.

[57] M. Nisoli, S.D. Silvestri, R. Szipocs, K. Ferencz, C. Spielmann, S. Sartania, and F. Krausz. Compression of high-energy laser pulses below 5 fs. *Opt. Lett.*, 22:522, 1997.

[58] A. Baltuška, T. Fuji, and T. Kobayashi. Visible pulse compression to 4fs by optical parametric amplification and programmable dispersion control. *Opt. Lett.*, 27:306, 2002.

[59] M. Spanner, O. Smirnova, P.B. Corkum, and M.Yu Ivanov. Reading diffraction images in strong field ionization of diatomic molecules. *J. Phys. B: At. Mol. Opt. Phys.*, 37:L243, 2004.

[60] H. Ihee, V.A. Lobastov, U.M. Gomez, B.M. Goodson, R. Srinivasan, C.-Y. Ruan, and A.H. Zewail. Direct imaging of transient molecular structures with ultrafast diffraction. *Science*, 291:458, 2001.

[61] R.W. Boyd. *Nonlinear Optics*. Academic Press, California USA, 1992.

[62] G. Herzberg. *Molecular Spectra and Molecular Structure: Volume I - Spectra of Diatomic Molecules*. Krieger Publishing Company, Florida USA, 2^{nd} edition, 1989.

[63] K.P. Huber and G. Herzberg (data prepared by J.W. Gallagher and R.D. Johnson III). Constants of diatomic molecules. In P.J. Linstrom and W.G. Mallard, editors, *NIST Chemistry WebBook, NIST Standard Reference Database Number 69*. Gaithersburg, MD, July 2001. (http://webbook.nist.gov).

[64] K.J. Miller. Additivity methods in molecular polarizability. *J. Am. Chem. Soc.*, 112:8533, 1990.

[65] K.J. Miller. Calculation of the molecular polarizability tensor. *J. Am. Chem. Soc.*, 112:8543, 1990.

[66] W.H. Press, B.P. Flannery, S.A. Teukolsky, and W.T. Vetterling. *Numerical Recipes*. Cambridge University Press, Cambridge, second edition, 1992.

[67] H.H. Brandsen and C.J. Joachain. *Quantum Mechanics*. Prentice Hall, Harlow England, 2^{nd} edition, 2000.

[68] A.E. Kaplan, P. Stifter, K.A.H. van Leeuwen, W.E. Lamb, and W.P. Schleich. Intermode traces - fundamental interference phenomenon in quantum and wave physics. *Phys. Scr.*, T76:93, 1998.

[69] I. Marzoli, F. Saif, I. Bialynicki-Birula, O.M. Friesch, A.E. Kaplan, and W.P. Schleich. Quantum carpets made simple. *Acta Phys. Slovaca*, 48:323, 1998.

[70] A.E. Kaplan, I. Marzoli, W.E. Lamb, Jr., and W.P. Schleich. Multimode interference: Highly regular pattern formation in quantum wave-packet evolution. *Phys. Rev. A*, 61:032101, 2000.

[71] J. Eberly, N. Narozhny, and J. Sanchez-Mondragon. Periodic spontaneous collapse and revival in a simple quantum model. *Phys. Rev. Lett.*, 44:1323, 1980.

[72] I.S. Averbukh and N.F. Perelman. Fractional revivals: Universality in the long-term evolution of quantum wave packets beyond the correspondence principle dynamics. *Phys. Lett. A*, 139:449, 1989.

[73] P.W. Dooley. (private communication).

[74] V. Renard, M. Renard, S. Guérin, Y.T. Pashayan, B. Lavorel, O. Faucher, and H.R. Jauslin. Postpulse molecular alignment measured by a weak field polarization technique. *Phys. Rev. Lett.*, 90:153601, 2003.

[75] D.J. Tannor and S.A. Rice. Coherent pulse sequence induced control of selectivity of reactions: Exact quantum mechanical calculations. *J. Chem. Phys.*, 85:5805, 1985.

[76] M. Shapiro and P. Brumer. *Principles of the Quantum Control of Molecular Processes*. John Wiley & Sons, New Jersey USA, 2003.

[77] D. You, R.R. Jones, P. Bucksbaum, and D. Dykaar. Generation of high-power sub-single-cycle 500-fs electromagnetic pulses. *Opt. Lett.*, 18:290, 1993.

[78] N.E. Tielking, T.J. Bensky, and R.R. Jones. Effects of imperfect unipolarity on the ionization of rydberg atoms by subpicosecond half-cycle pulses. *Phys. Rev. A*, 51:3370, 1995.

[79] C.H. Townes and A.L. Shawlow. *Microwave Spectroscopy*. McGraw-Hill, New York USA, 1955.

[80] M. Machholm and M.E. Henriksen. Field-free orientation of molecules. *Phys. Rev. Lett.*, 87:193001, 2001.

[81] S. Minemoto, H. Nanjo, H. Tanji, T. Suzuki, and H. Sakai. Observation of molecular orientation by the combination of electrostatic and nonresonant, pulsed laser fields. *J. Chem. Phys.*, 118:4052, 2003.

[82] E.A. Shapiro. Forms of localization of Rydberg wave packets. *Sov. Phys. JETP*, 91:449, 2000.

[83] E.A. Shapiro. Angular orientation of wave packets in molecules and atoms. *Laser Physics*, 12:1448, 2002.

[84] P. Kasperkovitz and M. Peev. Long-time evolution of semiclassical states in anharmonic potentials. *Phys. Rev. Lett.*, 75:990, 1995.

[85] Q.L. Jie, S.J. Wang, and L.Fu Wei. Partial revivals of wave packets: An action-angle phase-space description. *Phys. Rev. A*, 57:3262, 1997.

[86] F.L. Moore, J.C. Robinson, C.F. Bharucha, B. Sundaram, and M.G. Raizen. Atom optics realization of the quantum delta-kicked rotor. *Phys. Rev. Lett.*, 75:4598, 1995.

[87] V. Milner, D.A. Steck, W.H. Oskay, and M.G. Raizen. Recovery of classically chaotic behavior in a noise-driven quantum system. *Phys. Rev. E*, 61:7223, 2000.

[88] R. Blümel, S. Fishman, and U. Smilansky. Excitation of molecular rotation by periodic microwave pulses: A testing ground for Anderson localization. *J. Chem. Phys.*, 84:2604, 1986.

[89] A.B. Rechester and R.B. White. Calculation of turbulent diffusion for the Chirikov-Taylor model. *Phys. Rev. Lett.*, 44:1586, 1980.

[90] A.B. Rechester, M.N. Rosenbluth, and R.B. White. Calculation of turbulent diffusion for the chirikov-taylor model. *Phys. Rev. A*, 23:2664, 1981.

[91] A.V. Sokolov, D.R. Walker, D.D. Yavuz, G.Y. Yin, and S.E. Harris. Raman generation by phased and antiphased molecular states. *Phys. Rev. Lett.*, 85:562, 2000.

[92] A.V. Sokolov, D.R. Walker, D.D. Yavuz, G.Y. Yin, and S.E. Harris. Femtosecond light source for phase-controlled multiphoton ionization. *Phys. Rev. Lett.*, 87:033402, 2001.

[93] M. Wittmann, A. Nazarkin, and G. Korn. fs-pulse synthesis using phase modulation by impulsively excited molecular vibrations. *Phys. Rev. Lett.*, 84:5508, 2000.

[94] M. Wittmann, A. Nazarkin, and G. Korn. Synthesis of periodic femtosecond pulse trains in the ultraviolet by phase-locked Raman sideband generation. *Opt. Lett.*, 26:298, 2001.

[95] N. Zhavoronkov and G. Korn. Generation of single intense short optical pulses by ultrafast molecular phase modulation. *Phys. Rev. Lett.*, 88:203901, 2002.

[96] R.A. Bartels, T.C. Weinacht, N. Wagner, M. Baertschy, C.H. Greene, M.M. Murnane, and H.C. Kapteyn. Phase modulation of ultrashort light pulses using molecular rotational wave packets. *Phys. Rev. Lett.*, 88:013903, 2002.

[97] V. Kalosha and J. Herrmann. Phase relations, quasicontinuous spectra and subfemtosecond pulses in high-order stimulated Raman scattering with short-pulse excitation. *Phys. Rev. Lett.*, 85:1226, 2000.

[98] R.K. Bullough, P.M. Jack, P.W. Kitchenside, and R. Saunders. Solitons in laser physics. *Phys. Scr.*, 20:364, 1979.

[99] P.E. Ciddor. Refractive index of air: New equations for the visible and near infrared. *Appl. Opt.*, 35:1566, 1996.

[100] G. Yudin and M. Ivanov. Nonadiabatic tunnel ionization: Looking inside a laser cycle. *Phys. Rev. A*, 64:013409, 2001.

[101] T. Zuo, A.D. Bandrauk, and P.B. Corkum. Laser-induced electron diffraction: A new tool for probing ultrafast molecular dynamics. *Chem. Phys. Lett.*, 259:313, 1996.

[102] M. Lein, J. Marangos, and P. Knight. Electron diffraction in above-threshold ionization of molecules. *Phys. Rev. A*, 66:051404, 2002.

[103] H. Niikura, F. Légaré, R. Hasbani A. D. Bandrauk, M.Yu. Ivanov, D. M. Villeneuve, and P.B. Corkum. Sub-laser-cycle electron pulses for probing molecular dynamics. *Nature*, 417:917, 2002.

[104] P.B. Corkum. Plasma perspective on strong field multiphoton ionization. *Phys. Rev. Lett.*, 71:1994, 1993.

[105] H. Stapelfeld and T. Seideman. Colloquium: Aligning molecules with strong laser pulses. *Rev. Mod. Phys.*, 75:543, 2003.

[106] S.N. Yurchenko, S. Patchkovskii, I.V. Litvinyuk, P.B. Corkum, and G.L. Yudin. *Phys. Rev. Lett.*, 2004. (*submitted*).

[107] A. Scrinzi V. Yakovlev. High harmonic imaging of few-cycle laser pulses. *Phys. Rev. Lett.*, 91:153901, 2003.

[108] R. Kopold, D.B. Milosevic, and W. Becker. Rescattering processes for elliptical polarization: A quantum trajectory analysis. *Phys. Rev. Lett.*, 84:3831, 2000.

[109] A. Assion, T. Baumert, M. Bergt, T. Brixner, B. Kiefer, V. Seyfried, M. Strehle, and G. Gerber. Control of chemical reactions by feedback-optimized phase-shaped femtosecond laser pulses. *Science*, 282:919, 1998.

[110] R.J. Levis, G. Menkir, and H. Rabitz. Selective bond dissociation and rearrangement with optimally tailored, strong-field laser pulses. *Science*, 292:709, 2001.

[111] M. Spanner, M.Yu. Ivanov, V. Kalosha, J. Herrmann, D.A. Wiersma, , and M. Pshenichnikov. Tunable optimal compression of ultrabroadband pulses by cross-phase modulation. *Opt. Lett.*, 28:749, 2003.

[112] M. Spanner, M. Pshenichnikov, V. Olvo, and M.Yu. Ivanov. Controlled supercontinuum generation for optimal pulse compression: A time-warp analysis of nonlinear propagation of ultrabroadband pulses. *App. Phys. B*, 77:329, 2003.

[113] R. Kienberger, E. Goulielmakis, M. Uiberacker, A. Baltuška, V. Yakovlev, F. Bammer, A. Scrinzi, Th. Westerwalbesloh, U. Kleinberg, U. Heinzmann, M. Drescher, and F. Krausz. Atomic transient recorder. *Nature*, 427:817, 2004.

[114] S. Jochim, M. Bartenstein, A. Altmeyer, G. Hendl, S. Riedl, C. Chin, J. Hecker Denschlag, and R. Grimm. Bose-Einstein condensation of molecules. *Science*, 302:2102, 2003.